The University of Nottingham

Sub-Terahertz:

Generation and Detection

Mohd Azlishah bin Othman, MSc.

Thesis submitted to University of Nottingham for the degree of

Doctor of Philosophy

June 2013

Acknowledgment

I would like to express the deepest appreciation to my supervisor, Professor Dr Ian Harrison, for his guidance throughout my research work. For Ian, it is your brilliant insights and support that make this work possible and I owe you so much not only for your support on the research, but also for your support in my life.

Furthermore, thanks to all research staff in Photonic and RF Engineering Group under Division of Electrical Systems and Optics, Department of Electrical and Electronic Engineering, University of Nottingham for their support and cooperation on the work. Besides, I would like to express my deepest gratitude to the rest of colleagues, technicians, my fellow labmates in University of Nottingham: Xiao Li, Suhaila Ishak, Leah Righway, Vinoth, Frank, Kuldip and Fen for all the fun we had in the last four years.

Special thanks are owed to my parents and sisters, whose have supported me throughout my years of education, both morally and financially, and the one above all of us, the supreme God, for answering my prayers. Also, thanks a lot to my beloved wife Shadia Suhaimi for her passion in understanding me on working for this research.

Last but not least, my sincere thanks go to my sponsors; Malaysian Government and Universiti Teknikal Malaysia Melaka (UTeM), Nottingham Malaysian Community (NMC), friends and ex-housemates; Fairul Ezwan, Muzahar, Ahmad Fikri Dr. Mohd Fadzelly and Ir. Dr Nazri Othman.They were always supporting and encouraging me with their best wishes. I will be forever grateful for their love.

Abstract

Nowadays, there has been an increasing interest in Terahertz (THz) radiation for application across scientific disciplines including atmospheric sensing, medical diagnosis, security screening and explosive detection. The limitation of THz generators and detectors has gained interest from scientists and engineers to explore the development of both sources and detectors. With the advantages of low cost, low power consumption, high reliability and potential for large-scale integration, sub-THz generator and detector can be developed using CMOS process technology.

In this thesis, an IMPATT diode acts as a sub-THz generator, HEMTs and MOSFETs act as sub-THz detectors, which are developed in AMS 0.35 µm CMOS technology and UMC, 0.18 µm CMOS technology. The size of the IMPATT diode was 120 µm x 50 µm with the target resonant frequency at 30 GHz. The experiment results show that the operating frequency of the IMPATT diode was between 12 GHz up to 14 GHz. Then by using HEMTs with 0.2 µm gate length and 200 µm gate widths, sub-THz radiation detection has been demonstrated. Experimental results show that the photoresponse depends on the drain current and the gate to source voltage V_{GS}. In addition, photoresponse also depends on varying frequencies up to 220 GHz and fixed the drain current. Furthermore, the HEMT also give an indication of response by varying the input power of microwave extender.

MOSFETs from two types of CMOS technology; AMS 0.35µm and UMC 0.18 µm technology with different gate length ranging from 180 nm up 350 nm were demonstrated. These results provide evidence that the photoresponse increases with the drain current and the RF input power, but inversely to the frequencies. These results also provide evidence that the MOSFETs are able to work as low cost and sensitive sub-THz detector.

Contents

List of figures

List of Abbreviations

2 DEG Two Dimensional Electron Gas

AC Voltage Alternative Current Voltage

ADS Advanced Design System

AlGaAs Aluminium Galium Arsenide

AlGaN Aluminium Galium Nitride

AMS C35 Austria Micro Systems CMOS 0.35 μm process technology

BNC connector Bayonet Neill–Concelman connector

BWO Backward Wave Oscillator

CdTe Cadmium Telluride

CMOS Complementary Metal Oxide Semiconductor

CO_2 Carbon dioxide

CW Continuous Wave

DC Direct Current

DMM Digital Multimeter

DRC Design Rules Check

E-O Electro-Optic

EMI Electromagnetic Interface

ESR Equivalent Series Resistance

FEL Free Electron Laser

FET Field Effect Transistor

FPA Focal Plane Array

FS-EOS Free-Space-Electro-Optic-Sampling

G-S-G Ground-Signal-Ground

GaAs Galium Arsenide

GaN Galium Nitride

GPIB General Purpose Interface Bus

HB Harmonic Balance

HEMT High Electron Mobility Transistor

IF Intermediate Frequency

IMPATT diode Impact Ionization Avalanche Transit Time diode

InP Indium Phosphide

IV Current-Voltage Charatcteristic

LO Local Oscillator

LTG Low Temperature Grown

LVS Layout Versus Schematic

MBE molecular beam epitaxy

MOSFET Metal Oxide Semiconductor Field Effect Transistor

OML Olsen Microwave Lab

PCB Printed Circuit Board

QCL Quantum Cascade Laser

RF Radio Frequency

SMT Surface Mount Technologies

SNR Signal to Noise Ratio

SOI Silicon-On-Insulator

SOL Short-Open-Load

STJ Superconducting Tunnel Junctions

Sub-THz Sub Terahertz

TFC Terahertz Frequency Comb

THz Terahertz

UMC18 United Microelectronics Corporation CMOS 0.18 μm process technology

VLSI circuits Very Large Scale Integrated circuits

VNA Vector Network Analyzer

ZnTe Zinc Telluride

Chapter 1

Introduction

The development of sub-Terahertz (sub-THz) generators and detectors is one of the hot issues in modern Terahertz electronics. Sub-THz lies between 30GHz up to 100GHz. Many applications can be benefit from the generation and detection of THz radiation such as security, medicine, communication, and also remote sensing. The limitation of the sub-THz generator and detector aroused the need to develop devices in terms of power, responsivity, sensitivity, and time response.

With this motivation, the thesis will be presenting work on sub-THz generation and detection in electronic devices using CMOS processes. Silicon devices have an additional advantage since most of the electronic devices foundry and designer in the industry have been exposed in CMOS process. The major emphasis in this thesis is on the design, analysis and implementation of devices in order to generate and detect sub-THz radiation by using a low cost AMS C35 and UMC18 CMOS technology. Two types of devices have been investigated; IMPATT diodes which act as a sub-THz generator and a Metal Oxide Semiconductor Field Effect Transistor or MOSFET acting as a sub-THz detector. Our objectives are to understand, design and measure the properties of sub-THz devices in conventional CMOS process technology.

There are 5 chapters in this thesis. In Chapter 2, a review state of art sub-THz generators and sub-THz detectors is presented. Sub-THz generators discussed on lasers, oscillators, multipliers and THz generation is discussed using semiconductor technology. Besides that, sub-THz detectors discussed on bolometers, golay cells, pyroelectrics, photoconductive antenna, Schottky diodes, and FETs.

In Chapter 3, the theory of IMPATT diodes is presented. The operation and also its efficiency will be discussed as well. Compared to other sub-THz semiconductor devices, IMPATT diode has been chosen because of its capability to generate sub-THz better in terms of resonant frequency and output power in negative resistance. The design's flow for IMPATT diode based on theoretical appreciation, design and experimental assessment will be discussed in this chapter. The designs were made using AMS C35 CMOS technology.

The research continues by looking at detection of sub-THz radiation using Field Effect Transistors (FETs) in Chapters 4 and 5. In Chapter 4, the plasma wave detector by High Electron Mobility Transistor (HEMT) will be discussed. The method of sub-THz detection is different from the previous work because the radiation can be detected quasi-statically. Previously, researchers used femtosecond laser to generate THz pulse radiation, while in these experiments continuous-wave generator will be used to generate sub-THz radiation. There is a clear evidence that sub-THz can be detected using commercial HEMT Avago Technology ATF-36163. In addition, there is also clear evidence that the detection of sub-THz radiation varies based on different frequencies and power.

In Chapter 5, the focus will be on understanding and designing Metal Oxide Semiconductor Field Effect Transistors (MOSFETs) manufactured using CMOS technology as sub-THz detectors. This type should prove to be very cheap in terms of large-scale production. MOSFETs were designed using a conventional CMOS process in AMS C35 and UMC18 CMOS technology. The responses for sub-THz both types of MOSFETs were measured. Experimental evidence shows that MOSFETs can also be used as sub-THz detectors whereby responsitivity will depend on drain current, frequency and input power. Finally, Chapter 6 will summarize the experimental results on generating sub-THz signals and on detecting sub-THz signals using MOSFETs that were designed and fabricated using AMS C35 and UMC18 CMOS technology.

Chapter 2

Sub-Terahertz Technology:

Generation and Detection

2.0 Introduction

In recent years, research in the millimetre wave or sub-terahertz (sub-THz) spectrum has gained interest and can be used in a wide range of applications; communication [1], material identification [2] and atmospheric transmission [3]. In security applications, hazardous agents [4], chemical and biological substances [5] can be detected. There has been substantial growth in interest in security [6] and medical imaging [7]. In the electronic sector, sub-THz radiation has been used in characterisation of semiconductor materials [8] and also in the testing and failure analysis of MOSFETs and VLSI circuits [9].

In this chapter, a brief review of the state of the art of existing sub-THz generator and detectors, both past and present is given. The development in understanding the principle of sub-THz generator and detector will been given.

2.1 Generation of sub-THz radiation

In general, when generating sub-THz radiation in continuous wave (CW) mode, there are two kinds of approaches that can be used; optical and electronic. The optical generation methods of sub-THz include photoconductive antenna [10], optical rectification [11], free electron laser (FEL) [12], optically pumped IR lasers [13] and

quantum cascade lasers (QCL) [14]. While the optical approaches are big, bulky and expensive, researchers and engineers managed to developed compact, small and low cost sub-THz generators by using semiconductor electronics. The miniaturized sources include sub-THz sources that are capable of generating continuous wave (CW) including Backward Wave Oscillators (BWO) [15], frequency multipliers [16], photomixers [17], Gunn diode oscillators, IMPATT diode oscillator [18] and HEMT [19]. There are pros and cons of each sub-THz generator, in terms of power and operating frequency range. Figure 2.1 shows the average power of each sub-THz generator plotted against its frequency of operation.

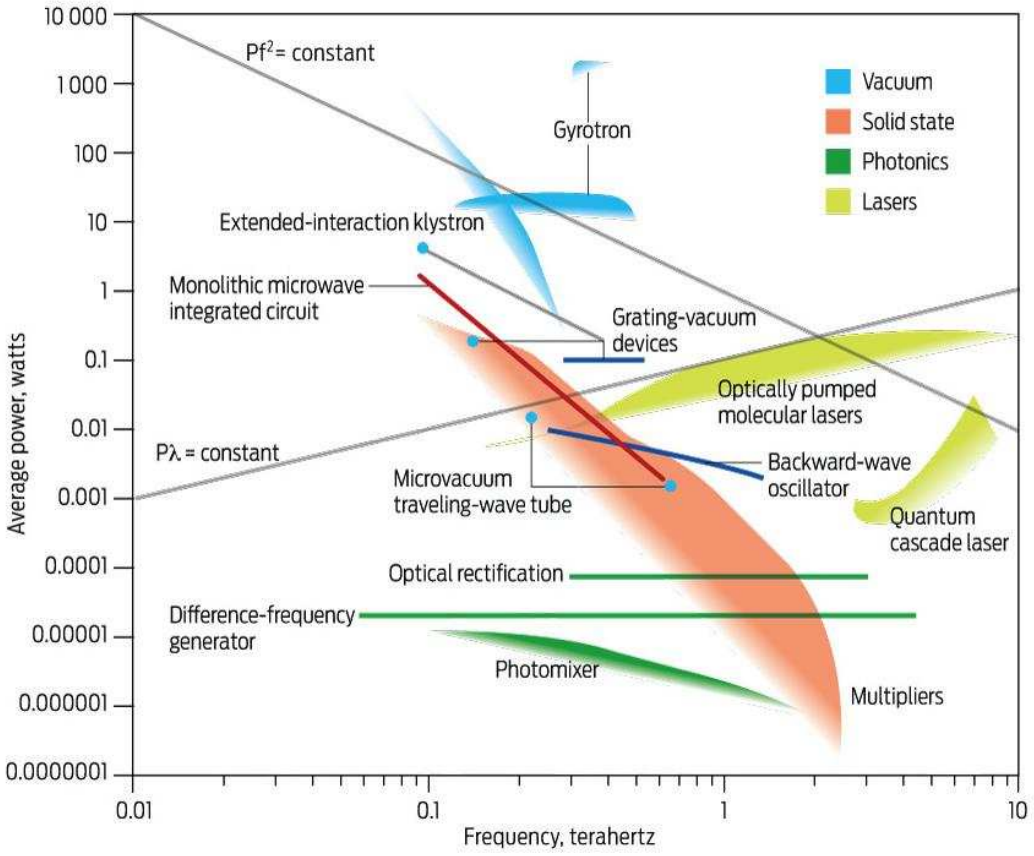

Figure 2.1: Average power comparison versus frequencies for sub-THz devices [20].

Photoconductive antenna

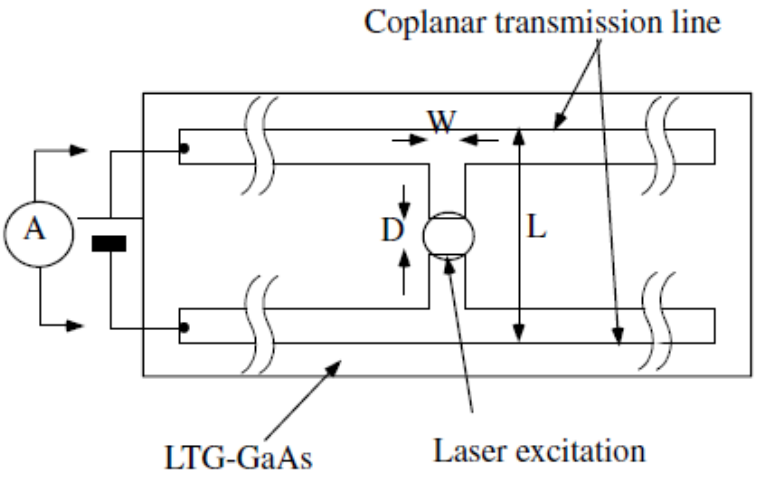

Figure 2.2: Dipole photoconductive antenna [21].

Figure 2.2 shows a schematic of a dipole THz photoconductive antenna. The structure consists of a two micro-strip lines fabricated on a GaAs grown at low temperature so that the material is highly defected using gold as the metallization. One micro-strip is biased with a DC voltage and the other is grounded. Half way along the microstrips, there is a shorting link with a gap in the middle [21]. With a gap at the centre of the antenna, no current will flow through the link. However, when the gap is illuminated with a femtosecond pulsed laser, the excited carriers will reduce the resistance of the gap and current will flow. When the laser pulse ends, the photoexcited carriers quickly recombine, because of the nature of low temperature GaAs, and the current decays rapidly to zero. Consequently the generated current pulses also have a sub-picoseconds temporal response, which corresponds to a

spectral response range of 0.1 to 3.0 THz [21]. The frequencies generated by the photoconductive-switched antennas are higher when compared to other techniques discussed below.

Optical rectification

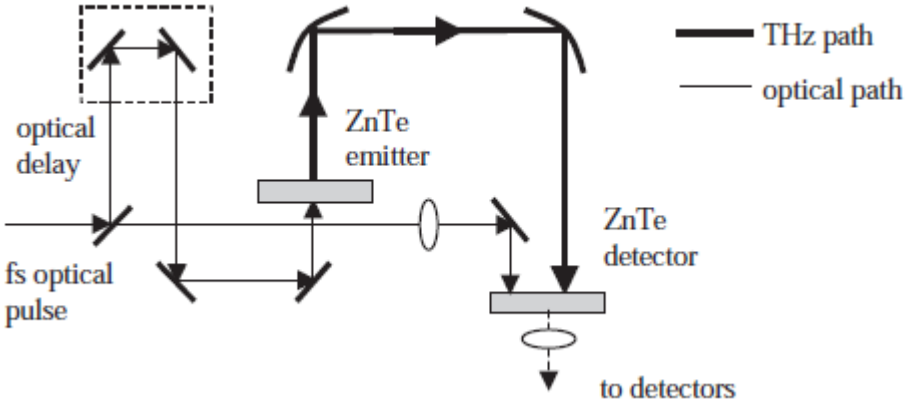

Figure 2.3: Optical rectification [22].

Optical rectification approach as shown in figure 2.3 is a commonly used method since it has both a high signal-to-noise ratio and a very broad bandwidth [22]. THz radiation will be generated by the production of a transient polarization. When femtosecond laser passes through a transparent crystal material such as GaAs, ZnTe, CdTe, or InP, an ultra-short electrical pulse are obtained in THz frequencies without applying any voltage.

Free Electron Laser

Another source of sub-THz is the Free Electron Laser (FEL). Unlike the majority of sub-THz sources, which generate powers in the microwatt to milliwatt range, the FEL can generate radiation with an output power in excess of hundreds of Watts. In a FEL, electrons are accelerated so that their speed is close to the speed of light and then they are sent through a 'wiggler' which is essentially a magnet which forces the electrons to follow sinusoidal path. Even though the electrons have constant speed, their direction of travel changes and hence their velocity. Consequently, the electrons are accelerated and so emit radiation [23].

Optically and electrically pumped lasers

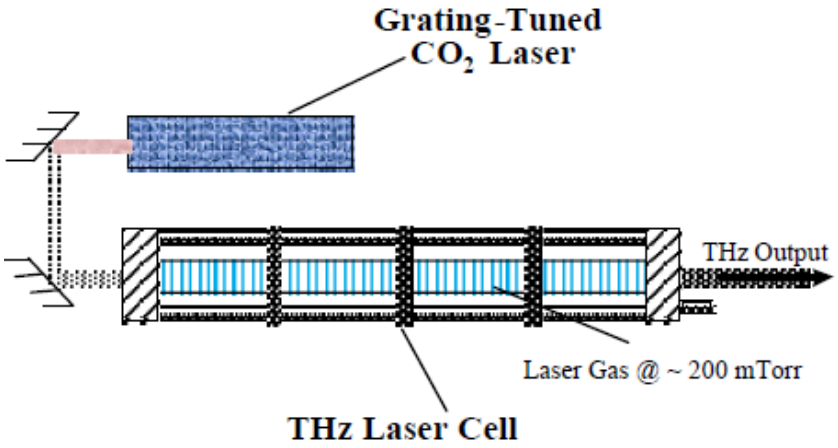

Figure 2.4: Optical pumped laser diagram [24].

Optical pumped lasers, shown in figure 2.4, consists of a THz laser cell, containing a low-pressure molecular gas, which is pumped by a grating tuned CO_2 laser [24]. With this method, THz radiation with output power from milliwatts to hundreds of milliwatts can be achieved [25].

The quantum cascade laser (QCL) is an electrically pump laser and the active region contains repeated a multi-quantum well region where the barriers and wells are identical. Whereas a standard semiconductor laser operates from inter-band transitions from the conduction band to the valence band, the lasing transitions in a QCL are between the conduction band sub bands formed within the multi-quantum well structure. The achievable output power from a QCL is in region of hundreds of milliwatts [26].

Backward Wave Oscillators

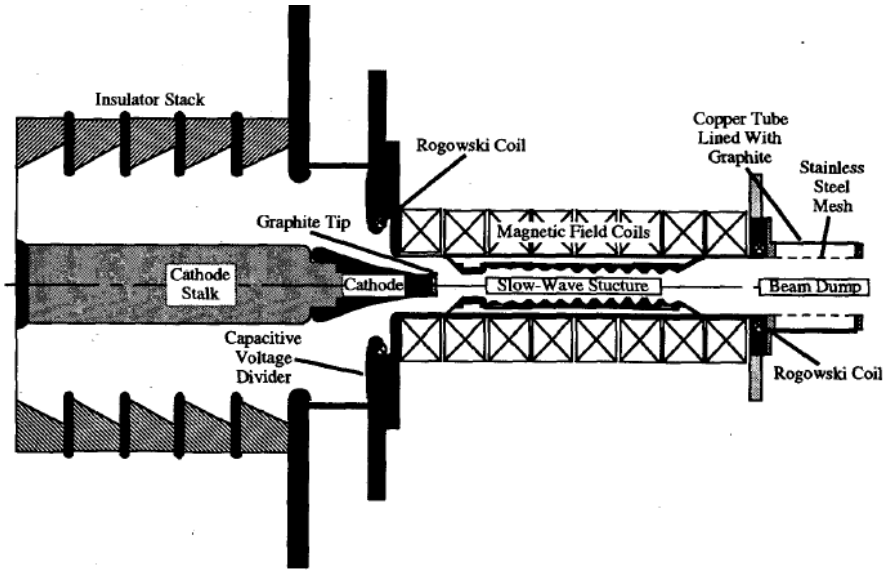

Figure 2.5: Backward Wave Oscillators [27].

Backward Wave Oscillators (BWOs), shown in Figure 2.5, also known as carcinotrons, are slow wave devices where the energy from an electron beam travelling through a slow wave structure in an axial magnetic field interacts with the first spatial harmonic of the backward wave. The electron beam accelerating potential can be used to control the output frequency. In order to extend their frequency range, the output from BWOs can be coupled to non-linear passive or active devices, which multiply the output frequency [27].

Transistor Based Oscillators

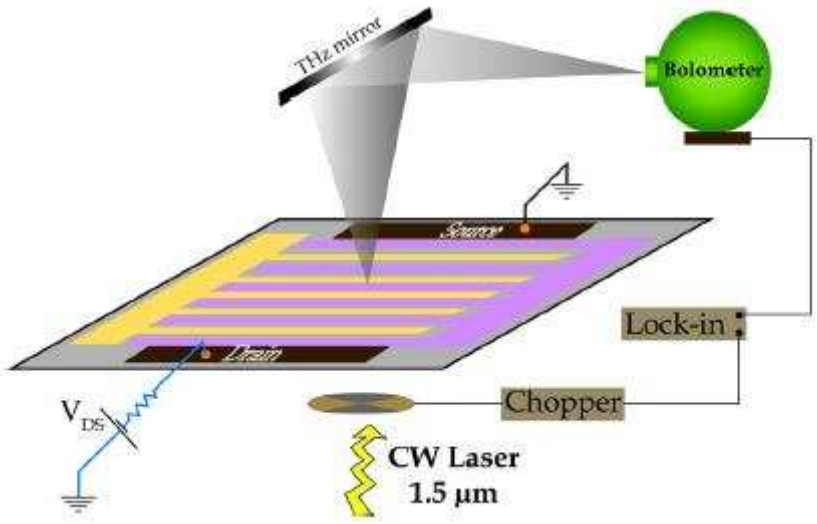

Figure 2.6: HEMT as THz Emitter [28].

Figure 2.6 shows the sub-THz generation setup using High Electron Mobility Transistor [HEMT]. Suemitsu et al, [28] have developed a sub-THz emitter which

converts energy from an infra-red laser operating at 1.5 μm to radiation between 0.5–0.65 THz using a 'double deck' high electron mobility transistor (HEMT). The upper deck HEMT works as a grating antenna where it can radiate the THz radiation by converting the non-radiative plasmonic wave in lower HEMT.

Two terminal solid-state devices

Gunn and IMPATT diodes are the traditional ways of generating sub-THz radiation. Both diode types are biased to operate in the negative differential resistance regions, so a small voltage fluctuation will be amplified with appropriate feedback and oscillations will occur. The frequency of operation depends critically on the structure and doping levels of the material. A. Reklaitis and L. Reggiani have published simulations, which indicate that GaN IMPATT diodes could be useful up to 0.7 THz [29]. In late 2005, Talal Al-Attar [30], managed to fabricate and test IMPATT diodes using 0.25 μm CMOS Technology. Their design is illustrated in Figure 2.7.

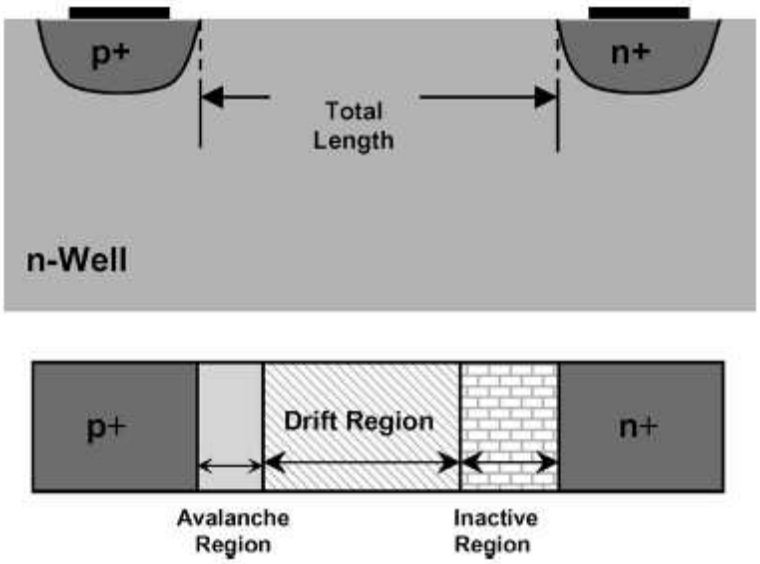

Figure 2.7: IMPATT diode in CMOS process [30].

Frequency multipliers

The frequency of the sub-THz emitters from any of the above sources, especially the IMPATT, Gunn and BWO, can be increased by coupling the radiation into a non-linear device such as Schottky diode. In principle frequency multiplication is a promising method of generating THz, however, there are drawbacks: the output power will reduce after each multiplication stage and so the output power is limited by the source power and thermal power capacity of the multiplier.

2.2 Detection of sub-THz radiation

Since the emitted powers of sub-THz signal are weak, detection of THz signals is difficult. The performance for each detector is measured via responsivity and sensitivity. Responsivity relates the output signal of the detector to the incident

power. Therefore, the more responsivity a detector has, the greater the output for a given incident power. Sensitivity of a detector refers as the minimum incident power, which can be detected and is closely related to the output noise of a device. Signal-Noise-Ratio (SNR) plays an important role for the detector since the higher the SNR, the better the detector would be.

There are three different approaches to sub-THz detection. Firstly, for detection of ultra-short pulses, it can be done using two methods; photoconductive sampling using photoconductive antenna as shown in section 2.1, and the other one by using Free-Space-Electro-Optic-Sampling (FS-EOS). FS-EOS detects the polarization change of the probe beam induced by THz electric field through the Electro-Optic (E-O) effect in the sensor crystal. Since the E-O effect is almost instantaneous on the THz time scale, especially in compound semiconductors, FS-EOS gives a signal directly proportional to the THz electric field [31]. Figure 2.8 shows an example of FS-EOS THz detector.

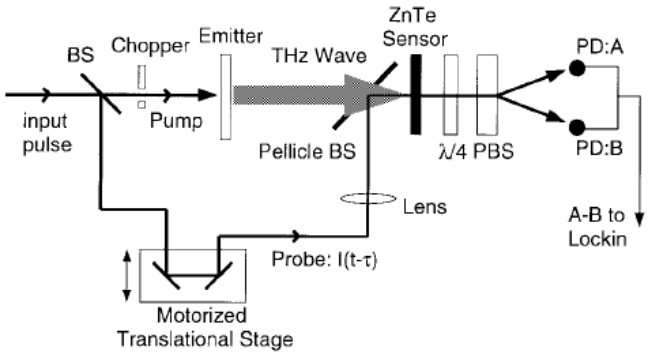

Figure 2.8: Setup for FS-EOS THz waves detector [31].

The second types of sub-THz detection are by mixing and down conversion of two signals, the incoming THz radiation and a local oscillator (LO) signal as shown

in Figure 2.9. The LO has a different frequency but with a fixed output power which is much greater than the power of the incoming signal. The frequency is proportional to the difference between the frequencies of the incoming THz signal and the LO; the frequency of the output signal is called intermediate frequency (IF).

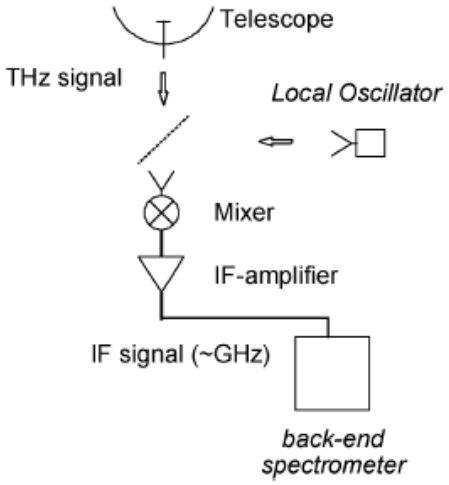

Figure 2.9: Schematic diagram for heterodyne receiver technique [32].

Some other devices with this type of detection are Schottky diodes [33], High Electron Mobility Transistors (HEMTs) [34], and Metal Oxide Semiconductor Field Effect Transistors (MOSFETs) [35]. The detection mechanism is directly related to the mixing process.

The third approach to detecting sub-THz signals is by direct detection, where the THz signal is directly detected through the interaction with the physical properties of the devices. Bolometers and microbolometers [36], Superconducting Tunneling Juctions (STJ) [37], Golay cells and pyroelectric devices [38] are the examples of direct detection.

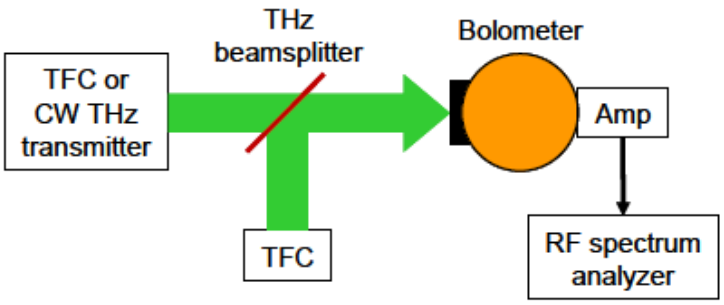

Figure 2.10: Schematic diagram for THz measurement using TFC and bolometer [39].

Figure 2.10 shows a schematic diagram of the THz measurement based on Terahertz Frequency Comb (TFC) and bolometer. The resistance of the bolometer is a function of temperature. The detector works by using the absorption of THz radiation increasing the bolometer's temperature and hence resistance. These devices operate at cryogenic temperatures (~4 K and below), and are very sensitive but in terms of time response, they are very slow. Another approach for THz detection is by using Superconducting Tunnel Junctions (STJ), which relies on photon-assisted tunnelling process that operates at cryogenic temperatures [40].

For commercial THz detection, room temperature operation is required. Golay cells operate at ambient temperature but again rely on the change of temperature when THz radiation is absorbed. This time it is the gas in a gas cell. As the temperature increases, the gas pressure increases and distorts a mirror, which is detected optically. Again Golay cells suffer from a poor time response.

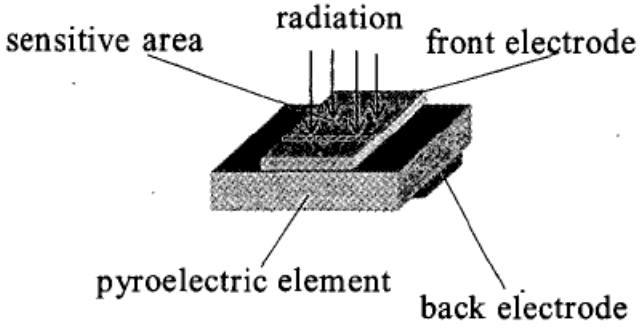

Figure 2.11: Setup for pyroelectric detector [41].

Pyroelectric devices operate in the same way but the physics is different as shown in Figure 2.11. The temperature is detected by either small voltage changes across the device or by current flow to equalising changes in the pyroelectric charge. In terms of response time, pyroelectric devices are better than other detectors but it is still in the order of milliseconds, but the drawback is that the pyroelectric detector is less responsive compared to bolometer and Golay cells.

An example of a semiconductor THz detector is Schottky diode where it responds to THz radiation due to rectification of the incident radiation. R. Han et. al reported that they had fabricated Schottky diodes in 0.13 µm CMOS process and characterized them in terms of photo detecting where the radiation power that had been measured was 28 mW [42].

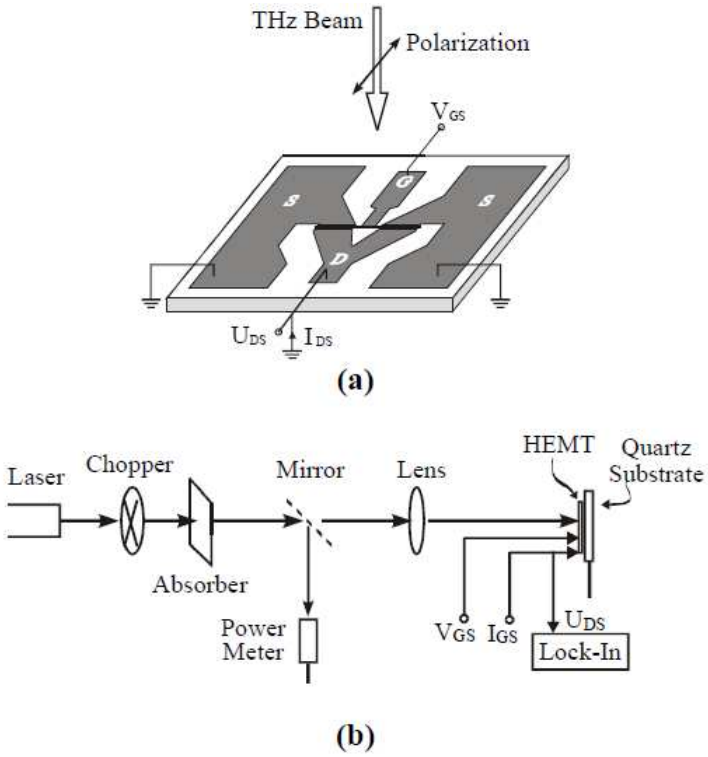

Figure 2.12: (a) Sub-THz detection using HEMT (b) Experimental setup for sub-THz detection [43].

Figure 2.12 shows a generic experimental setup for detecting sub-THz radiation. Sub-THz detectors using plasma waves in FETs was originally proposed by M. S. Shur et. al [43] where the detection of terahertz is caused by the nonlinear properties of the transistor channel where the incoming signal will lead to rectification of an ac current induced by the THz radiation. Hence, the photoresponse will appear in the form of DC voltage between source and drain. This phenomenon is based on 'shallow water analogy' for ballistic transport of electrons in short channel (FET), as the gate of the transistor decreasing, this FETs channel behaves as a resonator at Terahertz frequencies [43].

2.3 Generation and detection of sub-THz in University of Nottingham

The previous sections have outlined the state of the art for sub-THz generation and detection. The objective of the research in University of Nottingham was to fabricate sub-THz generators and detectors using standard CMOS technology. The sub-THz generator was based on IMPATT diode and for the THz detector, the plasma wave detector was used. Each of the devices is explained in individual chapters in this thesis. The aim of this research is to investigate the generation and detection of sub-THz devices especially in IMPATT diodes and FETs as sub-THz generator and detector.

Chapter 3

Sub-Terahertz Generator:

Impact Avalanche Transit Time (IMPATT) diode

3.0 Introduction

Two terminal devices are still the favourite choice for the generation of millimetre wave and sub-THz signals. One of the most powerful sub-THz sources are IMPATT diodes. IMPATT stands for 'Impact Ionization Avalanche Transit Time or 'IMPATT' for short. This diode acts as a signal generator with an operating frequency range from 30 – 300 GHz. IMPATT diodes employ both impact ionization and transit-time effects to give negative resistance at microwave frequencies. The oscillation of microwave in an IMPATT diode was discovered in 1965 by Johnston, De Loach and Cohen [44] but the theory was originally developed in 1958 by Read [45]. Since then, several of the structures of Read Microwave Avalanche Diode [46] or IMPATT have been reported, mesa, planar, distributed and lateral [47]. In early works on IMPATT diodes, there was a problem in terms of power dissipation, where researchers managed to resolve the problem by mounted the diodes on special diamond or copper heat sink [48 - 49]. Later on, C.J. Schoellhorn et al proposed a p^+-n, n^+ stack with n-doped avalanche and drift regions. The structure was grown using molecular beam epitaxy (MBE) [50]. Recent works suggest IMPATT diodes can be fabricated using standard CMOS process technology [51-52]. The advantages of IMPATT diodes are their small size and lightweight compared to other sub-THz sources.

However, the noise of IMPATT diodes is high and they are sensitive to operating conditions. The design of the biasing network is critical to avoid device blowing out. These diodes are used in many applications such as in automotive radar, communications, and security.

The IMPATT diode is essentially a p^+ - n - n^+ junction operating under high reverse bias so that avalanche occurs. The depletion region can be broken down into two regions, the avalanche region where carrier multiplication occurs and the drift region where the carriers move through the depletion region. Figure 3.1 shows a single drift IMPATT diode.

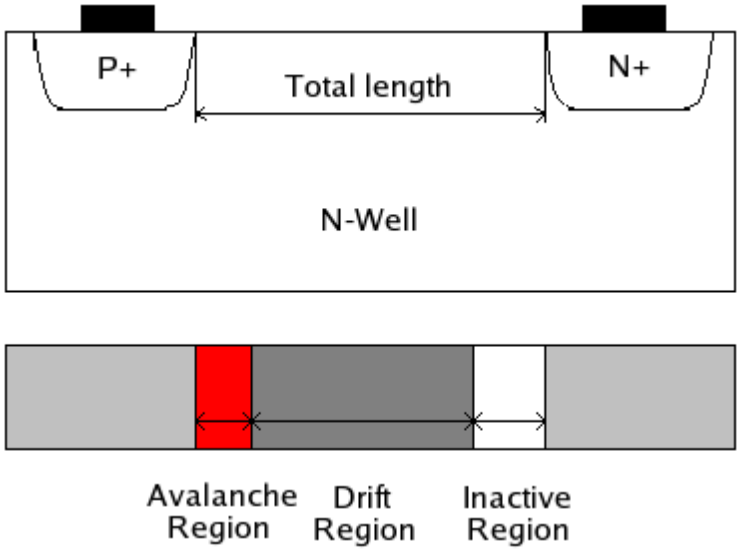

Figure 3.1: Single Drift IMPATT diode.

The avalanche region is the region where the diode acts, as the source where the impact multiplication occurs, is restricted to a very narrow region close to metallurgical junction. The ionization rates are very sensitive to the magnitude of the field. In silicon, electron ionization rate (α_n) is larger than holes ionization rates (α_p) [53]. In other semiconductors the ionization rates for electrons and holes are the same. As the field increases above 10^5 V/cm, the impact ionization occurs, and electrons moving into depletion region have sufficient energy to excite an electron from the valance band to the conduction band. This process is called Avalanche multiplication.

The drift region is the depletion layer where it excludes the avalanche region; the important thing in this region is carrier drift velocity. Minimum carrier transit-time across the drift region can be obtained by increasing the electric field so that the carriers generated can travel at their constant velocities; υ_d for the silicon is above $1x10^4$ cm/s. The field across the drift region is above 5 kV/cm [54]. When the electric field reaches maximum, the generated carriers with saturation velocity will travel through the drift region with minimum transit time [55].

3.1 IMPATT diode Principle of Operation

The IMPATT diodes in CMOS process consist of 3 parts; p^+ - n - n^+. Whenever the diode is supplied with reverse bias voltage, a very high electrical field will occur between p^+ - n. As a result, a thin layer of avalanche region will occur as shown in figure 3.2 (b). At this moment avalanche multiplication process begins with

generating holes-electrons pairs. Then, the generated holes will be quickly will be attracted to p^+ while generated electrons will be attracted to n^+ by passing through drift region. This process will produce external power.

Whenever the electric field is low, the average drift velocity is directly proportional to the field. As the electric field in this region keep increasing until the field is high enough, the generated carriers will travel with a very minimum transit time through the drift region with saturation velocity υ_s [51]**:-**

$$\upsilon_S = I/\rho A \tag{3.1}$$

where I is space charge current, ρ is the carrier charge density, and A is the diode area.

The total field across the diode is the sum of the dc field and ac fields. During the positive half of the ac voltage cycle given to the diode, the breakdown voltage occurs caused by the total field across the p^+ n-well junction. When the field is above the breakdown voltage, at the p^+ n-well junction the carrier current $I_o(t)$ will be generated by the avalanche multiplication where it grows exponentially with time as seen in figure 3.2 (d). As for the negative half cycle, when the field is below the breakdown voltage, the carrier current $I_o(t)$ will decrease exponentially to a small steady state level. The carrier current $I_o(t)$ will form a short pulse in term of time.

The carrier current $I_o(t)$ will reach the peak value at the middle of the ac voltage cycle, or one quarter of a cycle after the voltage. As the electrons flows in space-charge regions, the generated holes are injected into the space-charge region and towards n^+ region. When the injected holes traverse the drift region, they induce a current $I_e(t)$ in the external circuit. The drift velocity for the holes into the space-

charge region is constant, the induced current $I_e(t)$ in the external circuit is simply equal to [52]:-

$$I_e(t) = \frac{Q}{t} = \frac{\upsilon_d Q}{L} \tag{3.2}$$

where ;

Q = total charge of the moving holes

U_d = hole drift velocity

L = length of the drift region

Analysis of the IMPATT diode shows that the induced current $I_e(t)$ from the small signal analysis that had been done by Read [45] gives the expression for resistance of the diode :-

$$R \sim \frac{W}{A\varepsilon_s \omega} \frac{1}{1-\frac{\omega^2}{\omega_r^{\,2}}} \left(\frac{1-\cos\theta}{\theta} \right) \tag{3.3}$$

where W is the depletion width, A is the diode area ε_s is the dielectric permittivity, θ the transit angle and ω_r is the avalanche resonant frequency that given by [52]:-

$$\omega_r = \sqrt{\frac{2\alpha' \upsilon_s J_o}{\varepsilon_s}} \tag{3.4}$$

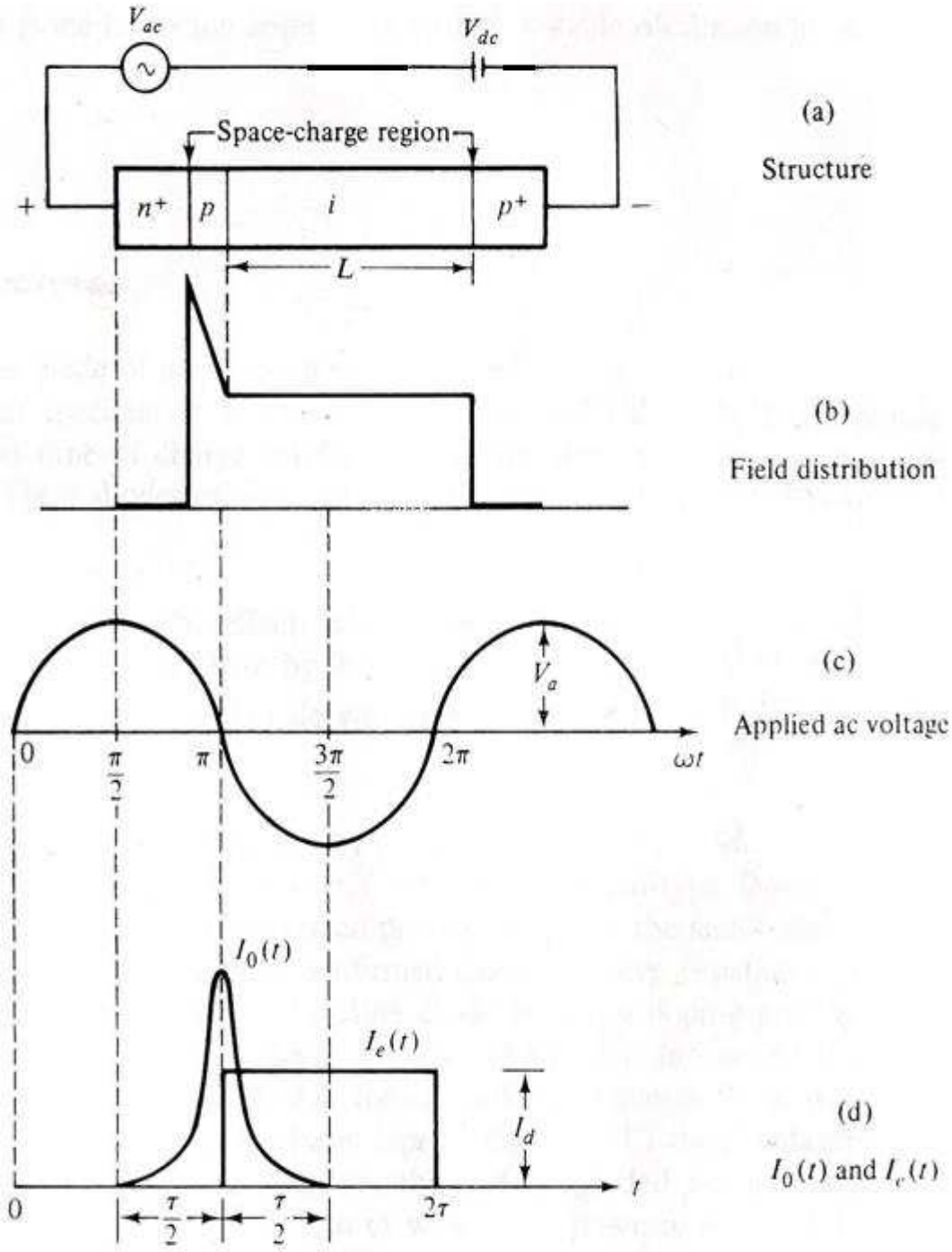

Figure 3.2: IMPATT structure, field distribution, AC voltage and current [45].

where α' is the derivative of the ionization rate based on electric field and J_o DC current density. As we can see from equation (3.4), the resistance can only be negative when $\omega > \omega_r$.

Negative resistance occurs in an IMPATT diode by two following effects; the impact ionization avalanche effect where it causes the carrier current and the ac voltage to be out of phase by 90 degree and the transit time effect which gives another delay for external currents and the ac voltage to be out of phase by 90 degree. This will give 180-degree phase difference between voltage and current and will be resulting negative resistance [55]. Negative resistance is also related to avalanche frequency, where the relation between avalanche frequency and current density is given by Schoellhorn [52]:-

$$f_A \propto \sqrt{J} \tag{3.5}$$

where f_A is the avalanche frequency and J is current density.

In terms of efficiency, for an ideal IMPATT diode, the ratio of AC voltage to applied voltage is 0.5 while the ratio of AC and DC current is about $2/\pi$ about more than 30%. But unfortunately, in reality, the efficiency of IMPATT diode is usually below 30% because of the following effects; high frequency skin effect, space charge effect, reserve-saturation-current effect and ionization-saturation effect [55].

3.2 Design methodology

3.2.1 Design process for IMPATT diode

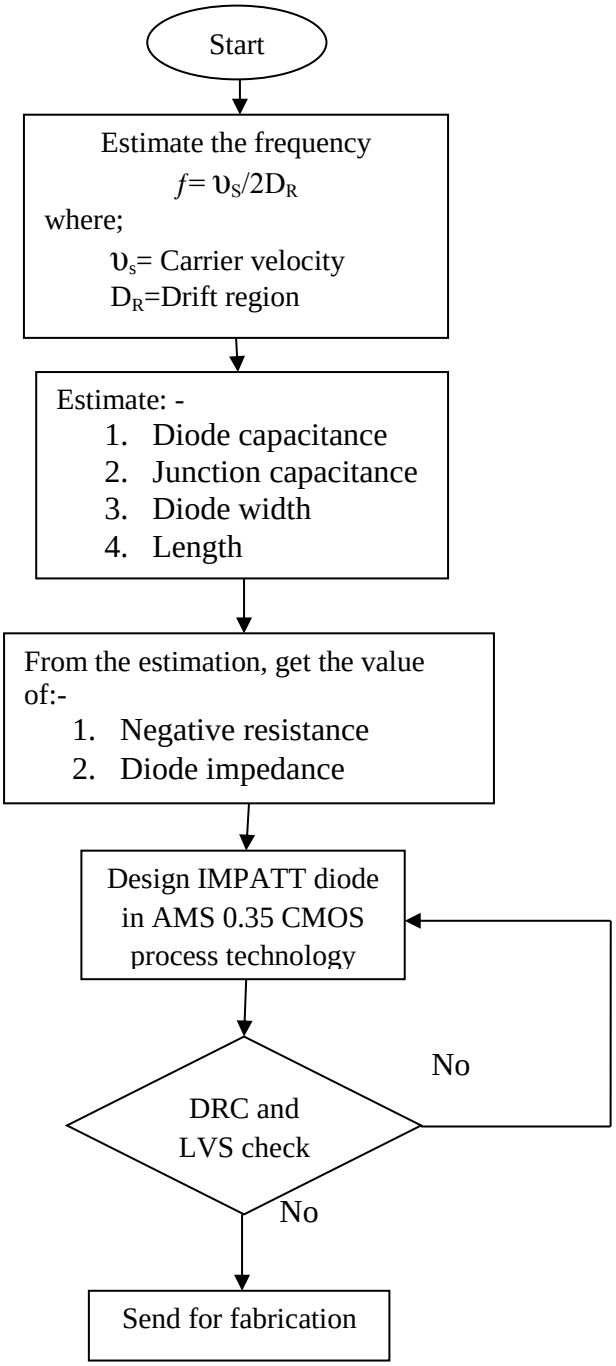

Figure 3.3: Process of designing IMPATT diodes.

Based on the flowchart in figure 3.3, the design on IMPATT diode will be explained in this section. In designing on the IMPATT diode, the design/target frequency should be achievable with the CMOS process technology. Our objective was to investigate and design an IMPATT diode using the C35 CMOS process. The depletion width can be estimated by fixing the frequency at 30 GHz based on equation below [55]:-

$$f = \upsilon_S / 2D_R \tag{3.6}$$

where f is the avalanche frequency, υ_S is silicon carrier velocity and D_R is the distance of the drift region where we estimated the distance between p^+ and n^+ as 1.667 µm. Then, using the negative resistance for IMPATT diode equation as shown in equation 3.2, we simulated equation (3.6) and the results are shown in Figure 3.5.

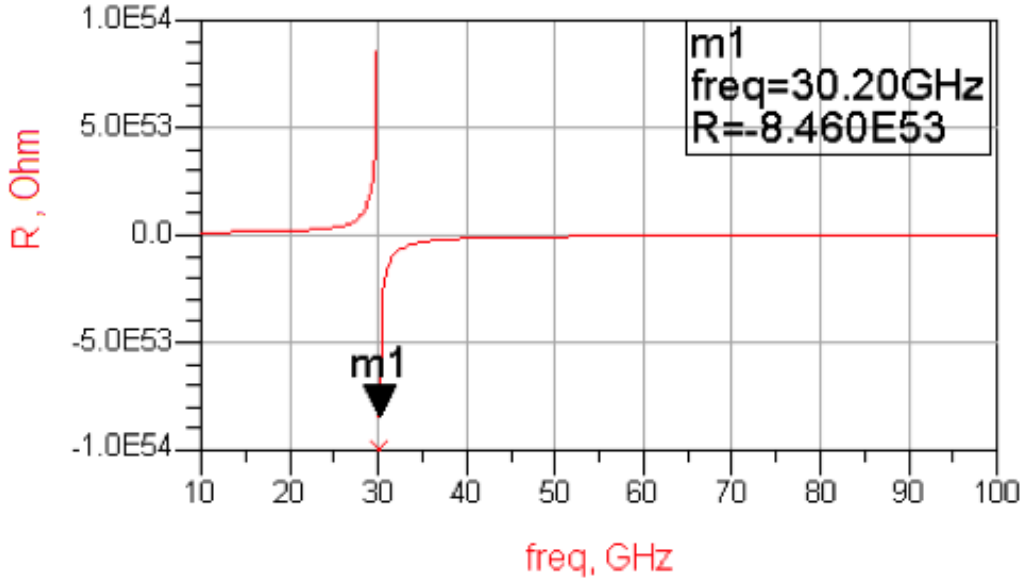

Figure 3.4: Negative resistance in IMPATT operation.

By using ADS2006A, the estimation for the negative resistance at 30 GHz is about -8.460 x 10^{53} Ω as seen in Figure 3.4. This simulation results showed that the IMPATT diode could produce a negative resistance as an effect of impact ionization in the avalanche region.

Later on, after estimation of the frequency, the design of the diode was continued by designing a diode layout using Cadence C35 process. The diode layout and diode schematic was designed using Virtuso Cadence with the design kit provided by Austria Micro System (AMS) C35 CMOS technology. The designs are checked with the Design Rules Check (DRC) and the Layout Versus Schematic (LVS) tools in the software. DRC will determine whether the physical layout of a particular chip layout satisfies with recommended parameters called design rules. The LVS verification is to compare the netlist file from the layouts design with the netlist for the schematics.

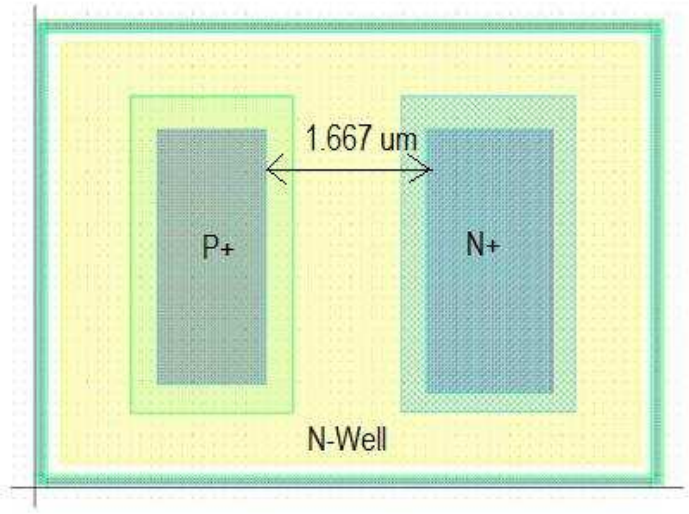

Figure 3.5: Layout for IMPATT diode 120 µm x 50 µm.

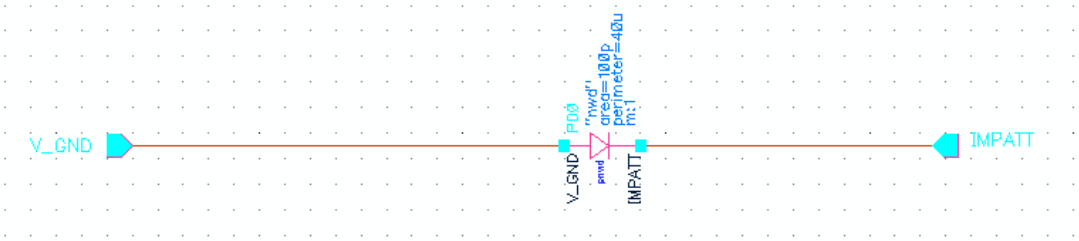

Figure 3.6: Schematic for a single IMPATT diode.

From Figure 3.5, the size of the IMPATT diode layout is 120 µm x 50 µm where the separation between p^+ and n^+ was 1.667 µm to get a resonant frequency at 30 GHz. The schematic of the diode was designed using Virtuso Cadence schematic and the process of LVS (Layout versus Schematic) was done to make sure that the netlists of the layout and the schematic were the same. If errors appeared, redesigning the layout or schematic was done until no errors appeared. Figure 3.6 shows the schematic figure for a single IMPATT diode.

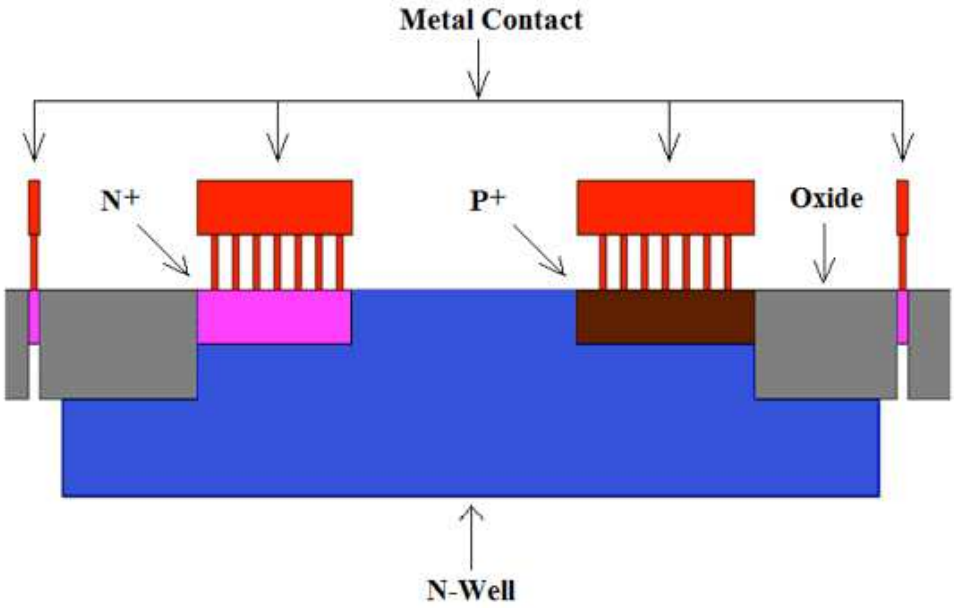

Figure 3.7: Cross section for IMPATT diode.

Figure 3.7 shows the cross section of the IMPATT diode by using AMS 0.35 μm CMOS process. On top of the p^+ and n^+, there are metal connections to RF pads for biasing purposes. Three RF pads were designed to connect and bias the diode. The layout of RF pads with IMPATT diode is shown in Figure 3.8 and the IMPATT diodes have been integrated with a coplanar waveguide as seen in Figure 3.9.

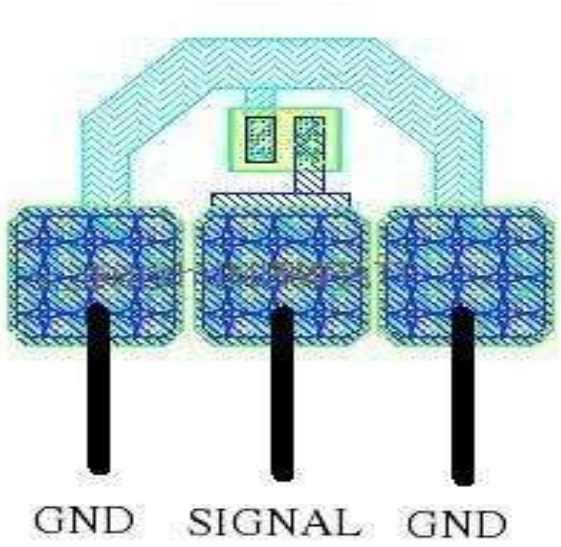

Figure 3.8: Layout for a single IMPATT diode with RF pads (G-S-G).

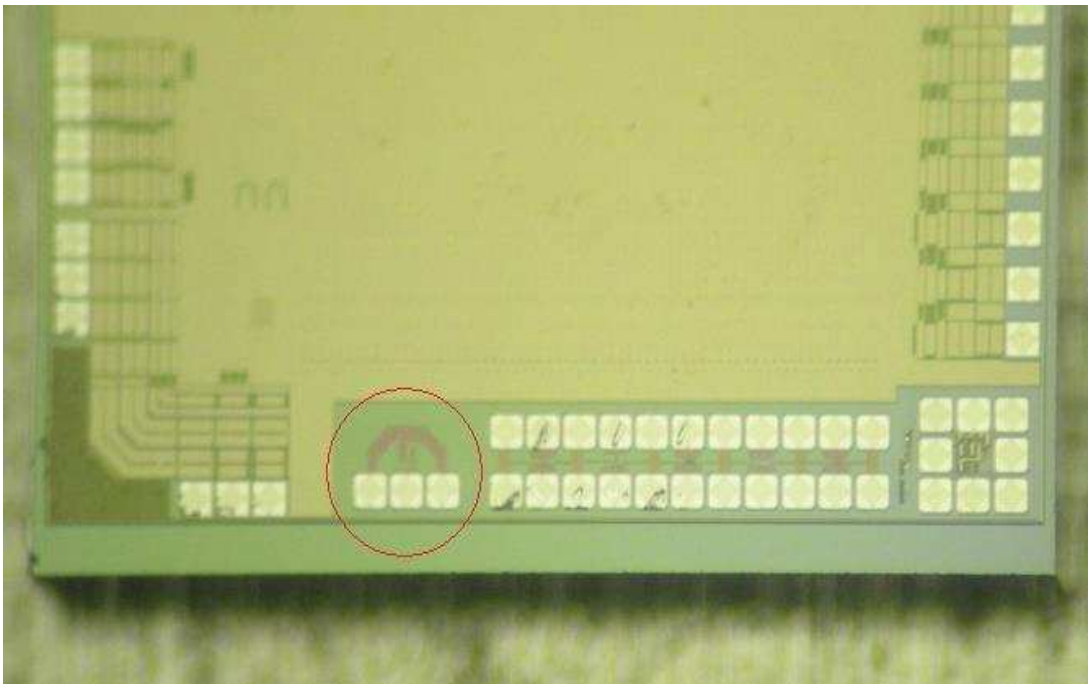

Figure 3.9: IMPATT diode in AMS C35 chip with RF pads (G-S-G).

3.2.2 Calibration and De-Embedding Technique

A two-step calibration procedure was used to measure the on-wafer S-Parameters. Firstly, a Short-Open-Load (SOL) calibration using a CS-5 precision calibration substrate provided by Picoprobe was done. Then, to remove the effects of the pads, a de-embedding technique using open-end and short-circuit de-embedding structures [56] was carried out. More information about the de-embedding procedure can be found in Appendix.

3.3 Experimental Procedure

3.3.1 Experimental setup

The IMPATT diode was fabricated by AMS C35 CMOS technology and tested in the RF Engineering Lab at room temperature. The equipment involved included the Anritsu Broadband Vector Network Analyser, 100 μm pitches G-S-G RF probe test bench, Keithley 236 and 237 programmable voltage source, digital multimeter and the Olympus 20x microscope.

The fabricated chip with IMPATT diodes was placed on the top of XYZ Probe station, so that the 100 μm pitch G-S-G RF probe could be easily placed on to the appropriate pad which allowed connections to the signal and ground pads. The biasing was supplied by Keithley Source Measurement Unit model number 236 directly into the RF probe using a bias-T. The S-Parameters were measured by using the signal 100-μm pitches G-S-G RF probe where the probe was attached to the Anritsu Broadband Vector Network Analyser 40 MHz-65 GHz. The experimental setup and a picture of the test bench are shown in Figures 3.10 and 3.11.

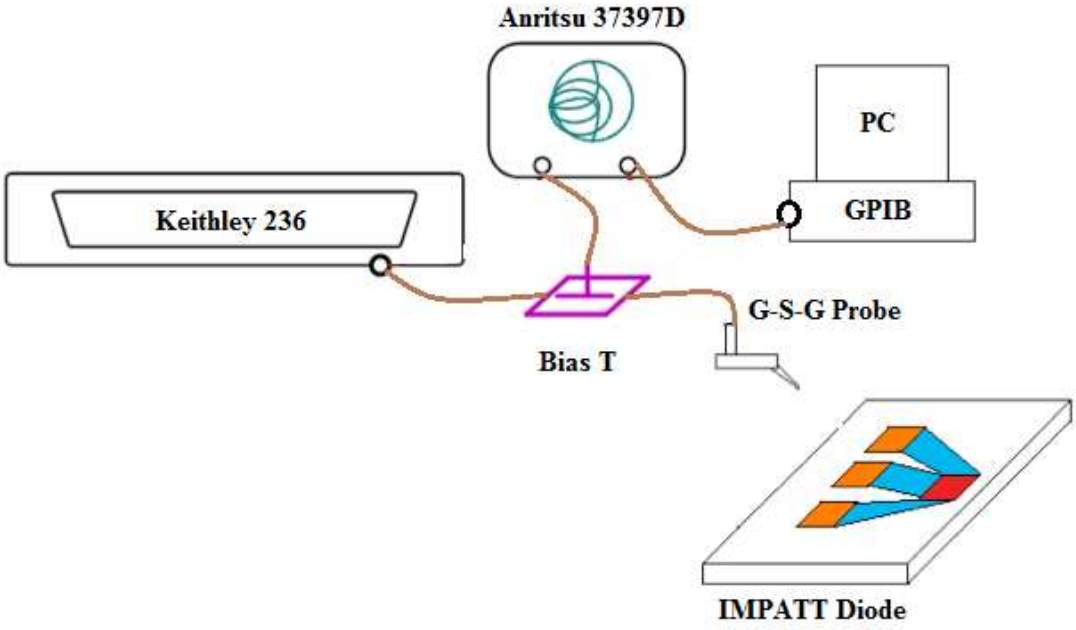

Figure 3.10: Experimental setup for IMPATT diode.

Figure 3.11: IMPATT diode experiment test bench.

3.3.2 IV and S-Parameter experiment using LabView

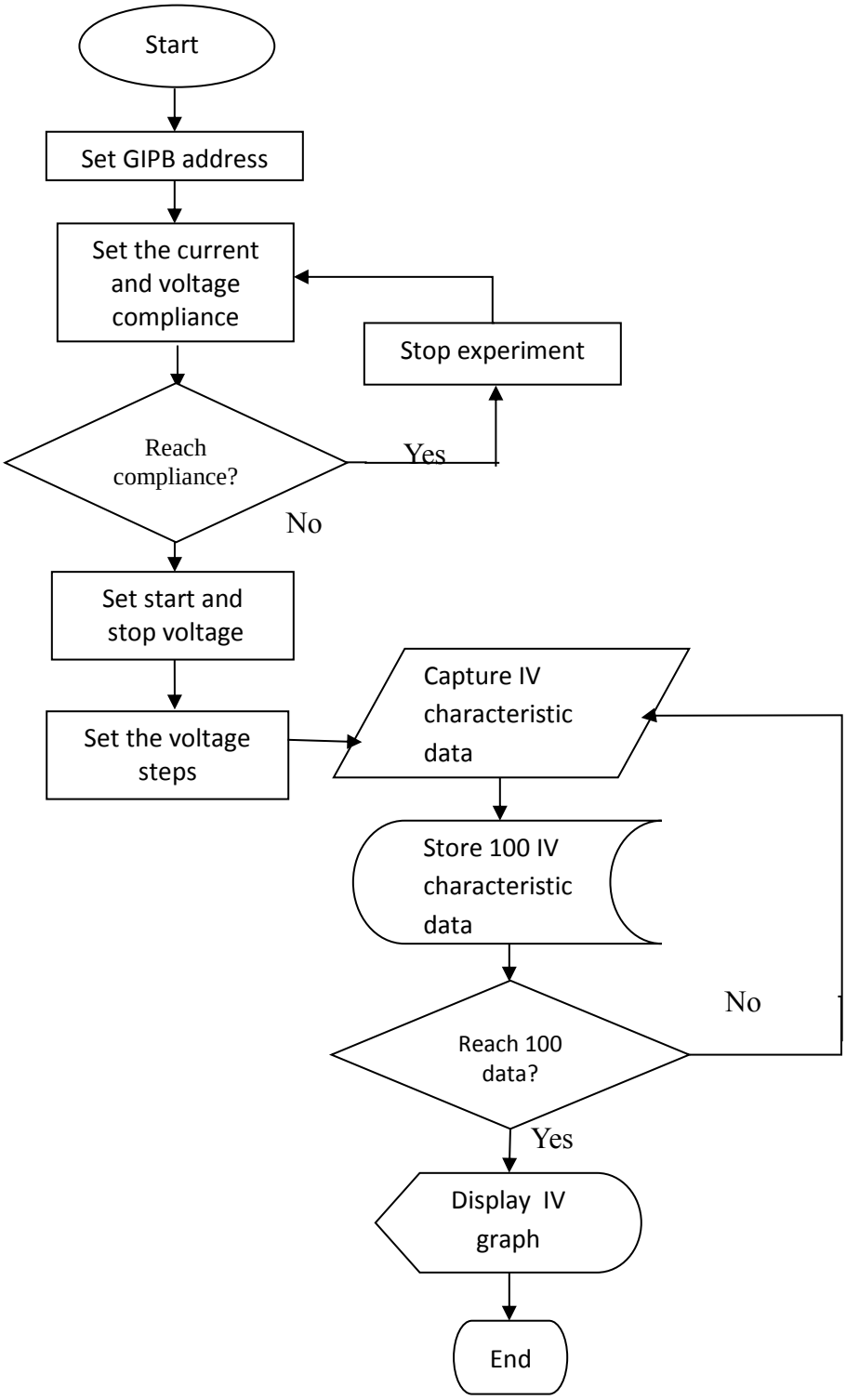

Figure 3.12: Flowchart for IMPATT diode IV experiment using LabView.

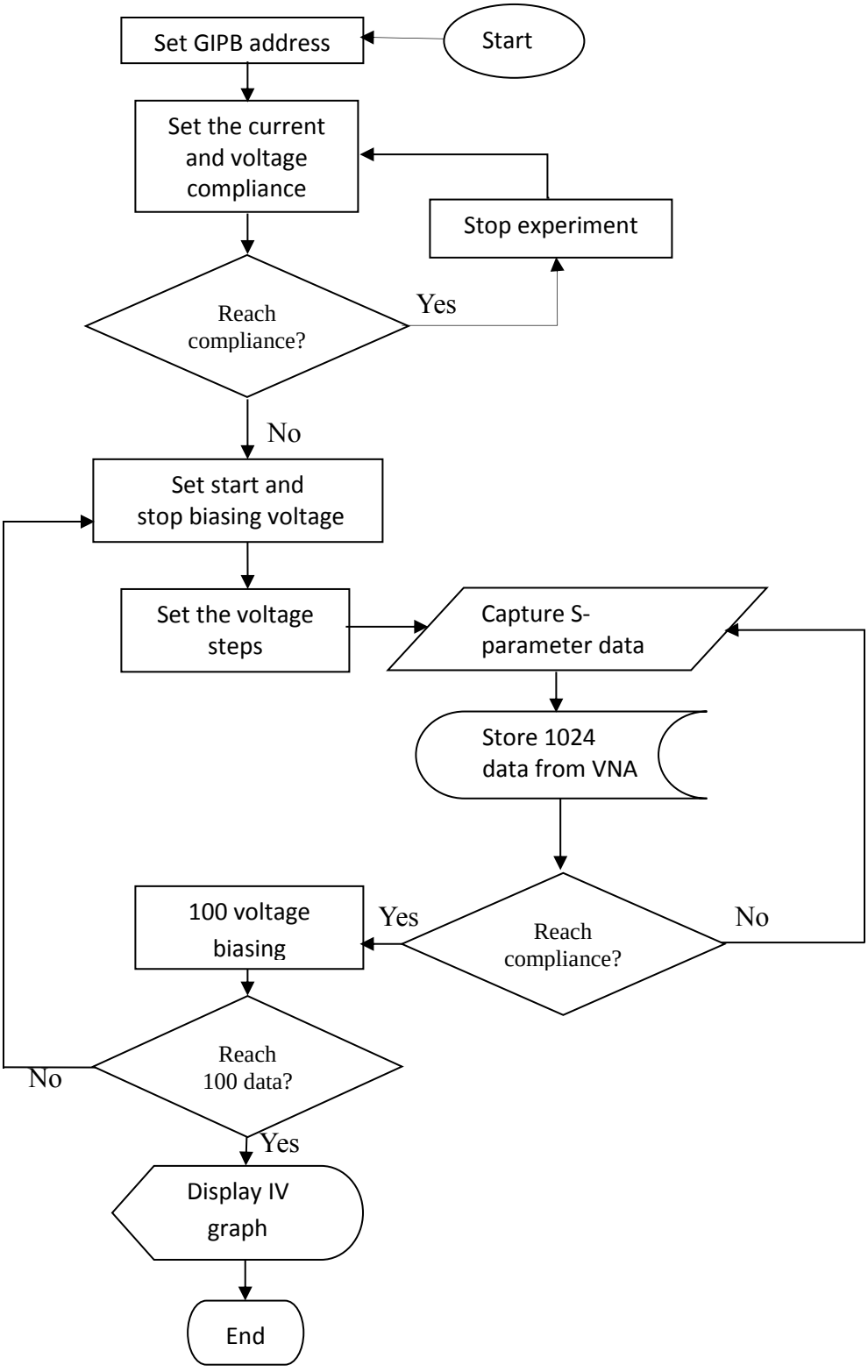

Figure 3.13: Flowchart for IMPATT diode S-Parameter experiment.

The flowchart for IV characteristic of IMPATT diode is shown in Figure 3.12. The development of this program was based on LabView 8.5 [57] with NI-USB-GPIB interface device. This interface device is used to connect LabView with all instruments with GPIB addresses. Each controller needs to initialize based on their GPIB address. For Keithley 236 the GPIB IEEE address is 16. The current and voltage compliance of the Keithley was set to protect the device from overload and potential destruction. Then IV data was captured and stored inside a table in the LabVieW program until the data count up reached 100.

Figure 3.13 shows the measurement procedure for S-Parameter measurements of IMPATT diodes in a flowchart. In the beginning, the Keithley 236 was set using the GPIB address. Then the voltage and current compliance were set for IMPATT diode protection. The voltage biasing was set from 0V up to -18V since the IMPATT diode operates at negative voltage. Once the voltage steps were chosen, the S-Parameter from VNA from 40 MHz to 65 GHz were captured and stored in the program. The process was repeated until the IMPATT diode reached a resonant frequency at 30 GHz and for biasing up to -12 V. All measurement process was done 100 times so that the data captured was accurate. Later on, after the experimental process finished, the S-Parameters data were extracted using ADS2006A.

3.4 Results and discussion

3.4.1 DC Characterization

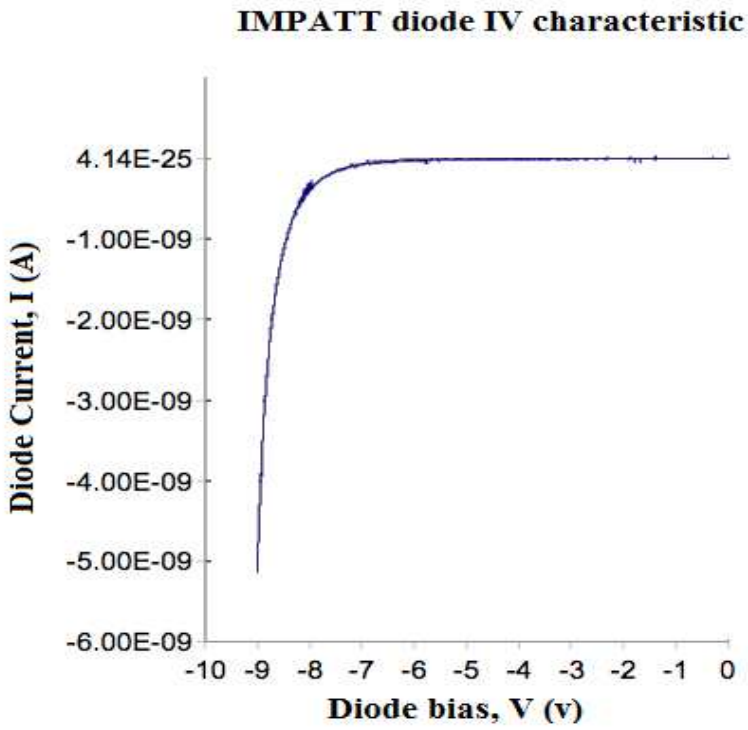

Figure 3.14: IMPATT Diode IV characteristic.

The IV characteristic of the device was measured before the RF measurements were taken. A typical IV characteristic is shown in the figure 3.14. In IMPATT diode, the reverse current of the IV characteristic is the interesting part as IMPATT diode is operating in avalanche region. The IMPATT diode starts to breakdown at -7.1V with -0.123 nA. The operation of IMPATT diode started after the breakdown voltage.

3.4.2 RF Characterization

Figure 3.15: IMPATT diode with active area (p^+) 12 um x 25 um = 300 um^2.

The IMPATT diodes were integrated with coplanar waveguide as seen in Figure 3.15 with diode active areas of 12 um x 25 um. Coplanar waveguide consists of a strip of the metallic film on the surface of a dielectric slab with two ground electrodes running adjacent and parallel to the strip [58]. The RF characterization of the IMPATT was done by using S-Parameter measurement from 40 MHz – 40 GHz by biasing at negative voltage from 0 V to -12 V. The RF measurements were divided into two sets of experiements. At first, the experiment was with no illumination, where the experiment was performed in a dark room with all the experimental setup was inside the black box. During the second experiment, the IMPATT diode were tested with illumintaion where the test bench was in ambient light. The S-parameter

measurement results for IMPATT diode are shown in Figures 3.19 to 3.24. The magnitude and phase before and after the breakdown voltage were analyzed .

3.4.2.1 RF Characterization for IMPATT diode without illumination

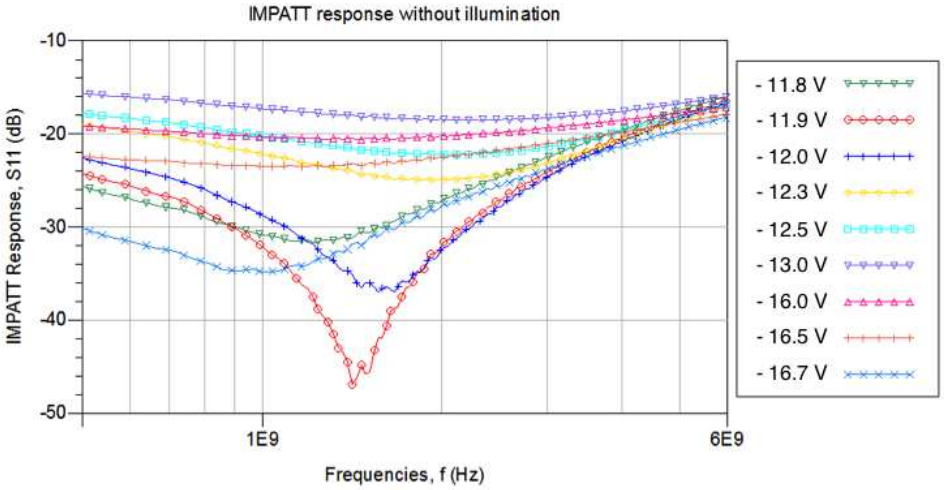

Figure 3.16: IMPATT response without any illumination.

Figure 3.16 shows IMPATT response, S11 due to voltage biasing from 0 V up to -16.7 V without illumination condition. From the graph, as the IMPATT was biased from 0 V to -16.7 V, it can be seen that before the diode achieved the breakdown voltage, no resonant frequency was observed. As the voltage was raised above the breakdwon voltage, at V= -10 V, the IMPATT diode started to oscillate. During oscillation, the field in IMPATT diode increases above 10^5 V/cm, where impact ionization occurs. At this stage, electrons moving into depletion region have sufficient energy to excite an electron from the valance band to the conduction band [48].

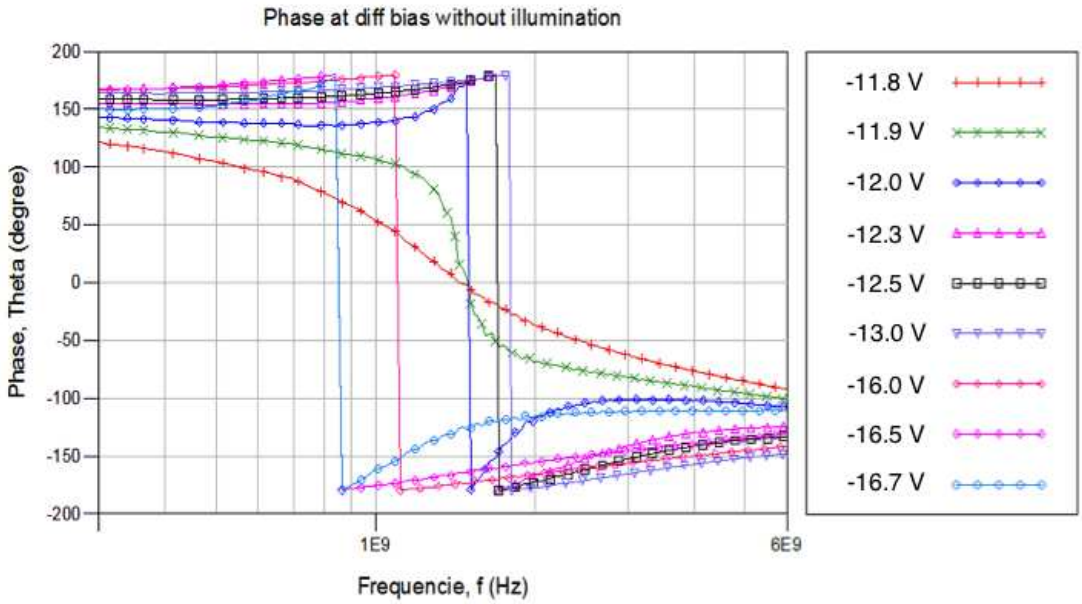

Figure 3.17: IMPATT diode phase different without any illumination.

As the biasing to the IMPATT diode increasing towards negative voltage, the maximum avalanche frequency that can be observed was at -11.9 V for 1.414 GHz. The zero degree phase crossing was observed where the frequency referred to as avalanche frequency f_A developed as the resonance took place. Showing the phase relationship with biasing as shown in Figure 3.17 can reveal the avalanche frequency for IMPATT diode.

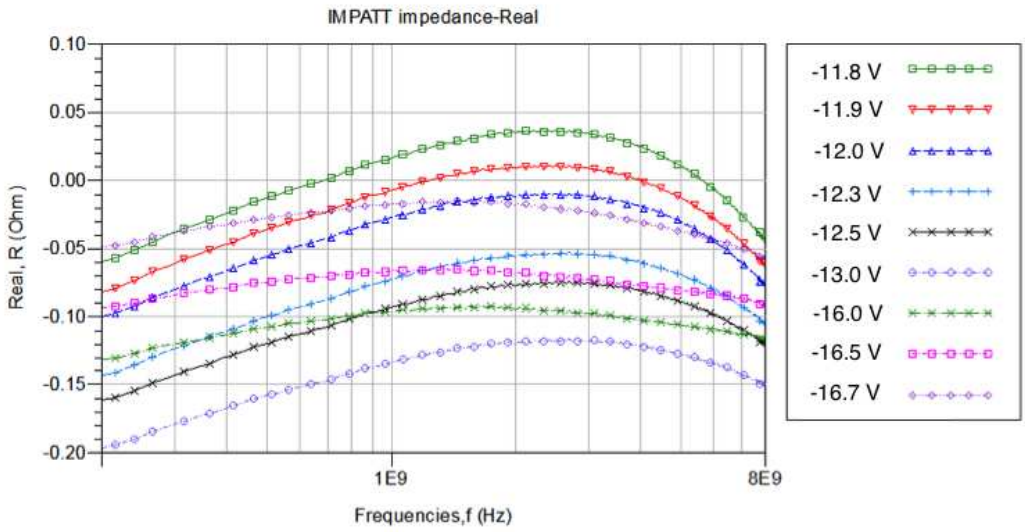

Figure 3.18: IMPATT negative resistance with no illumination.

Figure 3.18 shows the IMPATT diode negative resistance versus frequency. It shows that the negative resistance occurs when avalanche frequency took place. In this experiment, we can observe that the value for the negative resistance is 10 mΩ when the IMPATT diode was biased at -11.9 V. One important point in here, although the result for negative resistance was not achieved, still the avalanche frequency occured when the IMPATT diode was biased appropriately.

3.4.2.2 RF Characterization for IMPATT diode with illumination

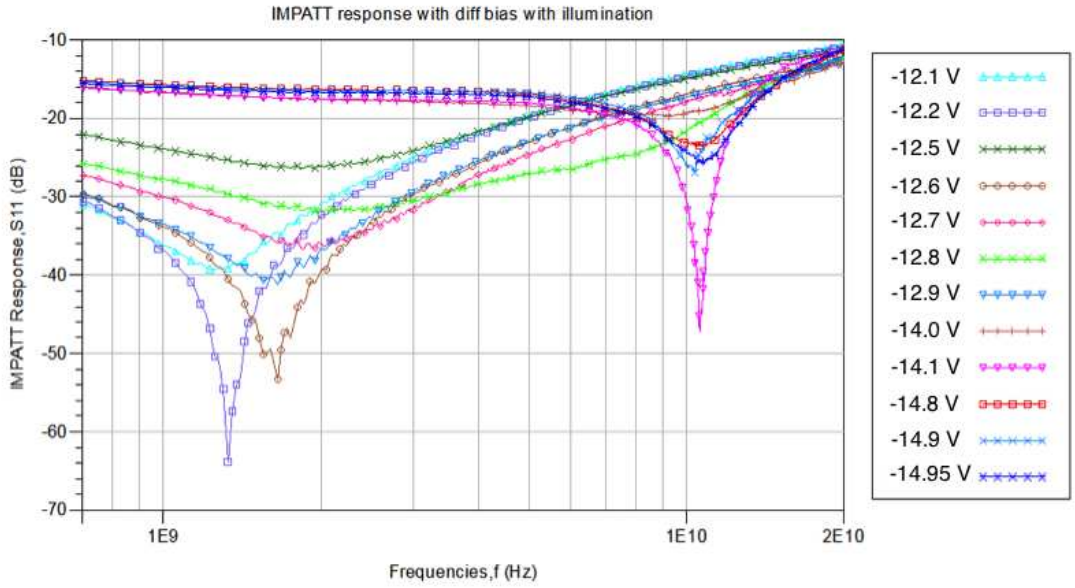

Figure 3.19: IMPATT diode response with different bias with an illumination.

The second experiment was done by illumintaing the IMPATT diode with the bias voltage above the breakdown voltage. From Figure 3.19, the observation was made about the IMPATT diode response by avalanche frequency at 1.327 GHz with bias at -12.2 V with -63.844 dB. We know that as the biasing increased, the current density also increased. This impacted the IMPATT reponse S11, where it also increased from 1.327 GHz, with biasing at -12.2 V with -63.844 dB to 1.627 GHz, with biasing at -12.6 V with -51.099 dB and increasing the resonance to 10.56 GHz with biasing at -14.1 V at -45.214 dB. This response was due to the avalanche effect. Previously, IMPATT diode operation had been observed starting at -10 V without illumintaion condition. In this experiement with illumination, the IMPATT diode resonant peak was observed at -12.2 V.

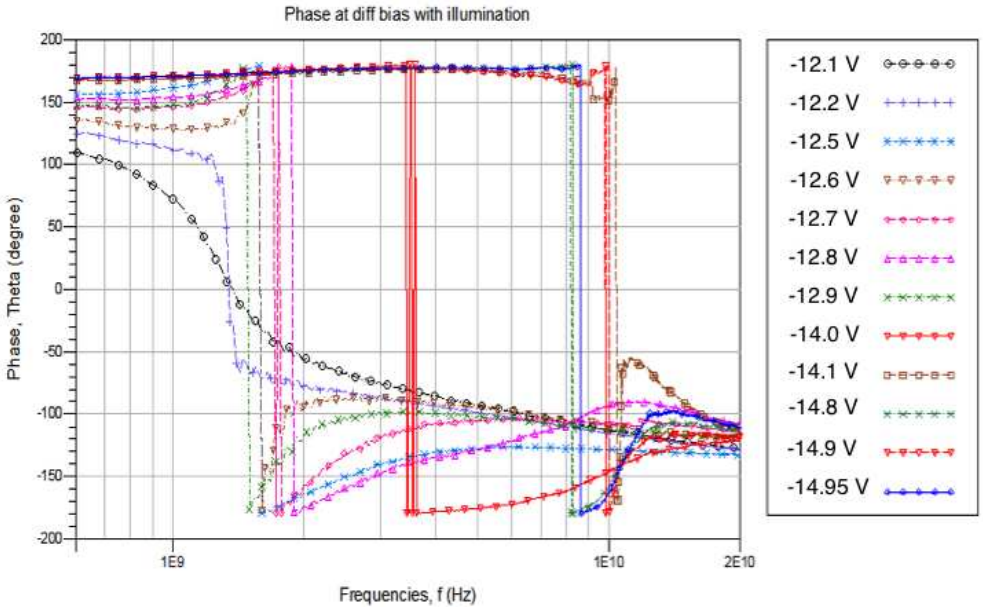

Figure 3.20: IMPATT phase with different bias with an illumination.

As the resonance occured, zero degree phase crossing was observed as shown in Figure 3.20, which is referred to as avalanche frequency f_A. When the IMPATT diode was biased at -12.2 V, it was expected to produce 180° phase shift with negative resistance at the avalanche frequency. From Figure 3.20, with biasing start at -12.2 V to -12.6 V and -14.1 V, a 180° phase difference was measured. We know that as the voltage increased, the current also increased and this relates back to the Read [45] equation 3.5 from the previous section. It can be seen that by increasing the current densities, it automatically increases the voltage, and it also increases the avalanche frequency. As the current densities get larger, it will increase the IMPATT diode self-heating and so will increases its temperature. As temperature increases, the diode area becomes overheated and at the end the diode will be burn out.

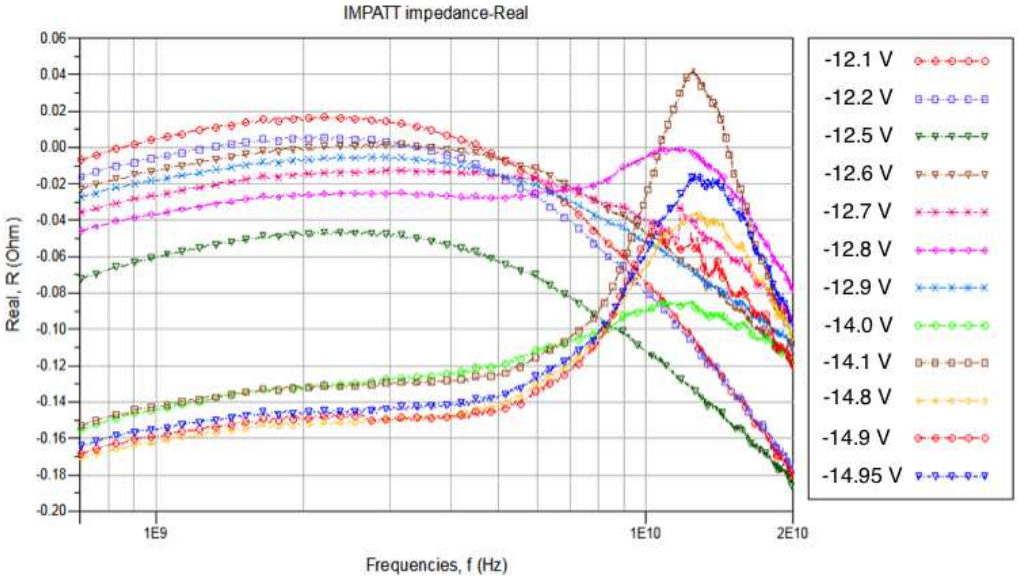

Figure 3.21: IMPATT diode resistance with illumination.

The impedance (negative resistance) of the IMPATT diode was next observed. From Figure 3.21, the resistance was observed to be about 11 mΩ at 1.327 GHz with biasing at -12.2 V when the resonance started. As the biasing increased up to -12.5 V, the resistance was -180 mΩ at 20 GHz. This experiment is a proof that IMPATT diode can achieve negative resistance although it happened after the avalanche frequency.

In these results, a resonant frequency did occur but the value of the negative resistance was too small in milliOhms. There are several explanations which are put forward. Firstly, the technology used to build up the IMPATT diode was totally different. Previous work on silicon IMPATT diode was done by two different groups with different techniques. C.J. Schoellhorn et al. using molecular beam epitaxy (MBE) technique to growth high quality layer of p^+ - n - n^+ stack for single IMPATT

diode [52]. Talal Al-Attar et al. built an IMPATT diode in 0.25 μm CMOS process technology [51], while in these experiment the AMS C35 CMOS technology were been used. All these technologies have different doping profiles and junction capacitances that affect the resonance frequency at different avalanche and drift regions and also breakdown voltages. In AMS C35 CMOS technology, the minimum space between p^+ and n^+ that can be achieved in this technology is 1.43 μm where in theory the avalanche frequency could be transpire at 35 GHz.

3.5 Conclusion

Monolithic integrated IMPATT diode was designed and fabricated using AMS C35 CMOS technology. Experiments for characterization of the IMPATT diode were done using IV characteristic and S-Parameter measurement techniques. Based on the measurements, the avalanche frequency for the IMPATT diode without illumination were observed at 1.414 GHz and with illumination, the observation were made at 12.2 GHz, 12.6 GHz and 14.1 GHz. Further, as the bias are increased, the IMPATT diode burn out. Based on the experimental results, it was shown that, the IMPATT diode could be used as sub-THz sources up to 35 GHz by using AMS C35 CMOS technology.

Chapter 4

Sub-Terahertz Detector:

Field Effect Transistor (FET)

4.0 Introduction

Terahertz (THz) technology is one of the evolving technologies that will help in changing our life. A lot of applications, such as medicine [59], security [60], astronomy [61], biology [62], and non-destructive materials [63] testing have been demonstrated recently. The developments of sensitive and compact THz detectors are important for these technologies advancement. However, there are a few challenges in realization of compact THz detectors because of the frequencies are too high for conventional electronics and the photon energies are too small for classical optics. As a result, THz radiation is resistant to the techniques commonly employed in these well-established neighbouring bands [64]. Many different types of THz detectors have been developed such as bolometers [65], pyroelectric detectors [66], Schottky diode [67], photoconductive detectors [68] and most recently is plasma waves detectors in Field Effect Transistors (FETs) [69]. The detection of THz by FETs is one of the promising technologies that can be both selective and tuneable [70]. Recently, experimental evidence on detection of THz signal was demonstrated in commercial AlGaAs/GaAs FETs [71], AlGaN/GaN HFETs [72], a double quantum well FET with periodic grating gate [73] and MOSFETs [74].

In the beginning of ‘90s, THz generation and detection using FETs was initiated by Dyakonov and Shur [75] where they predicted that a steady current flow in an asymmetric FET channel could lead to instability against spontaneous generation of plasma waves. This will lead into producing the emission of electromagnetic radiation at the plasma wave frequency. Later on, it was explained in [35], that the detection of terahertz radiation is a result of non-linear properties of the transistor channel by rectifying incoming radiation and as a result, a photoresponse appears in the form of dc voltage between source and drain, which is proportional to the radiation power (photovoltaic effect).

In order to understand plasma waves, Shur [75] explained that plasma waves was generated within the device channel from modulation of electron concentration and hence produced a THz response. The decreasing in electron concentration, made an excess of positive charges, attracting electrons nearby. These electrons move towards positive charges, but due to their inertia, these electrons overshoot the charge location. As these electrons got attracted to opposite direction, again they move in and overshoot the charge location. This phenomenon with oscillations of electron density is called plasma waves.

The plasma waves in gated two-Dimensional Electron Gas (2 DEG) propagate at much faster velocity rather than electron drift velocity propagation; hence the rectification by plasma waves can be used as radiation detection in THz frequencies region. A resonant cavity by a gated channel of a FET allowing resonant detection of sub-THz and THz radiation is described [76]. Several factors in determining the resonant frequencies need to be taken into account such as electron concentration in

the channel and its length, the electron concentration and geometrical parameters of the V_{GS} (voltage gate source) and V_{DS} (voltage drain source) regions. The gate voltage changes the electron concentration under the gate and, therefore, can tune the resonant plasma frequencies. The FET plasma frequency can reach THz range as the carrier densities on the order of 10^{12} cm^{-2} and the gate length going into submicron region [77].

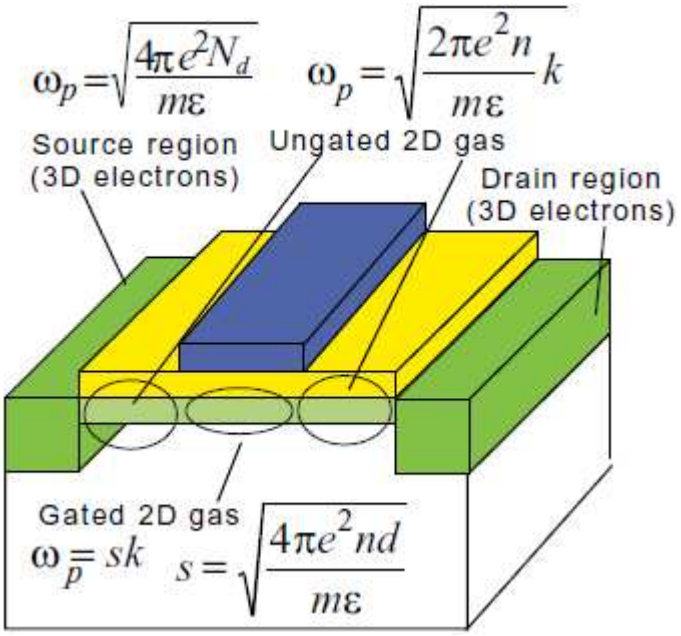

Figure 4.1: Frequencies of plasma oscillations (ω_p) vs wave vector (k) [78].

Figure 4.1 shows the dependencies of plasma frequencies in 3D, ungated 2D and gated 2D regions. In the figure above *m* is the electron effective mass, ε is the dielectric permittivity of semiconductor, *N* is the bulk electron concentration in alloyed regions, *n* is the sheet electron concentration for channel regions, where it is

proportional to the gate voltage bias.

Plasma waves in FETs have a linear dispersion law. Discontinuities at the end of the 2 DEG channel reflect the waves. At certain frequencies the reflected and the original wave will be in phase and resonance will occur [35] as shown in equation (4.1).

$$\omega = sk \tag{4.1}$$

where $s = [e(V_G - V_{TH})/m]^{1/2}$ is the plasma wave velocity, e is electron charge , V_G is gate voltage, V_{TH} is threshold voltage and m is electron effective mass. At a given gate length, L_g acts as a resonant response at plasma frequencies $\omega_N = \omega_O(1+2n)$, where n = 0,1,2,… and ω_O is the fundamental plasma frequency as :-

$$f_0 = \sqrt{\frac{e(V_g - V_{th})}{m}} \Big/ 4L_g \tag{4.2}$$

This equation has two important consequences; the sufficiently short (submicron) FET's gate length will increase plasma wave resonant frequency of detection can be tuned along with gate voltage [70].

The plasma wave resonant frequency against channel length is shown in Figure 4.2 on a log plot. Several interesting points to note: the resonance frequency increases as the channel length decreases, and the frequency for GaN and GaAs is higher than silicon. This is because the saturated drift velocity or mobility is higher in these compounds.

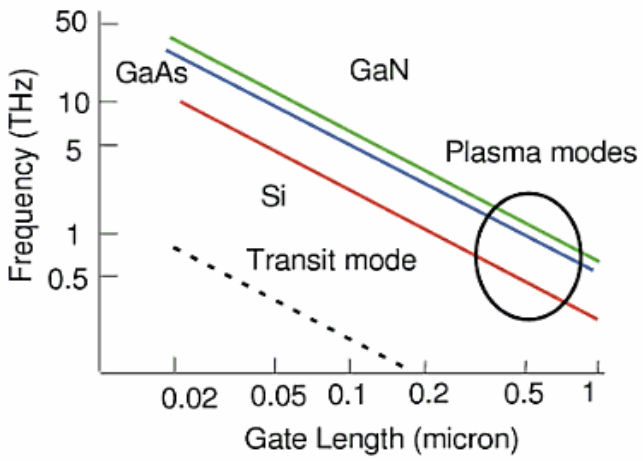

Figure 4.2: Plasma wave and transit regime comparison for THz frequency vs gate length of several semiconductor materials [78].

Previous THz detection work using High Electron Mobility Transistors (HEMTs) [71] showed that a resonant detection of THz frequency occurs when a constant drain current was applied. The plasma relaxation rate is affected by the drain current by driving the two-dimensional plasma in the transistor channel towards plasma wave instability [69]. THz detection by GaAs/AlGaAs high electron mobility transistor (HEMT) was reported in 2001 where researchers used a commercial HEMT (Fujitsu FHR20X) as a resonant THz detector [71]. P.J. Burke et al. shows that the impedance of high electron mobility transistors (HEMT) exhibits maxima at the fundamental plasma frequency and its harmonics [79]. Lu et al. have proposed and demonstrated that photoresponse will rise when the drain current is increasing and this effect also happens because of the increasing asymmetry in plasma wave. Figure 4.3 shows the previous work on the drain current effect [80]:-

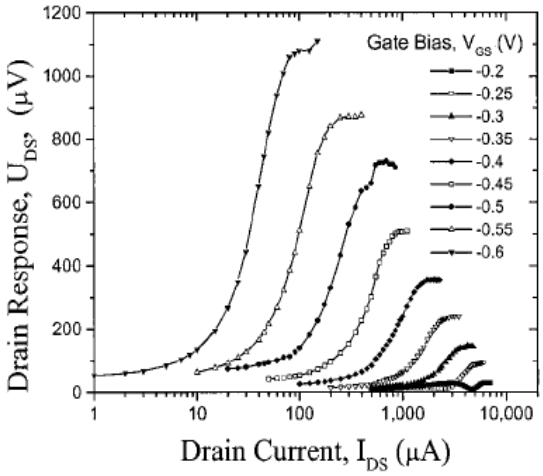

Figure 4.3: Photoresponse versus drain current (I_{DS}) at different gate biasing (V_{GS}) at 2.5 THz [80].

Sub-THz detectors based using FET is an interesting topic to be explored further. The key factor for doing this work was to develop a novel THz detection design based on interaction with plasma waves by experimenting it using HEMTs and also using MOSFETs in CMOS technology. In the Photonic and RF Engineering Group (PRFEG), School of Electrical and Electronic Engineering, University of Nottingham, opportunities have been taken to explore the FET devices act as sub-THz detector. Hence, with this motivation the development of sub-THz detector board based on commercial HEMT will be designed, fabricated, tested and discussed in this chapter.

4.1 Design Methodology

4.1.1 Design and experimental flowchart for HEMT as Sub-THz detector

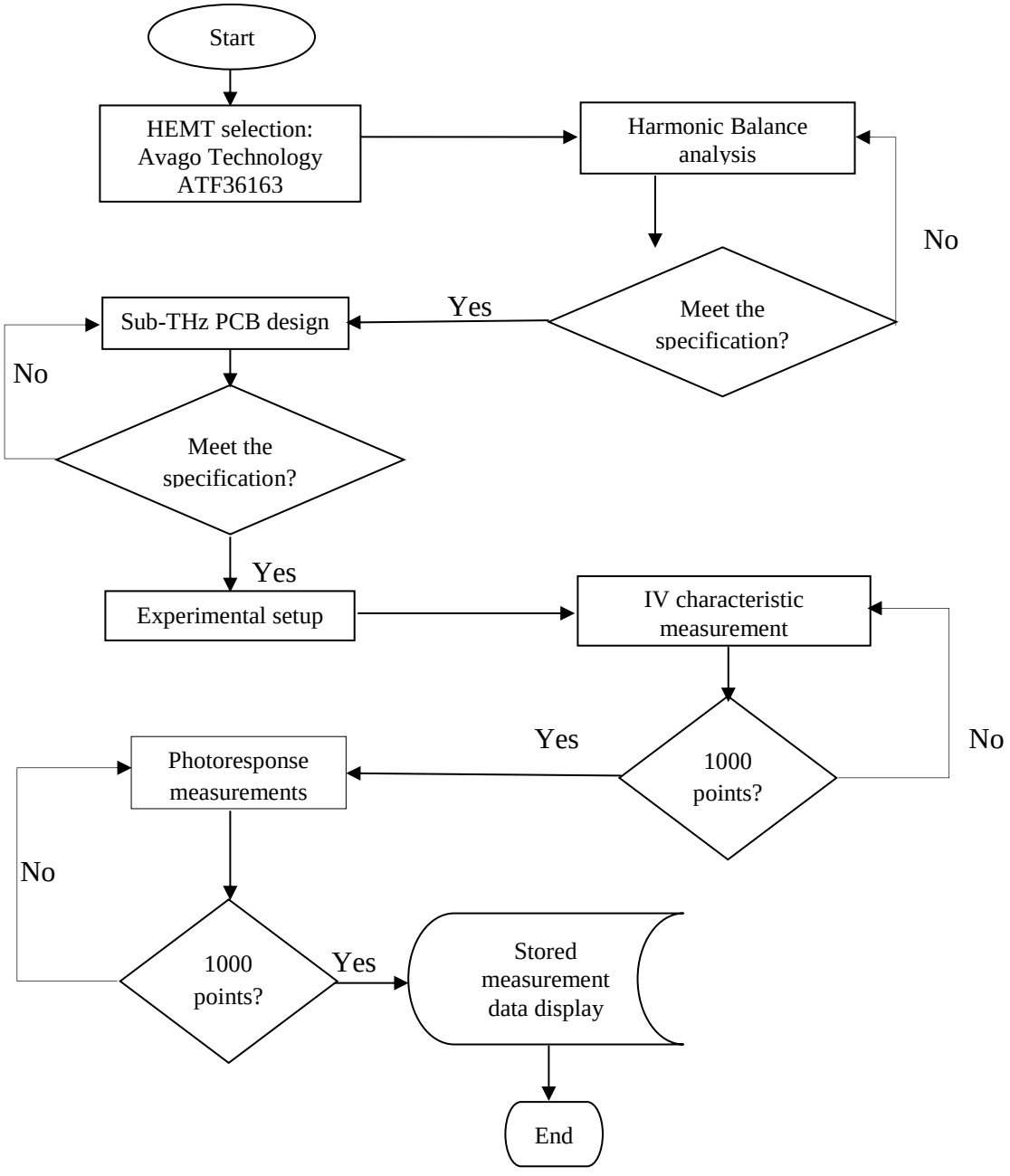

Figure 4.4: Process of designing and experimental HEMT.

Figure 4.4 shows flowchart format for the design methodology of a sub-THz detector based on a commercial HEMT. The first stage is choosing the appropriate device. Previous work used a HEMT manufactured by Fujitsu (FHR20X) and the data sheet of this device indicates it has a 0.15 μm gate length and 100 μm gate width [71]. Since there are already reports that this device works as sub-THz detector, this would be the obvious choice. However, it was not possible to get samples from the manufacturer and the UK supplier as they would only sell large quantities of the device and so, cheaper alternatives were investigated. Since the mechanism proposed by Shur et al [35] was universal and only required a 2 dimensional electron gas and the coupling mechanism was likely to be via the bond pad, it was very likely that other commercial HEMTs would also exhibit the effect.

Consequently, it was decided to use a HEMT that was freely available and relatively cheap. The chosen device (Avago Technologies ATF 36163 HEMT) was cheap and was a standard stock item of the local electronics distributor. The device is slightly larger than the Fujitsu device previously used and so the responsivity and frequency dependence is expected to be slightly different from the previous work. According to the ATF 36163 datasheet, the gate length and width are nominally 0.2 μm and 200 μm gate respectively. In addition, the datasheet states that the typical value for F_{max} is 100 GHz whilst F_T at 40 GHz [81].

4.1.2 Sub-THz Detector configuration

Before proceeding, it is worth recapping the mode of operation of the device when it is being used as a sub-THz detector. The device is biased at a constant drain current and the THz signal is applied to the gate. The non-linear processes within the device will cause the DC current to change slightly. However, most detection techniques whether it is lock in detectors used in previously published work or the high impedance amplifiers used in this work detect voltage changes.

Consequently, the change in DC bias current is converted to a voltage using a sampling resistor. This is usually a combination of the drain resistance in the circuit and the internal impedance of the source. If a voltage source is used to bias the drain, the internal resistance of the source will be very small and the sensing resistance is effective the value of the drain resistor. On the other-hand, if a constant current source is used, then internal resistance of the source is significantly higher than the drain resistance of the circuit and so the sensing resistance is approximately the internal resistance of the source. In previous work, a voltage source was used to bias the device and so simulations were performed using a voltage source but in our own configuration, we used a constant current source.

4.1.3 Harmonic Balance Analysis

As stated the previous section, the plasma resonance effect is not included in the spice model of the device and it is important to investigate whether parametric down conversion caused by the non-linear gate-capacitance can explain the detection of sub THz radiation. Harmonic Balance analysis (HB) is an extension of AC spice analysis that allows non-linear effects to be modeled. In reality, the non-linear elements of a circuit or device will produce an infinite number of mixing products and a full simulation would require the tracking of the relative magnitudes and phases of each of these mixing products. However, the majority of the mixing products are very small. Consequently, these products and their interaction of these products within the circuit can be neglected without having a significant impact the estimation of circuit performance [82].

The HB analysis provided by the Agilent ADS simulation suite allows single or multiple input frequencies simulation and allows the calculation of the intermodulation frequencies, harmonics and frequency conversion between the different harmonics. This analysis will produce not only the harmonics itself but each signal source can also produce harmonics or small signal sidebands. The device model used in the simulation was the spice model for ATF-36163 provided by Avago Technologies with 0.2 μm gate length and 200 μm gate width and includes all the packaging parasitic elements. The model is shown in figure 4.5.

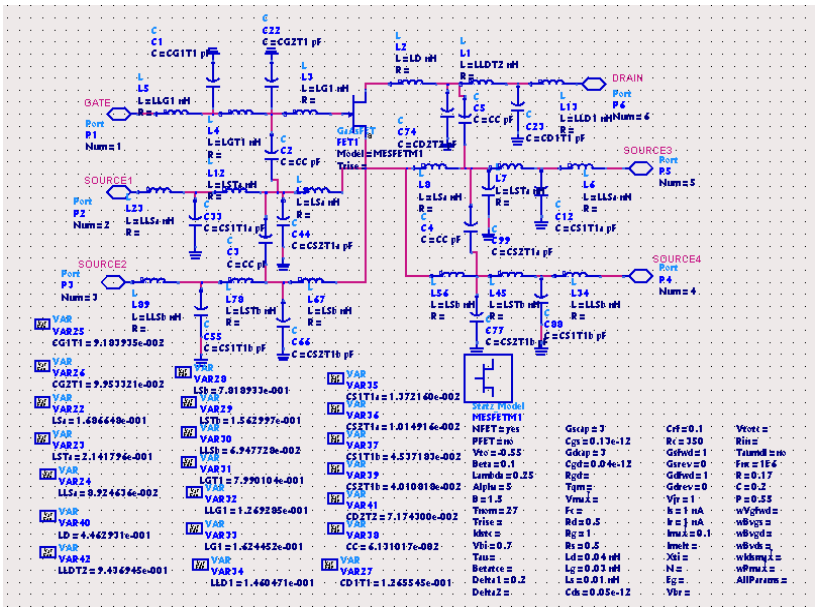

Figure 4.5: ADS model for ATF-36163

Prior to running the HB analysis, DC simulations were performed to determine the operating point of the device and to confirm that the spice parameters are consistent with the device datasheets. Figure 4.6 shows the IV characteristic measurement configuration. Figure 4.7 shows the I_D vs V_{DS} characteristic and I_D vs V_{GS} characteristic of the ATF36163 device. The important parameter from the diagram is threshold voltage (V_{TH}) which is equal to -0.6 V which, as expected, is the typical value in the datasheet. The threshold voltage for a real device is likely to be different from the typical value because of process variation.

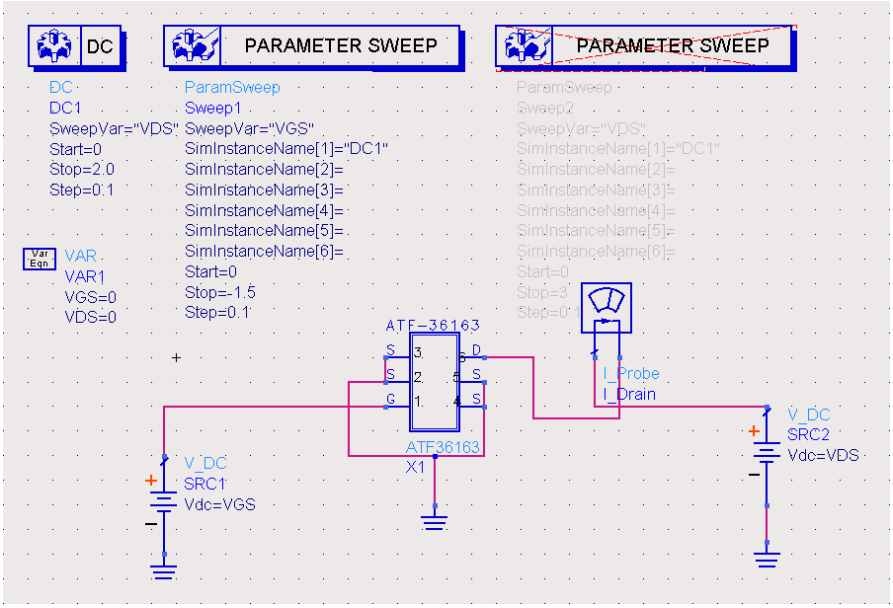

Figure 4.6: ATF36163 IV characteristic circuit

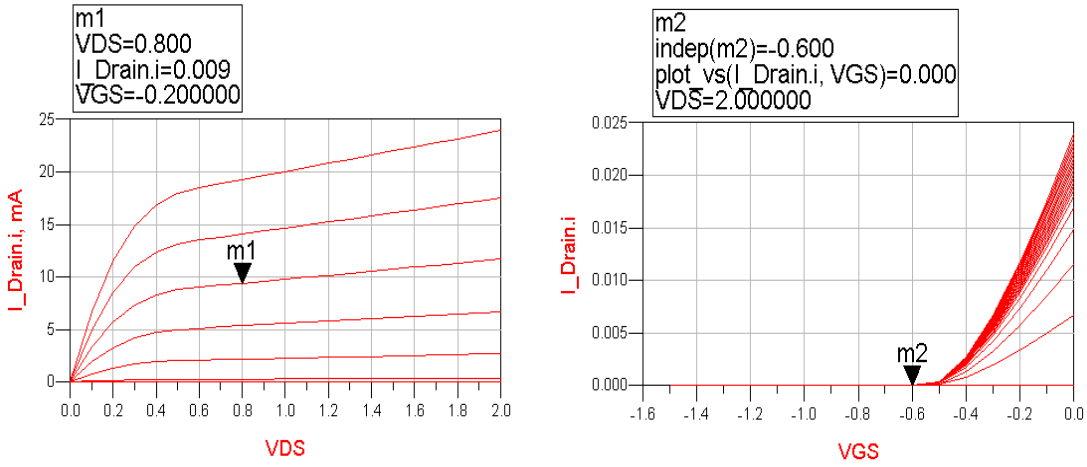

Figure 4.7: ATF36163 IV Characteristic

As stated previously, HB analysis will allow us to determine whether the detection can be explained using current models. In figure 4.8, the ADS schematic used for HB analysis is presented. Although in practice we will be using the device to detect one single sub THz signal, two frequencies close together have been used in

the simulation.

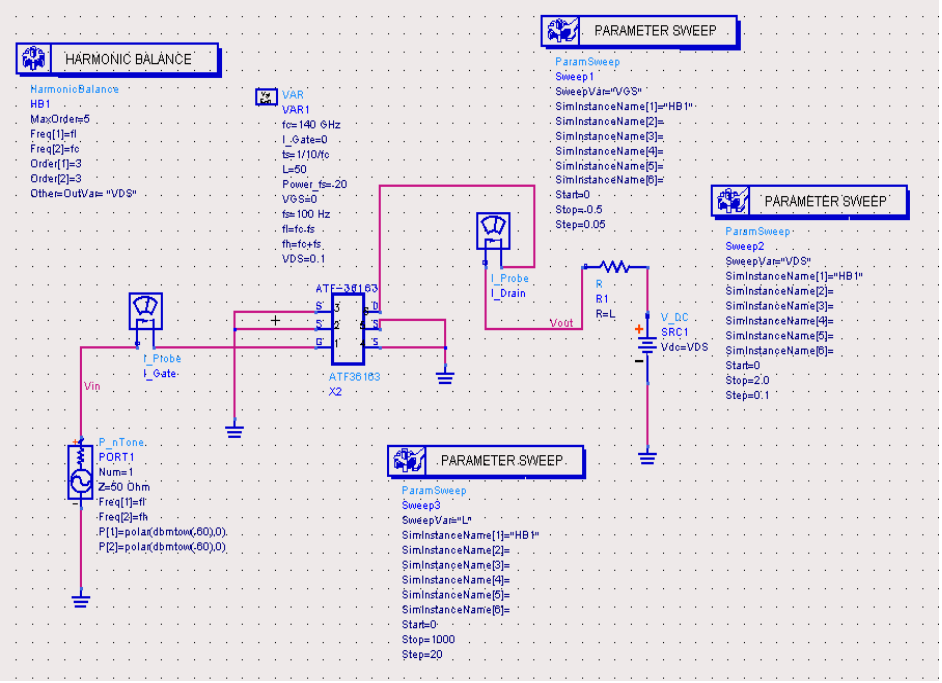

Figure 4.8: HB analysis circuit using HEMT ATF-36163

This allows the beating of the signals to produce a quasi DC value that can be easily extracted from the simulation data. If a single frequency was used, the self-mixing would result in changes to the DC value and the simulation data would be lost in the simulation noise caused by rounding errors and iteration tolerances. In the schematic, the HB component tells the ADS simulator that HB analysis is required and the values of the component are important simulation parameters. The Max Order parameter indicates the highest non-linearity used in the calculation of the mixing products. The frequency parameters informs the simulator of the input frequencies whilst the order parameters indicates which orders of the fundamental frequencies to use in the simulation. The final parameter indicates the other output nodes. The input

to the circuit is the P_ntone component. This allows multiple frequencies to be feed into the circuit using a source of output impedance 50 Ohms. The power of each of the signals was -60 dBm. As discussed above, two frequencies are used with a separation of the 200 Hz. Consequently, the frequency which represents the down-conversion of the sub-THz radiation is 200 Hz. The average frequency is 140 GHz, which was chosen because it is in the range of one of the VNA extenders. The Parameter sweep components allow the sweeping of one of the circuit parameters so that down conversion responsivity as a function of that circuit parameter can be found. The values swept were V_{GS}, V_{DS} and R_L.

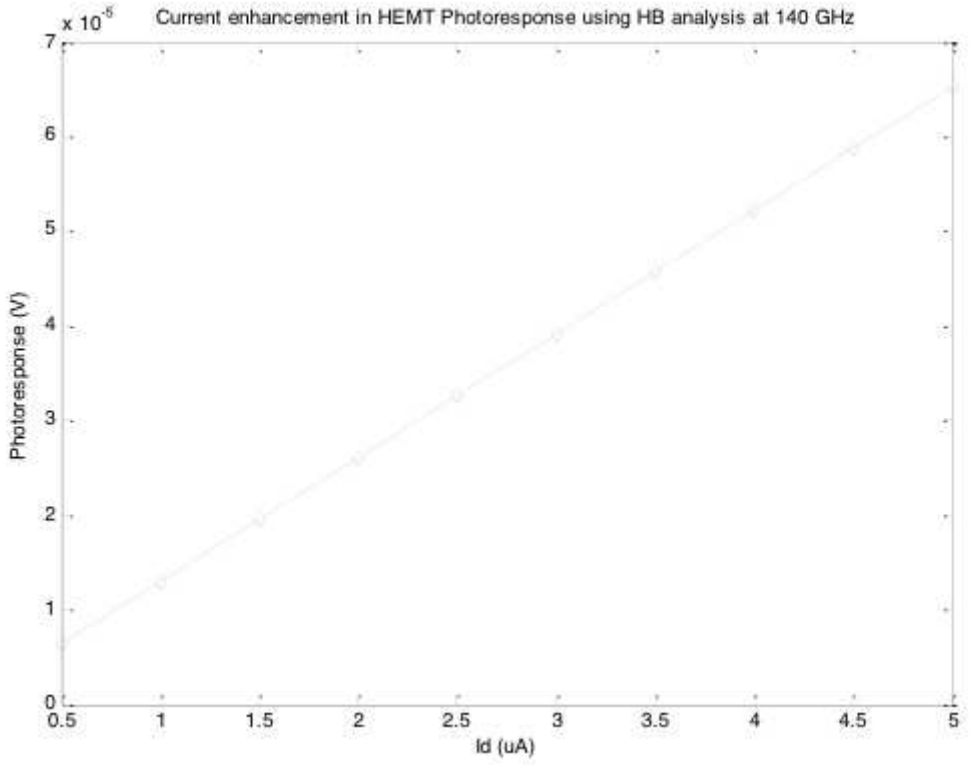

Figure 4.9: Peak photoresponse for different drain current using HB analysis.

Photoresponse is measured at the output of the device (V_{DS}) whereby the sub-THz signal will enter into the gate device while the device itself will be biased at V_{GS} near to the threshold voltage of the devices. In HB analysis, we tried to simulate the photoresponse of the devices by injecting a 140 GHz signal with 0 dBm. The outputs from the drain were measured in term of voltage. From the Figure 4.9, it can be seen that in terms of magnitude, the photoresponse was 0.6534 μV at DC term from HB analysis. The results looked promising indicating that the detection of sub-THz frequencies may be possible. The response started to increase around the threshold voltage for this device at -0.6 V. This showed that the gate voltage controls the carrier density in the channel and then it allows the resonance plasma frequency to be tuned [70].

By enhancement of the drain current, the photoresponse also increased. The simulation results predicted that by increasing the drain current, the photoresponse also increases from 0.2613 μV at 0.5 μA drain bias, up to 0.6534 μV at 5.0 μA drain current biasing. In summary, this HEMT transistor model can be used as sub-THz detector model. The drain current affects the physics behind the plasma wave by affecting plasma relaxation rate in driving the two dimensional plasma in the transistor channel towards plasma wave instability [35]. At this rate, the broadening of plasma wave resonant will decrease as drain current is increased.

4.1.4 Sub-THz Detector PCB board

A PCB board was designed as a platform to test the transistor performance as a sub-THz detector. EAGLE PCB Design 4.16r1 software is used to design the PCB board [83]. Our main objective was to design the sub-THz detector board to produce low noise as possible with transistors (HEMTs) being placed far away from all the electronic equipment.

In designing the PCB board, several layout techniques were considered. These techniques are important, as we want to design a circuit layout with optimum results. In PCB layout design, we need to use bypass and decoupling capacitors. For devices that need power source, a capacitors value of 0.1 μF is placed near to devices and of 10 μF near where the power sources enter the board. Bypass or decoupling capacitors generally serve to re-direct high frequency signals that are on the power rail that would otherwise enter into the sensitive analogue chip through the power pin [84]. If bypass or decoupling capacitors are not used in layout design, noise to the signal path will be created and it may cause oscillations. We used high speed, low ESR decoupling capacitors (X7R or BX type of dielectric ceramic chip) on each power supply pin ground to reduce high frequency noise on power and ground pin.

At high speeds, the signals traces look like transmission lines whereby trace impedance becomes an important factor. Supply voltage and current trace must be wider than other traces [85].

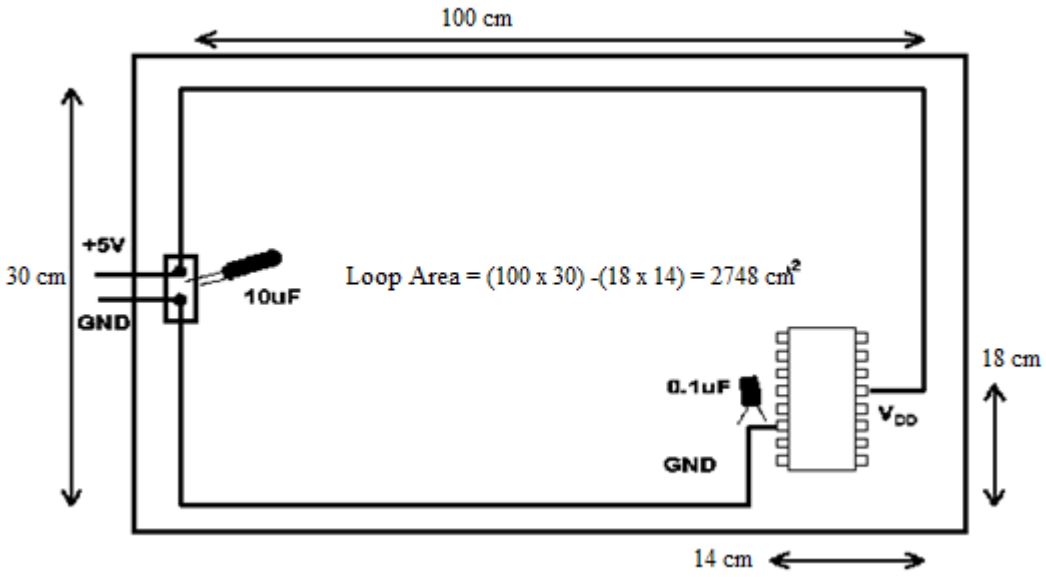

Figure 4.10: Power and ground with different route will increase EMI.

If the PCB design has a power and ground routing with a different route, it will increase electromagnetic interference (EMI) as shown in Figure 4.10. One of the techniques for reducing electromagnetic interference (EMI) is by routing the power and ground in the same place. As a result, when the power and ground are not routed together, system loops need to be designed into layout and there will be a possibility of noise to occur. This explanation will include an example of PCB designed to reduce EMI as shown in Figure 4.11.

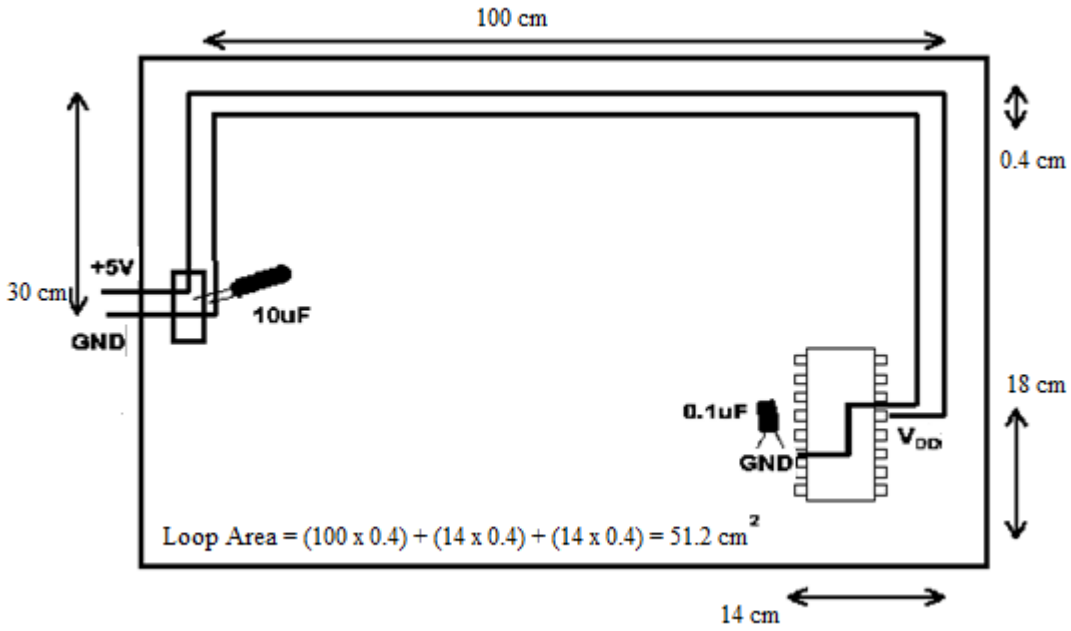

Figure 4.11: Power and ground with same route will decrease EMI.

Both PCB boards have different areas whereby the first board have loop area of 2748 cm^2 while the other one have 51.2 cm^2. The opportunity to reduce the EMI by lessening ratio of:-

$$\frac{2748}{51.2} \approx 54x$$

Placing the components in the PCB is also important. All the analogue and digital components must be separated as digital components and circuits such as digital buffer; logic gates and others are full with noise and less sensitive to it. In addition, high frequency components must be separated from the lower frequency components and kept near to the connector, as this will limit the coupling between sub-systems to a minimum.

Whenever a PCB board is designed, and two traces are put too close to each other, a parasitic capacitance will exist. Therefore, in order to solve the parasitic capacitance problem, two traces can be placed perpendicular to each other or the traces can be placed side by side but the gap between them must be bigger.

Another important thing in designing the PCB is the ground plane. A good ground is important, as it will be the foundation to a high-quality PCB design. The entire ground path has some finite impedance and so when current flow, it can cause a voltage drop. When designing a ground plane, parallel pathways can be placed to the ground and it will help to reduce inductance for the PCB board. The inductance of the conductor is inversely proportional to conductor's diameter or width but directly proportional to the length. In this case, we can decrease the inductance by reducing trace length and make it wider. The transmission reflection in the trace can also be reduced by using 45-degree turns rather than 90 degree turns.

EAGLE 4.26r1 PCB design software is a powerful tool in designing a PCB. The design started by creating a library name Sub-THz Detector. Then, the footprint such as ATF36163 HEMT transistor for each component was designed. Figure 4.12 below shown the example of the footprint for the transistor.

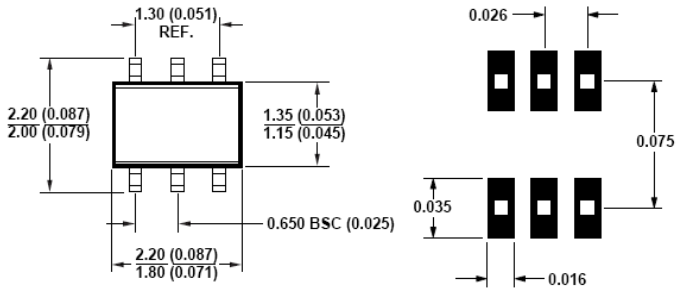

Figure 4.12: ATF36163 Package outlines with PCB pad layout [81].

After the foot print library for each component was created, these libraries were used to design the sub-THz detector board. The main concern for this sub-THz detector board was the noise created from the electronic components on the board. Therefore, all the components such as Surface Mount Technologies (SMT), variable resistor, BNC connectors and others were chosen will have a minimum noise. The sub-THz detector board was fabricated at PCB Train [86]. The schematic and layout for the sub-THz detector board are shown in Figures 4.13 and 4.14.

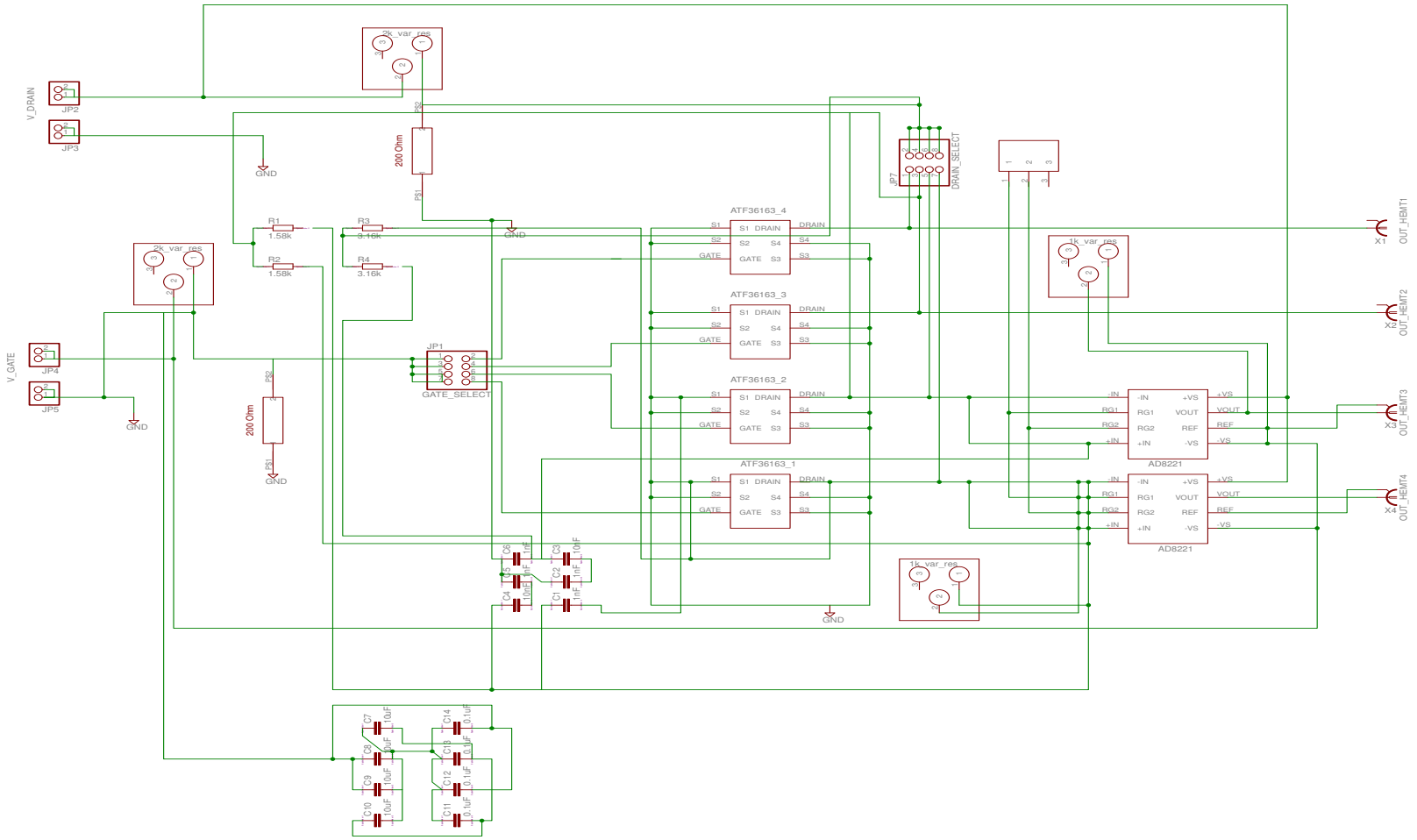

Figure 4.13: Sub-THz Detector schematic diagram.

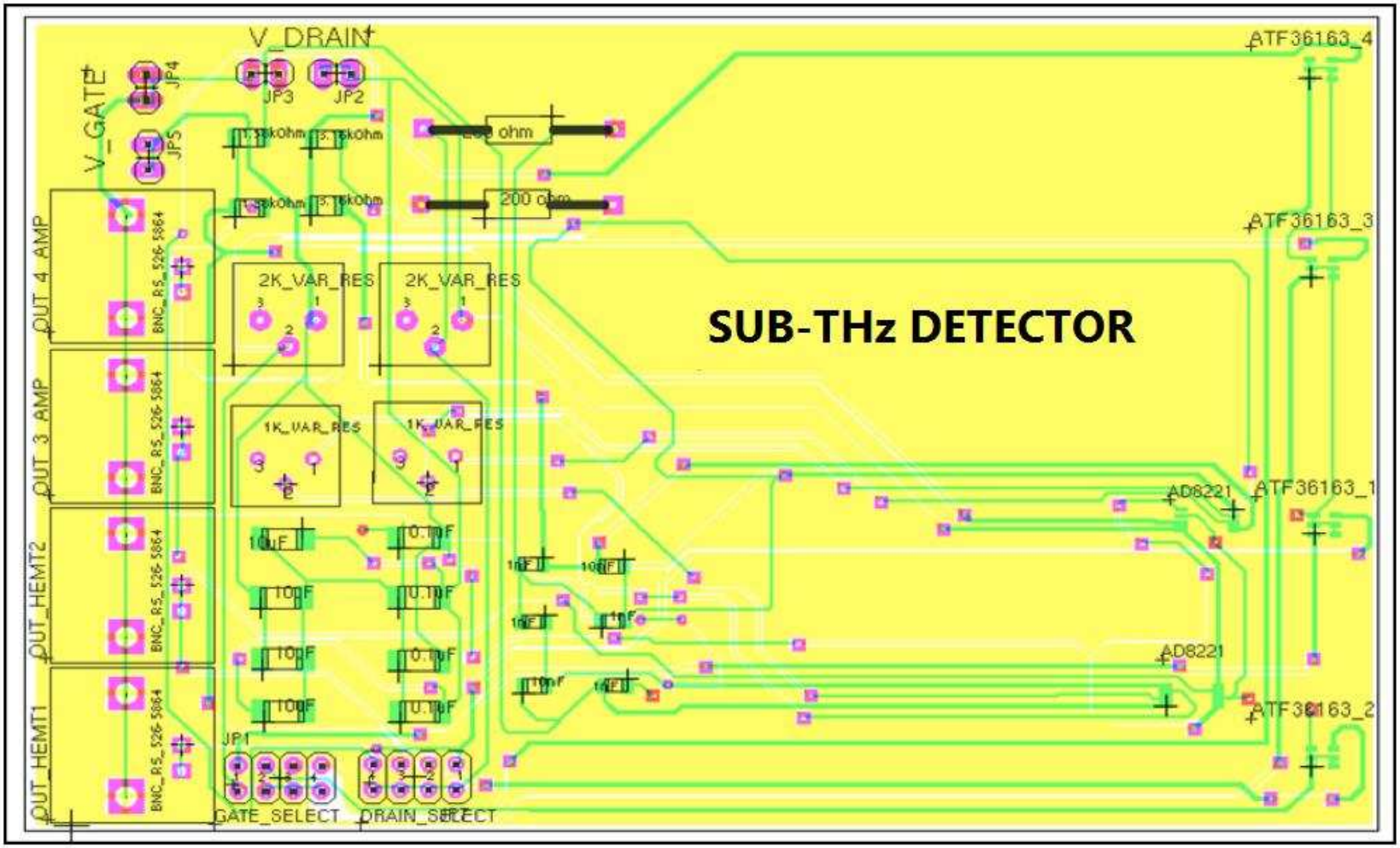

Figure 4.14: Sub-THz Detector PCB board- 123.94 mm x 80.19 mm

4.1.5 Experimental Procedure

The sub-THz detector was tested in RF Engineering room at ambient temperature. The equipment used included Broadband Vector Network Analyser up to 325 GHz, 75 um pitch RF probe test bench, Keithley 236 and 237 programmable voltage sources, digital multimeter, Olympus 20x microscope.

The SMT packaged Avago PHEMTs were commercially sourced and were soldered to a custom sub-THz detector board that allowed easy connections to the drain and gate of the device. The source of the device was connected to ground. Keithley source measurement units supplied the biased gate voltages and drain currents. The drain-source voltage (V_{DS}) was measured using a Keithley Digital multimeter. The experimental setup is shown in figure 4.15.

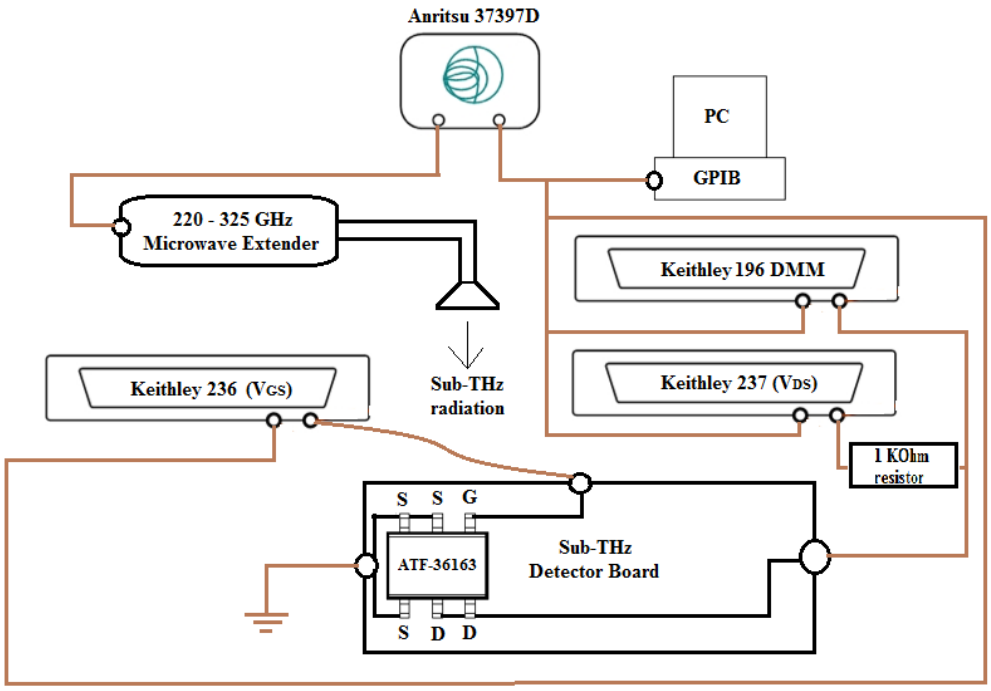

Figure 4.15: Experimental setup for Sub-THz detection

The source of radiation was an Olsen Microwave Lab (OML) vector network analyser extender (V03VNA2-T/R module) which can operate between 220 GHz and 325 GHz. The VNA extender was connected to an Anritsu Broadband Network Analyser ME7808B operating in CW mode. This allows the frequency of operation to be changed. The RF input power to the VNA extender was 13 dBm and nominal output power from VNA extender specifications was – 25 dBm. This power was not verified. Moreover, there is no recognised power standard above 100 GHz.

The power from the VNA extender was coupled into HEMT device using a length of rectangular waveguide and a horn antenna. The horn was placed directly above the HEMT but not touching the surface. There were no special antennas connected to the device. To measure the photo-response of device to the incident radiation, the value of V_{DS}, is measured when the incident radiation was on, and subtracted from the value obtained when the radiation was off. (The power of the incident radiation was turn off by removing the incident RF power to the VNA extender.) Since the photo-response is small in 0.1 V, the measurements had to be repeated 100 times and averaged.

4.1.6 IV Characteristic and Photoresponse experiment using Labview

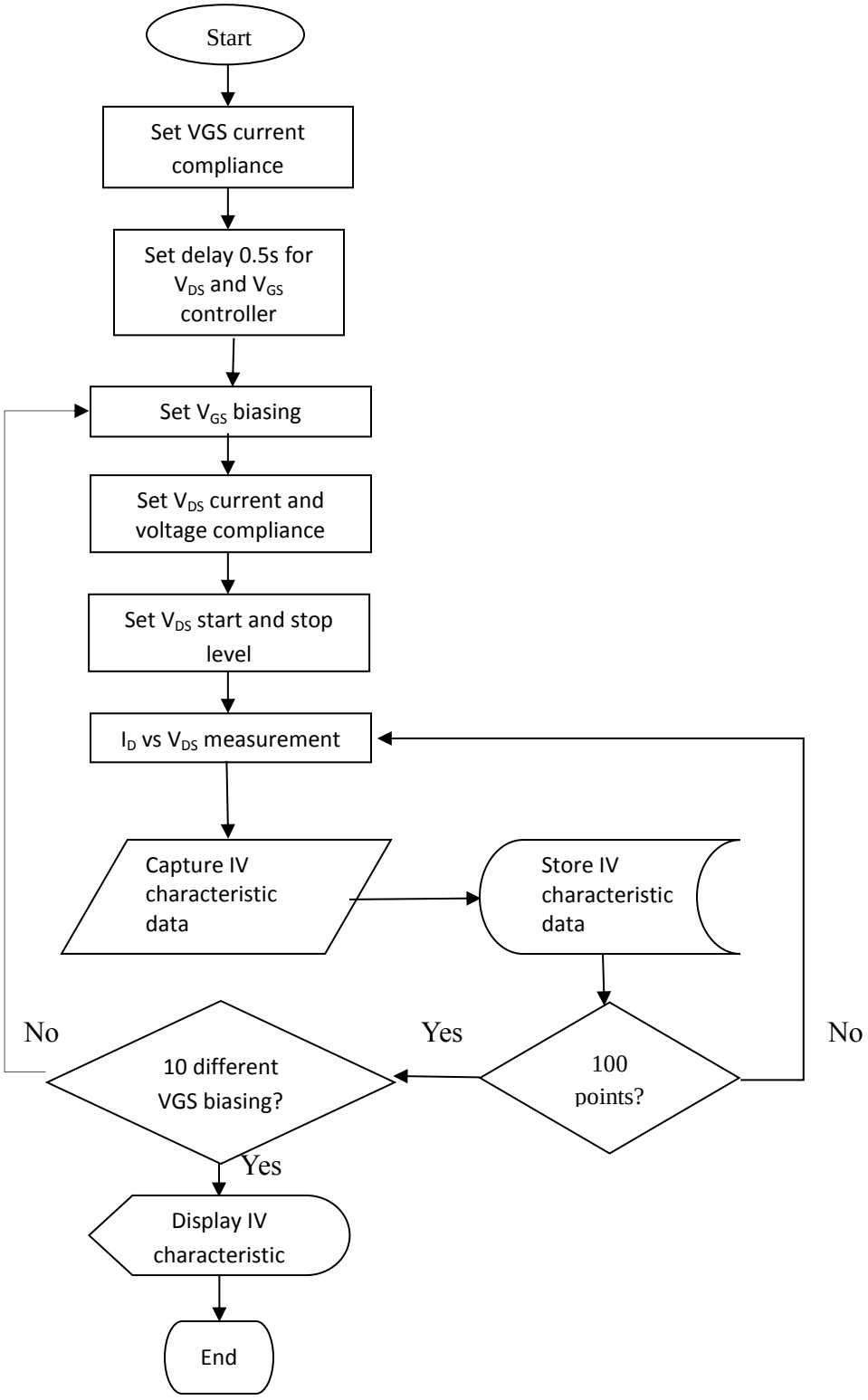

Figure 4.16: IV characteristic experiment flowchart using LabView

To measure I_D, two Keithley source measurement units (SMU) were used and controlled via a program based on Labview 8.5 [57] with NI-USB-GPIB interface device. This interface device is used to connect Labview with all instruments. It is important to ensure that the instrument is initialized with its GPIB address at GPIB bus controller. For the Keithley 236 the GPIB IEEE address was set at 16, the Keithley 237 the GPIB IEEE address was set to 15 and for Keithley 196 digital multimeter (DMM), GPIB address was 17. In addition, the Anritsu Broadband Network Analyzer for sub-THz source, the GPIB address was set at 13.

The flowchart for developing FET IV characteristic program using Labview is shown in Figure 4.16. At the beginning of the program, the VGS (Keithley SMU 236) and the V_{DS} (Keithley SMU 237) current compliance was set at a certain value to protect the devices from short-circuits and burn out. Then, a delay of around 0.5 seconds was set at V_{GS} and V_{DS}. Later on, the V_{GS} were set at 10 different biasing, while V_{DS} was set at 100 point of different biasing by setting the V_{DS} start, stop, and voltage step. After that, the program was run and I_D was measured using digital multimeter (Keithley 196 DMM). The IV characteristic data was captured and stored inside LabView memory. The process of capturing data continues until the V_{DS} biasing point reach 100 points.

4.1.7 Photoresponse Experiment using Labview

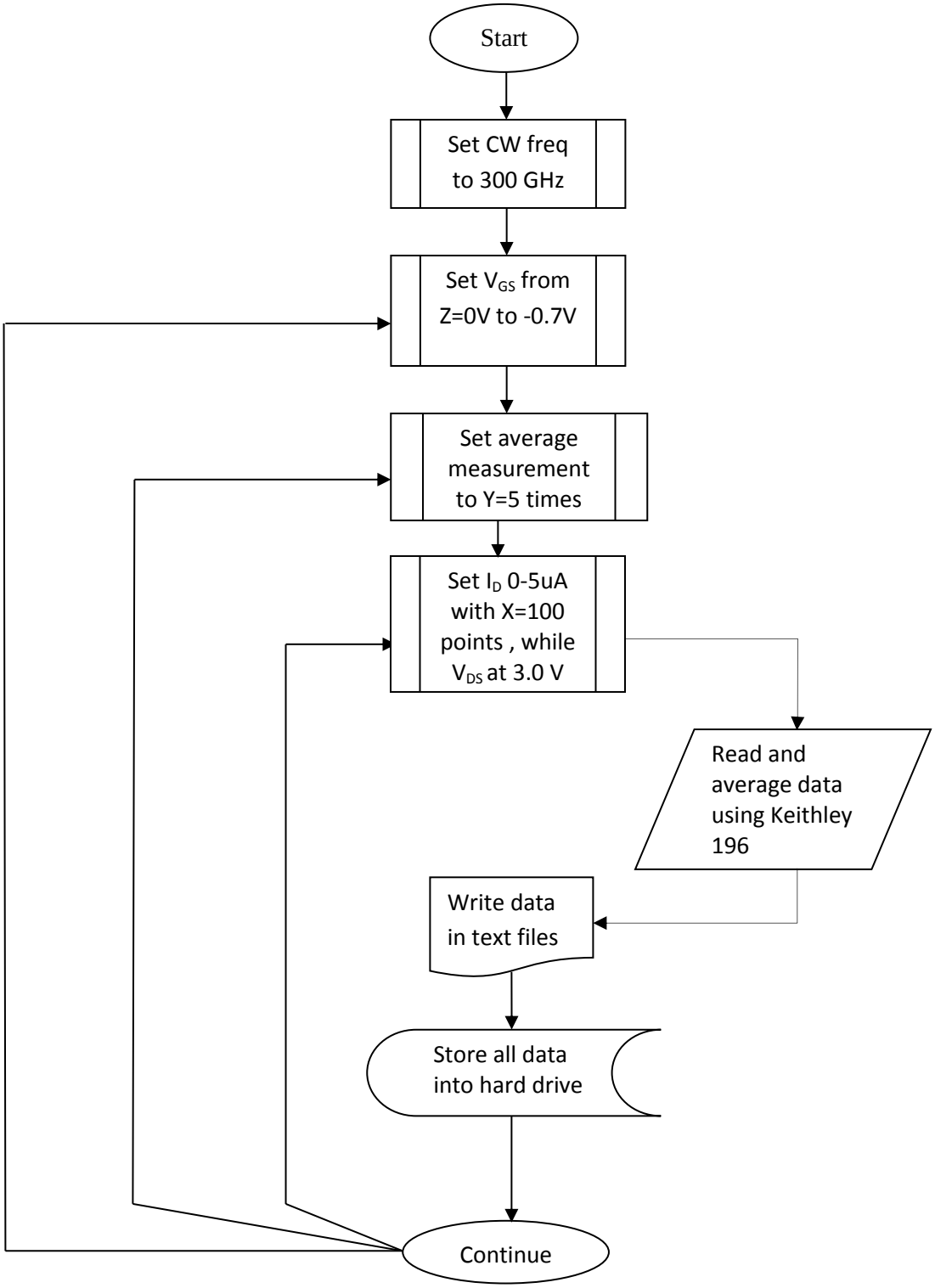

Figure 4.17: Photoresponse flow chart using Labview 1

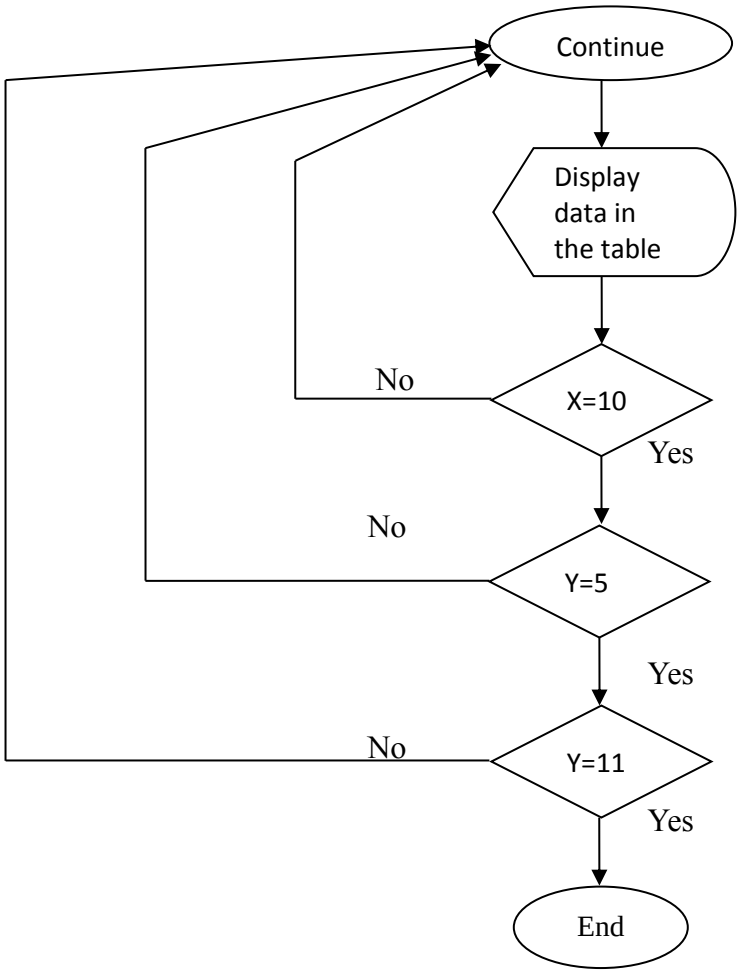

Figure 4.18: Photoresponse flow chart using Labview 2

The photoresponse can be produced in different types of experiments as shown in Figures 4.17 and 4.18. At the first stage, frequency was fixed with varying VGS and $I_{D.}$ The development of this program was based on Labview 8.5 with NI-USB-GPIB interface device. This interface device is used to connect Labview with all instruments using GPIB address. Labview initializes each instrument based on their GPIB address. In this experiment, GPIB IEEE address for Keithley 236 was 16 while Keithley 237 was 15. An analysis of the measured data will be described in the next section.

4.2 Results and discussion

4.2.1 Experimental results and discussion

4.2.1.1 FET IV Characteristic.

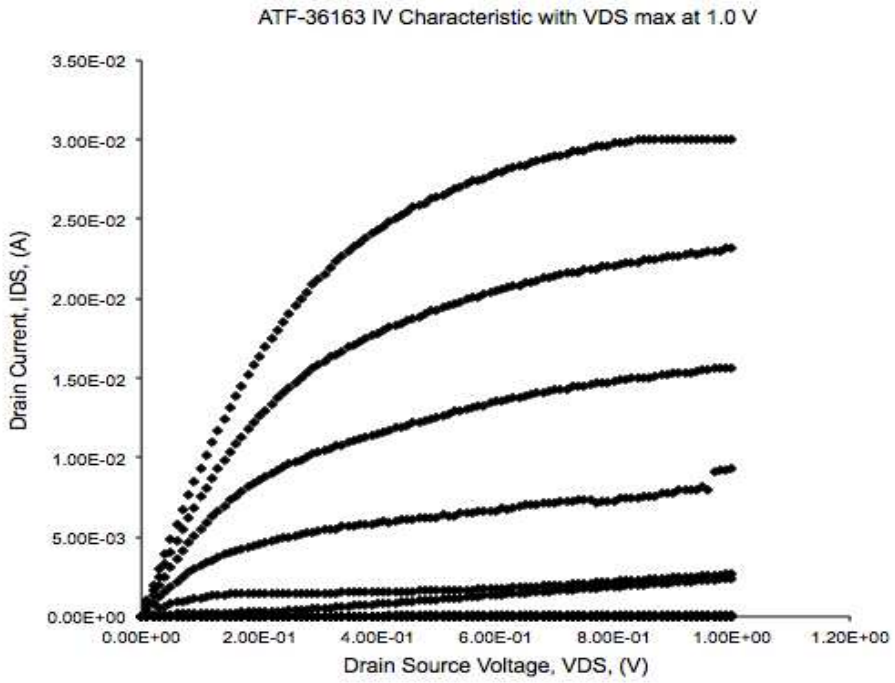

Figure 4.19: Measured ATF36163 IV characteristic.

Figure 4.19 shows the measured IV characteristic of the ATF36163. The drain current is 3 mA at V_{DS} = 1.2 V. In the next experiment, the photoresponse of the devices were measured. The process of photoresponse measurement takes quite a long time since the photoresponse data measurement was so small and sensitive. The experimental repetitions needed to be done although the calibration for measurement was previously performed before. The data repetitions of measurement were averaged so that it reduced the noise from others, and increase data accuracy.

4.2.1.2 Photoresponse: fixed frequency, vary V_{GS}, vary I_D

Figure 4.20 shows the photoresponse of a device as a function of V_{GS} for different bias currents. In all these measurements, the frequency was constant and set to 300 GHz. The photoresponse was very small until V_{GS} approached the threshold voltage of device (-0.6 V). When V_{GS} was reduced further, the photoresponse began to increase and then levelled off before sharply increasing again. At higher currents, there is also evidence that the photoresponse goes through a maximum. This method of drain current enhancement, will affect plasma relaxation rate in driving two-dimensional plasma in the transistor channel towards plasma wave instability [69].

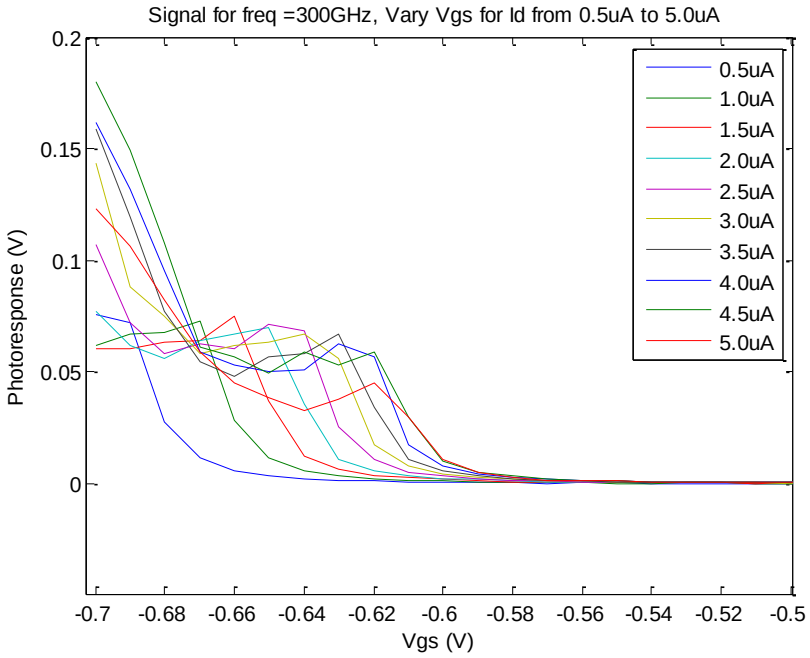

Figure 4.20: Photoresponse signal for frequency at 300 GHz as a function of gate bias at different drain current.

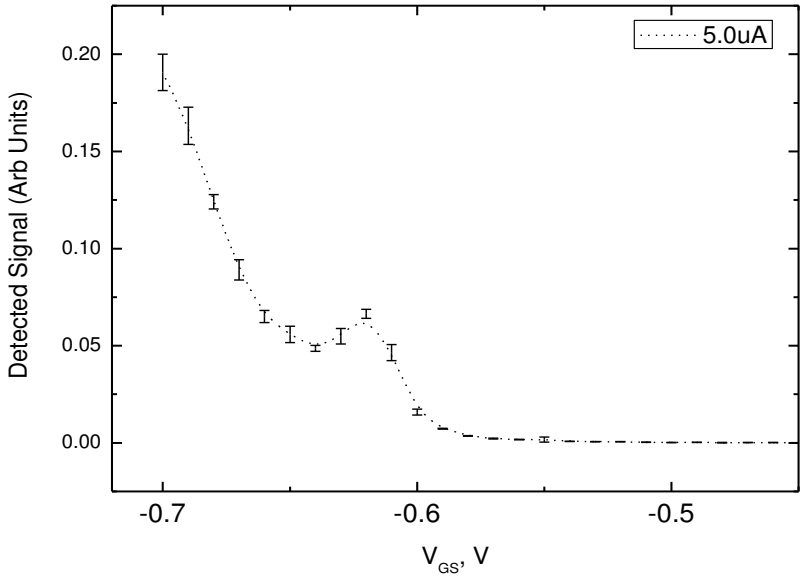

Figure 4.21: Photoresponse along with the corresponding standard deviation for a bias of 5 μA.

The variation of photoresponse is shown more clearly in Figure 4.21 whereby data obtained with a drain bias current of 5 μA is shown on its own. Also included in this diagram is an estimation of the measurement over photoresponse by taking 100 measurements and calculating standard deviation. From this diagram, it is clear that the "peak" at V_{GS} = -0.62 V consists of one data point and need to bear this in mind when drawing conclusions. However, the difference between this point and its neighbours is larger than standard deviation of the measurements. In addition, this behaviour is seen in other curves presented in Figure 4.20.

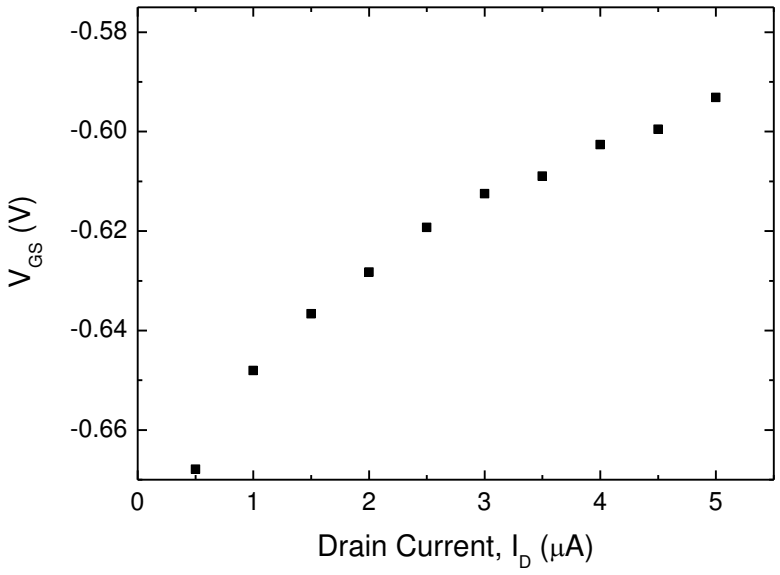

Figure 4.22: The values of V_{GS} at which the photo-response is 0.01 V as a function of the DC drain bias current.

Another observation from Figure 4.21 is the voltage, at which photoresponse initially increases depends on drain bias current. In order to investigate this phenomenon, the voltage at which signal was detected is equal to 0.01 V as shown in Figure 4.22. In all cases, the point at which this occurs is between two measured values. So, linear interpolation has been used to estimate the value. The figure shows that the responsivity does increase with bias current but the rate of increase slows down with drain current [87].

4.2.1.3 Photoresponse: fixed I_D, vary V_{GS}, vary frequency

The effect on the photo-response for frequencies from 220-320 GHz is shown in Figure 4.23. In all these measurements, the drain current was kept at 5 μA. Since

the power emitted by VNA extender was not measured, only trends in data are valid. In general, the shape of photo-response $-V_{GS}$ characteristic is approximately the same for all frequencies. However, on closer inspection, the frequency dependence of the responsivity at "-0.62 V peak" is different to the case when V_{GS}=-0.7.

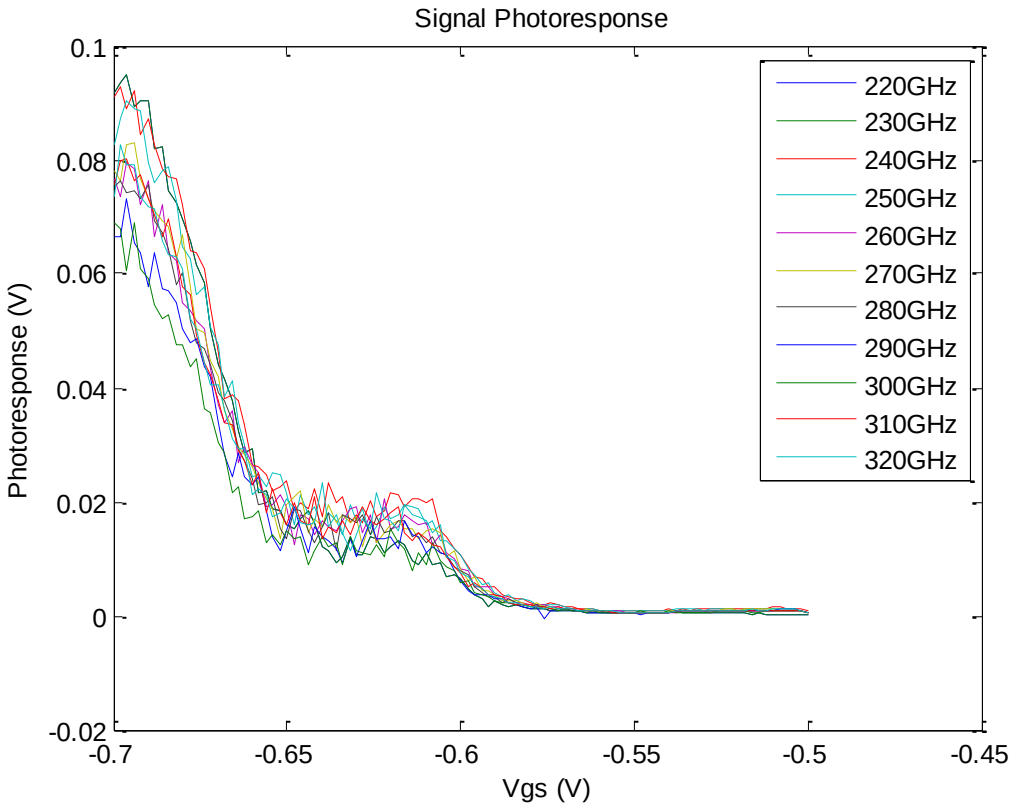

Figure 4.23: Photoresponse in different frequency in biasing V_{GS} [88].

Previous results on the use of THz detectors show just a single broad peak in responsivity with the maximum occurring approximately at the threshold voltage of device. In our results, there is a superposition of a possible small peak with a general increase in responsivity as V_{GS} is decreased below the threshold.

4.2.1.4 Photoresponse: varying VNA input power

In the next experiment, photoresponse was run with different RF power input from 6 dBm, 8 dBm and 10 dBm. The experiment setup is still the same with V_{GS} at -0.65 V (threshold voltage -0.60 V for HEMT ATF36163), and varying the I_{DS} from 2 µA to 10 µA and also fixed frequency at 300 GHz. Each point was averaged 100 times by Keithley 196 DMM and 100 times in LabView program to get the average data. The result is shown in Figure 4.24.

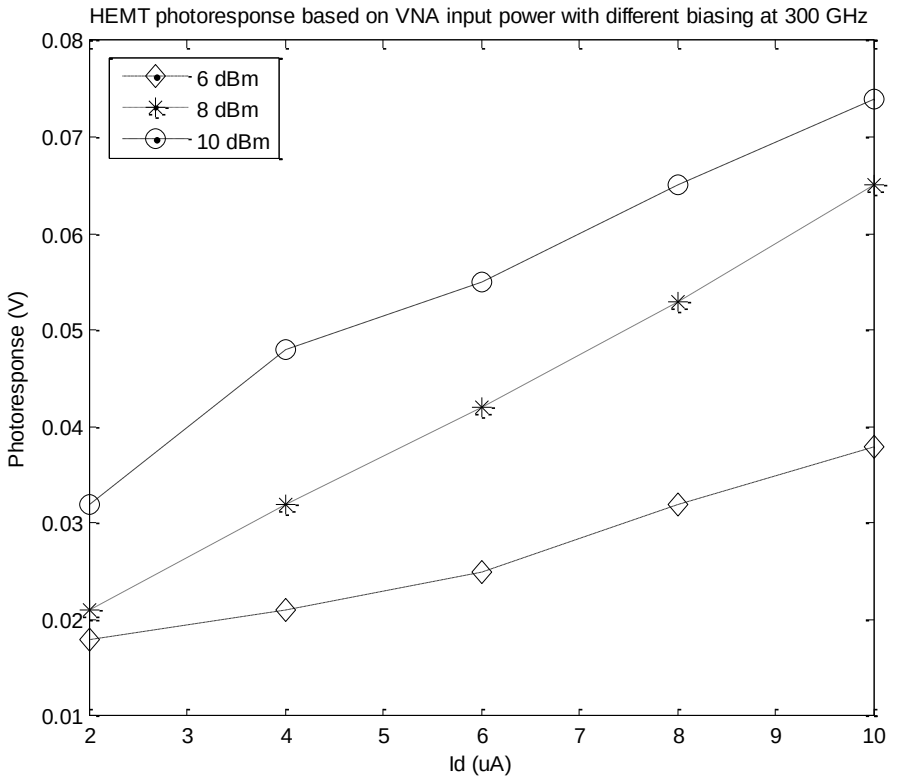

Figure 4.24: Peak of photoresponse at different VNA input power

These results were purely original, as no other similar researchers have done this experiment before. In summary, with different RF power input, bias at $V_G=V_{TH}$, and varying I_D, the results show that when RF power input increase, the photoresponse will also increase. Several explanations are put forward regarding these results.

Previously, measured peak width was approximately 0.2 V [71]. This happens because the result presented is just one side of an unobserved peak. However, V_{GS} could not be reduced any further to test this criterion. As V_{GS} was reduced below pinch off, the resistance of the channel between source and drain rapidly increased. Since the drain is driven by a constant current source, the drain voltage increased and reached 3V the maximum permissible V_{DS} for this device.

The measured response of HEMT detector depends critically on the orientation of polarisation with radiation with respect to the gate finger [89]. However none of the published photo-response-V_{GS} characteristic looks like the measured characteristic of this work. In terms of the measurement frequency, our experimental results are different from previous work [90]. From comparison with literature, the response does depend on frequency. It is unclear whether this difference can be attributed to the measurement frequency or different devices and orientations used. The results presented in Figure 4.24 provide some evidence to support this hypothesis because the actual shape of the response with V_{GS} does depend slightly in frequency. However, the results measured at 220 GHz still show a peak while on previous research, at 200 GHz, nothing was observed. At cryogenic temperatures (10K), small peaks have been observed in the response as a function of V_{GS} but these disappeared

as the temperature increased. As far as this research was concerned, none of the study was done on detecting sub-THz signals by varying the RF power input. In this experiment, there is strong evidence that by increasing the RF power input, the photoresponse will also keep increasing. This proves that the HEMT is a sensitive sub-THz detector since it can generate a photoresponse at different input powers.

4.3 Conclusion

In summary, we have demonstrated photoresponse to CW sub-THz radiation of HEMT with 0.2 µm gate length and 200 µm width caused by plasma wave detection. There are some evidence that photoresponse was affected by increasing drain current and varying the V_{GS}. In addition, photoresponse also depends on frequency. Furthermore, the HEMT also gives an indication of response by varying the input power. The results also indicate that a HEMT can work as a sub-THz detector at different input powers. In general, the shapes of our response are different to previous research and several explanations have been put forward to discuss on these differences. While the HEMT gives a hope on detecting sub-THz radiation, further work was done on developing MOSFETs CMOS process technology and this will be discussed in the next chapter.

Chapter 5

Metal Oxide Semiconductor Field Effect Transistors (MOSFETs) as Sub-THz Detectors

5.0 Introduction

Recently, sub-THz and THz radiation detection by Metal-Oxide-Semiconductor Field Effect Transistor (MOSFET) manufactured in a conventional CMOS process has been reported [74]. Both P channel and N channel MOSFETs were used. Based on the prediction by F. Teppe et al. [76], sub-THz and THz radiation can be detected by using plasma waves in 2D electron gas created at the oxide semiconductor interface in a MOSFET. The actual mechanism is similar to that which has been reported using HEMTS as explained in chapter 4.

Earlier, non-resonant plasma wave detection of sub-terahertz and terahertz was discovered in HEMT [43] and Silicon FET [74]. Later on in 2005, it was reported that Silicon-On-Insulater Metal Oxide Semiconductor Field Effect Transistor (SOI MOSFET) was used as THz detector at different temperature from 8K -350K [91]. All these devices were tuned to the sub-THz frequency from 30 - 300 GHz by varying the gate bias.

5.1 Design methodology

The operation of THz detector using FETs was previously discussed in chapter 4. To investigate the effect further, several MOSFETs with different lengths and

widths in two different CMOS process, AMS C35 and UMC18 CMOS technology were manufactured. All design was done using Virtuso Cadence software [92]. The MOSFET design for this work is different from the previous research work since the gate and drains were connected directly to the RF pads which allows electrical (both DC and RF) connections by using RF probes with 75 µm pitch. The maximum frequency of operation for the Picoprobe GGB Industries RF probe is 0.22 THz [93]. The MOSFET layout in the CMOS C35 process is shown in Figure 5.1 and 5.2. All the MOSFETs have the same gate length (Lg = 0.35 µm) with seven (7) different gate width which are; 5 µm, 10 µm, 15 µm, 20 µm, 25 µm, 30 µm and 35 µm.

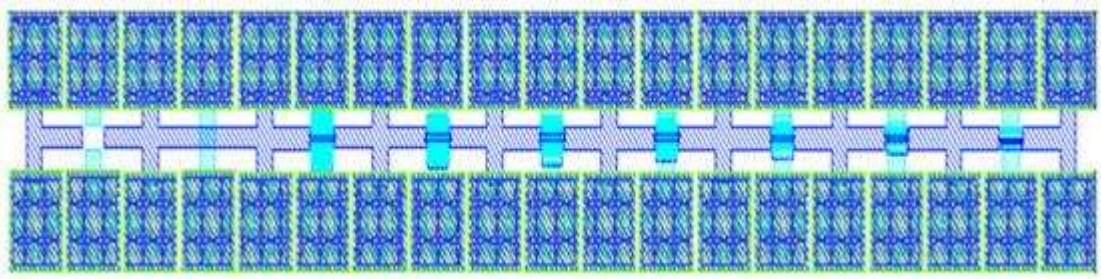

Figure 5.1: MOSFETs layout in Cadence using AMS C35 CMOS technology.

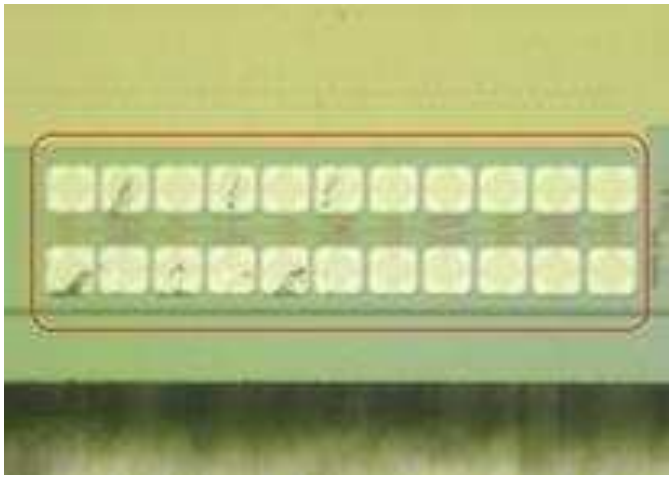

Figure 5.2: MOSFET with 7 different widths length (gate length, Lg = 0.35 µm).

Besides MOSFETs in AMS C35 CMOS technology [94], several MOSFETs with different gate length were manufactured in the UMC18 CMOS technology [95]. By using this type of technology, six (6) different MOSFETs are designed with 6 different gate lengths, which are; 180 nm, 250 nm, 350 nm, 500 nm, 650 nm and also 800 nm. The widths of the transistors are fixed at 20 μm and Figure 5.3 shows the layout for these MOSFETs.

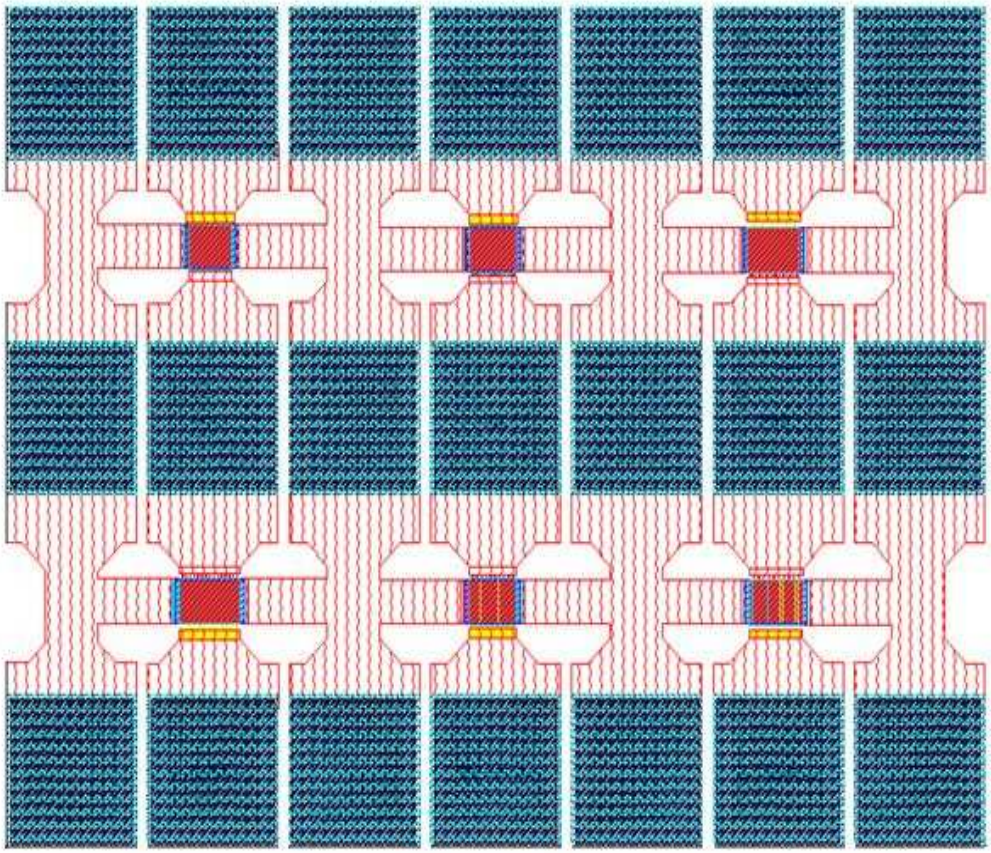

Figure 5.3: Six (6) different gate length for MOSFET in UMC18 CMOS technology.

5.2 Experimental Procedure

5.2.1 Experimental setup

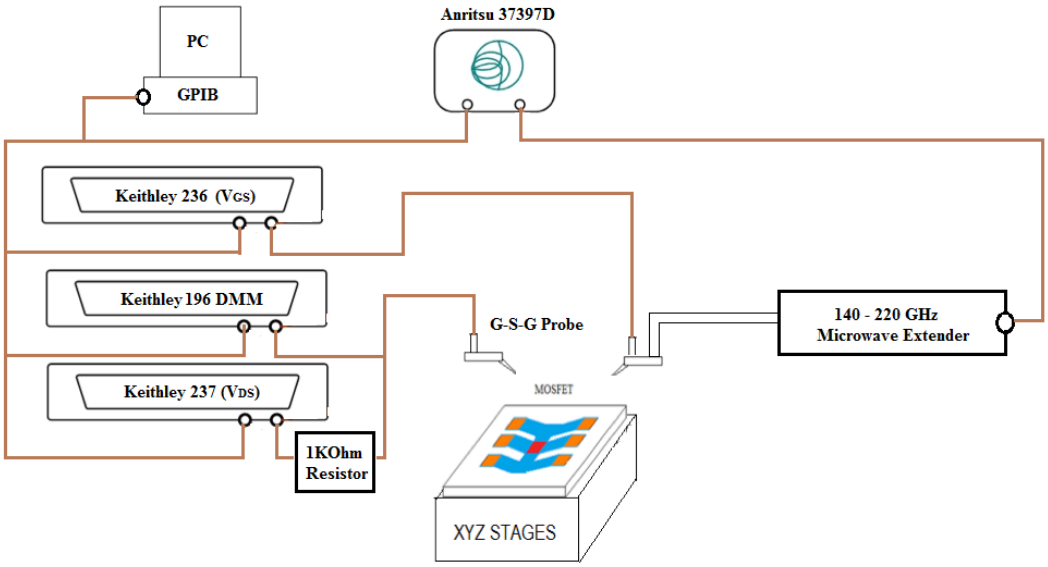

Figure 5.4: Experimental setup for Sub-THz detection using MOSFETs.

The fabricated MOSFETs were sent for fabrication and have been tested at ambient room temperature. The equipment used was Anritsu Broadband Vector Network Analyzer up to 325 GHz, 75 µm pitch RF probe test bench, Keithley 236 and 237 programmable voltage source, digital multimeter and an Olympus 20x microsope.

From Figure 5.4, the MOSFETSs were placed on to the XYZ Probe station, so that the 75 µm pitch RF probe could be easily placed at the appropriate pads which allowed connections to the drain, gate and source of the device. Note that the devices are configured in common source configuration so the source is connected to ground. The biasing gate voltages and drain currents are supplied by Keithley Source

Measurement Units model, which are numbered at 236 and 237 respectively. The drain-source voltage (V_{DS}) was measured using a Keithley Digital multimeter 238.

An Olsen Microwave Lab (OML) vector network analyser extender (V03VNA2-T/R module) which operates between 140 GHz up to 220 GHz produced the sub-THz radiation. The VNA extender was connected to an Anritsu Broadband Network Analyzer ME7808B which operated in CW mode. This allowed the frequency of operation to be changed. The RF input power to the VNA extender was -13 dBm with the output power from the VNA extender specified to be -25dBm. The power from the VNA extender was coupled into the MOSFETs device using a length of rectangular waveguide and connected to RF probe as shown in Figure 5.5. The probe/pad connection was made by placing the probe directly on to the top metal layer of RF pad and this marked a good connection whereby the sub-THz radiation directly couples into gate of device and the photoresponse could be directly measured at the drain.

When the incident radiation was on, the photoresponse was taken by measuring the V_{DS}. The photoresponse was obtained by subtracting this measurement from that when the radiation was off. The power of the incident radiation was turned off by removing the incident RF power to the VNA extender. Since the photo-response was small, the measurements were repeated 100 times and the average taken. With this procedure, the results of photoresponse could be obtained more accurately since it would reduce the noise from the photoresponse experiments.

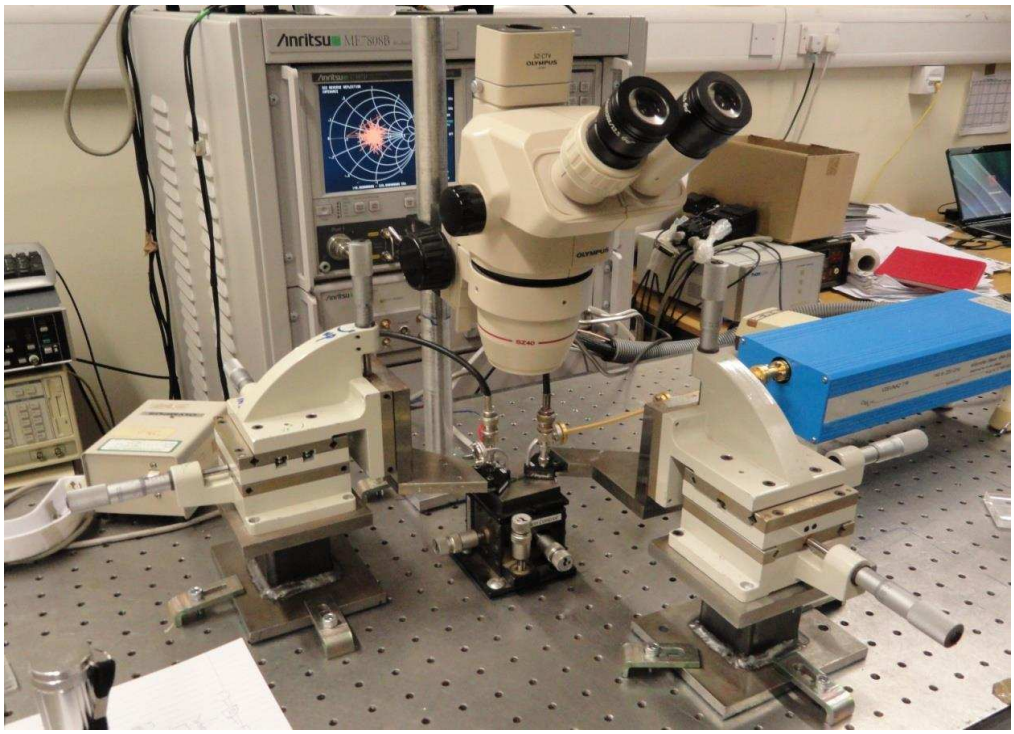

Figure 5.5: Sub-THz detection test bench.

5.2.1.1 FET IV Characteristic program using Labview

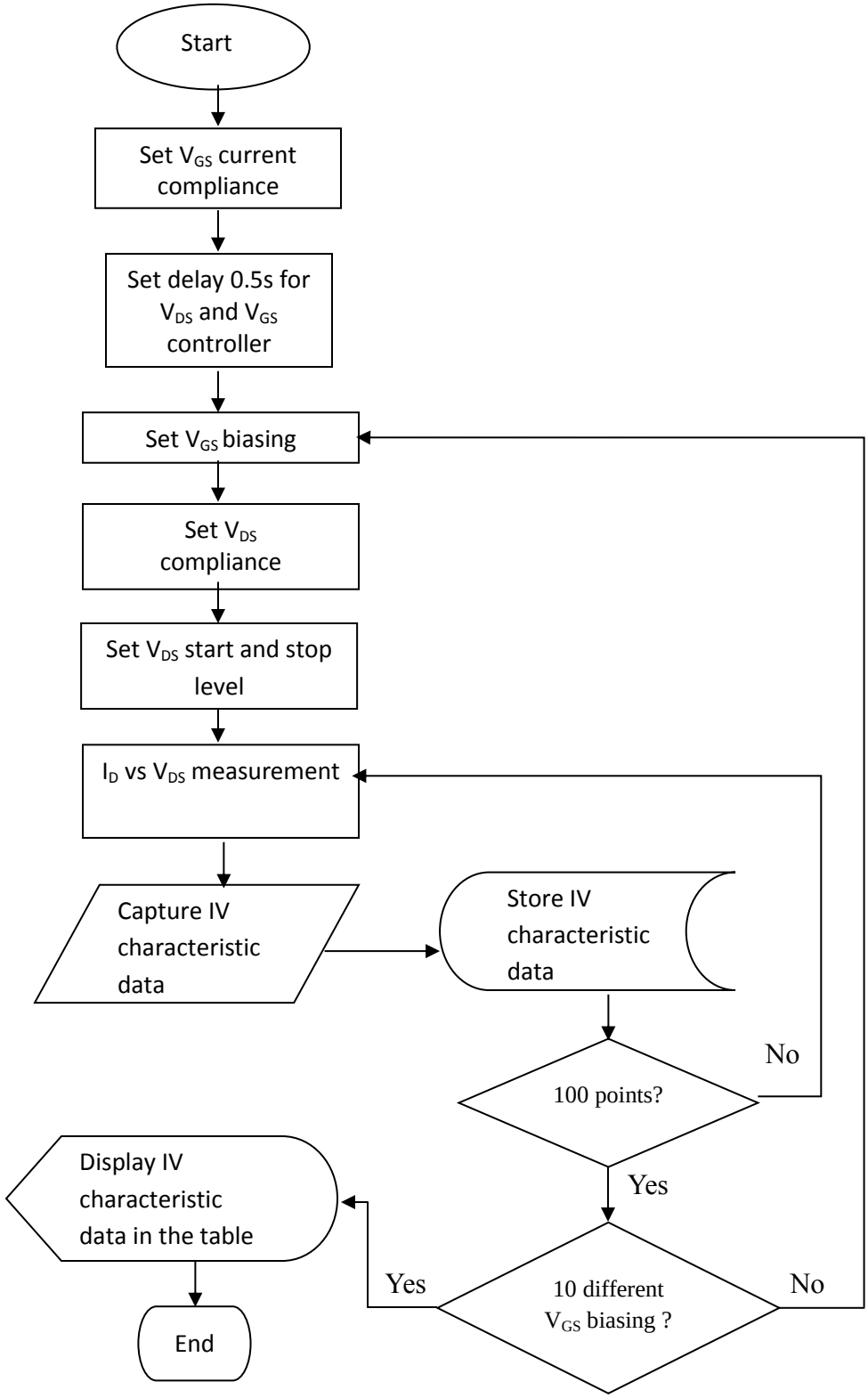

Figure 5.6: IV Characteristic experiment flowchart using LabView.

To measure I_D, two Keithley source of measurement unit (SMU) were used and controlled via a program based on Labview 8.5 [57] with NI-USB-GPIB interface device. This interface device is used to connect Labview to all of the instruments. To uniquely address an instrument, the instrument needs to initialize with its GPIB address at GPIB bus controller. Each of the equipment were initialized with the GPIB addresses such as Keithley 236 the GPIB IEEE address was set to be 16, Keithley 237 was set to 15, Keithley 196 digital multimeter (DMM) was set to 17 and the Anritsu Broadband Network Analyzer as the sub-THz source, was set to be 13.

The flowchart for developing FET IV characteristic program using Labview is shown in Figure 5.6. In the beginning of the program, the V_{GS} (Keithley SMU 236) and the V_{DS} (Keithley SMU 237) current compliance was set at 3 V and 8 mA as to protect the devices from short-circuits and burn out. Then, a delay of around 0.5 seconds was set at V_{GS} and V_{DS}. Later on, V_{GS} was set at 10 different biasing, while the V_{DS} was set at 100 points of different biasing by setting the V_{DS} start, stop, and voltage step.

The drain current I_D was measured using digital multimeter (Keithley 196 DMM) when the programme was executed. The IV characteristic data was captured and stored inside LabView memory.

5.1.1.2 Photoresponse program using Labview

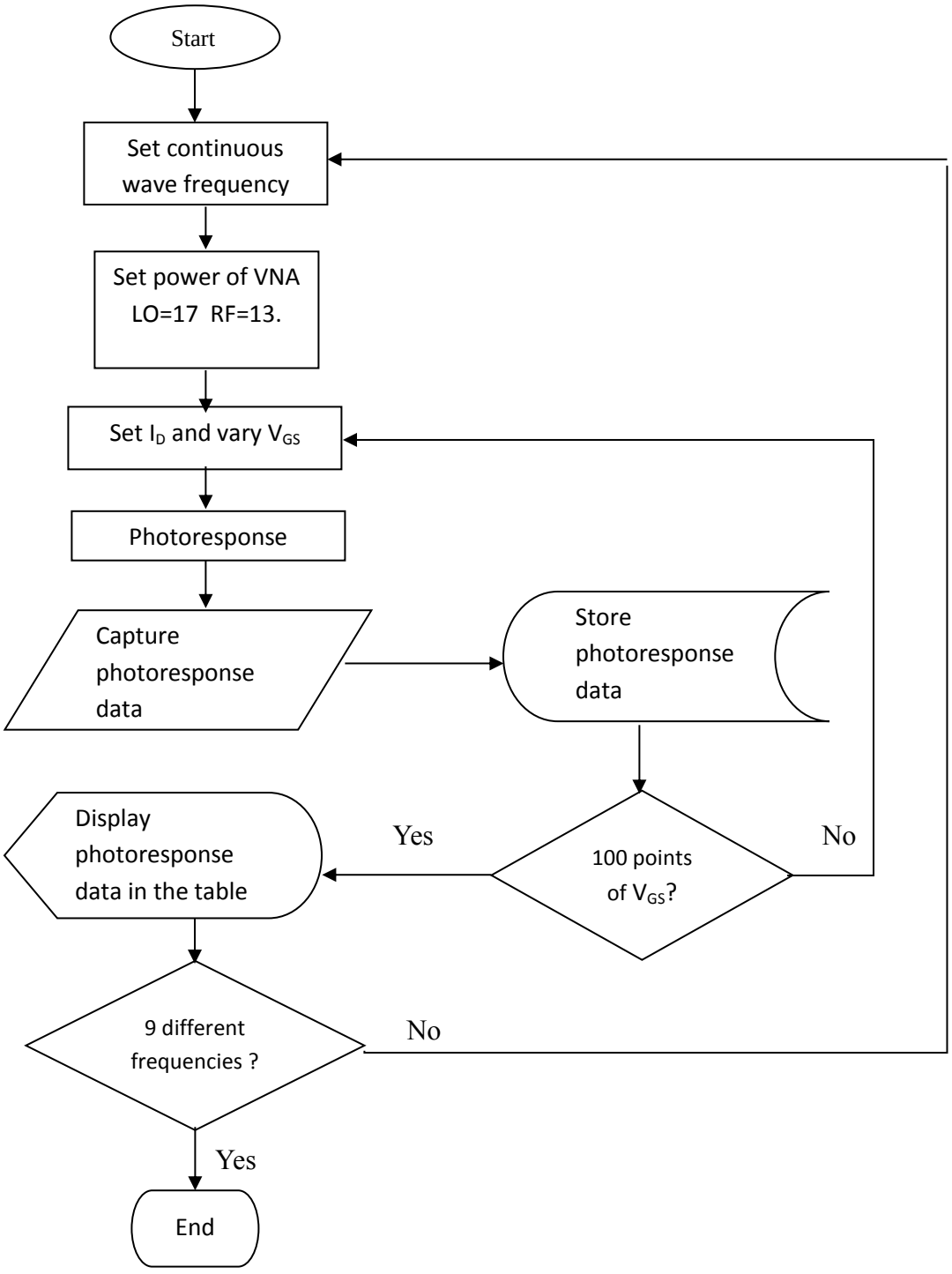

Figure 5.7: Photoresponse experiment flowchart using LabView.

Figure 5.7 shows the flowchart for MOSFET photoresponse experiment using LabView. The setting of GPIB address is the same as before. At the beginning of experiment, the frequency of Anritsu Broadband Network Analyzer as sub-THz sources was set to be as continuous wave. The local oscillator and RF power were set at 17 dBm and 13 dBm. Then, the LabView was programmed in order to measure photoresponse by setting I_D while varying V_{GS} and frequencies. The potoresponse data were captured after it has been measured by controlled digital multimeter (Keithley 196 DMM) and stored inside the LabView memory.

The measurements were taken for nine different frequencies ranging from 220 GHz up to 325 GHz and the process of capturing the photoresponse was continued until frequency reached 325 GHz. Variation of experiments was designed based on the flowchart such as; (1) fixed the frequency, vary V_{GS} and I_D (2) fixed I_D and frequency, vary V_{GS} and input power (3) fixed input power and I_D, vary V_{GS} and frequency. In section 5.3 the results and discussions are shown from these experiments.

5.3 Results and discussion

5.3.1 MOSFET IV Characteristic

Figures 5.8 to 5.13 show the simulated and experimental results for I_D-V_{DS} characteristic results for 3 different MOSFET fabricated using both AMS C35 and UMC18 CMOS technology. In the simulations, for MOSFET AMS C35 CMOS technology, with Lg = 0.35 μm and Wg = 5.0 μm, the threshold voltage was 0.21 V while maximum I_D was 1.4 mA at V_{DS} = 2.0 V. In UMC18 CMOS technology, two different types of MOSFET were used in the experiment. Firstly for Lg = 0.35 μm and Wg = 20.0 μm, threshold voltage was 0.185 V while the maximum I_D was 6 mA at Vds = 2.0 V. Secondly for Lg = 0.25 μm and Wg = 20.0 μm, threshold voltage that was recorded at 0.205 V and the maximum I_D = 7 mA at V_{DS} = 2.0 V. However, in comparison with simulation results, the measured values of I_D are different. This is not unexpected since there is always some process variation during the manufacture of the devices. In this particular case, the actual measured results of I_D for UMC devices are below predicted values of I_D using process average simulation parameters while the AMC devices are above the average values.

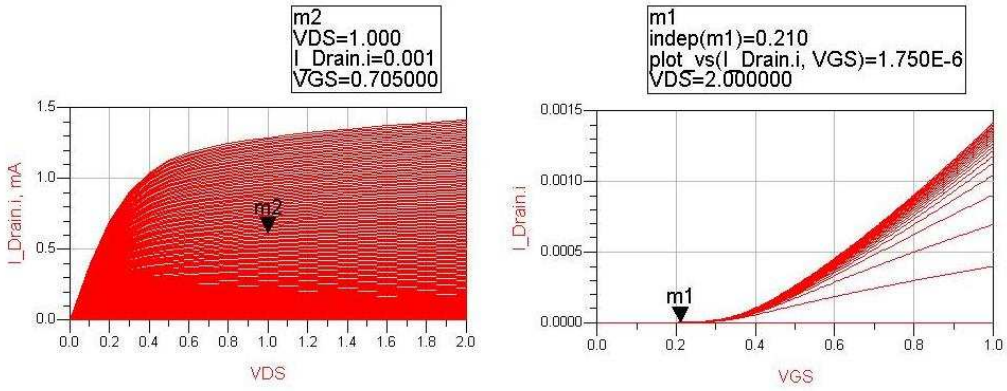

Figure 5.8: Simulated results for the I_D-V_{DS} and I_D-V_{GS} characteristics for a MOSFET AMS C35 CMOS technology, with Lg = 0.35 µm and Wg = 5.0 µm.

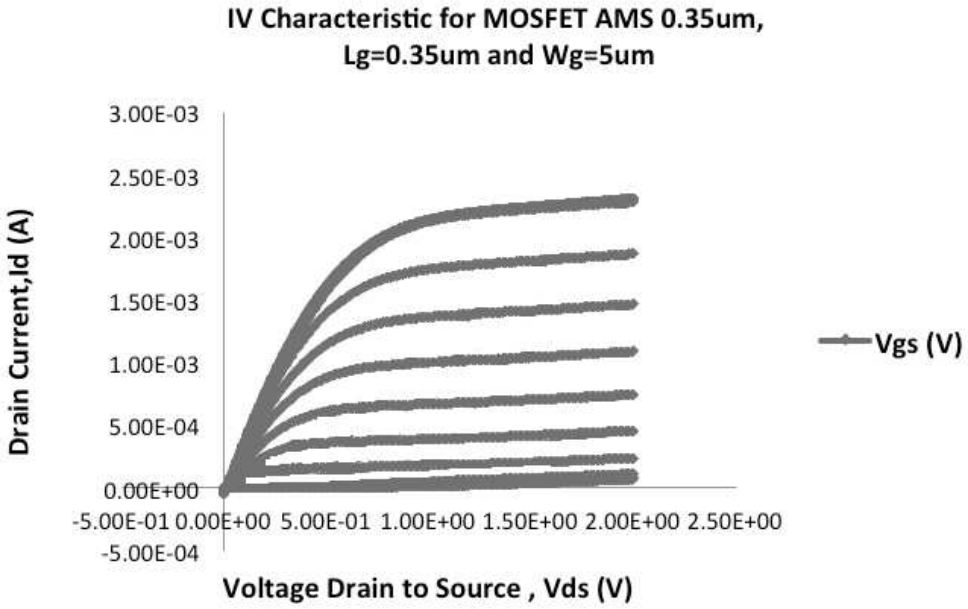

Figure 5.9: Measured IV characteristic for MOSFET Lg= 0.35 µm, Wg= 5.0 µm.

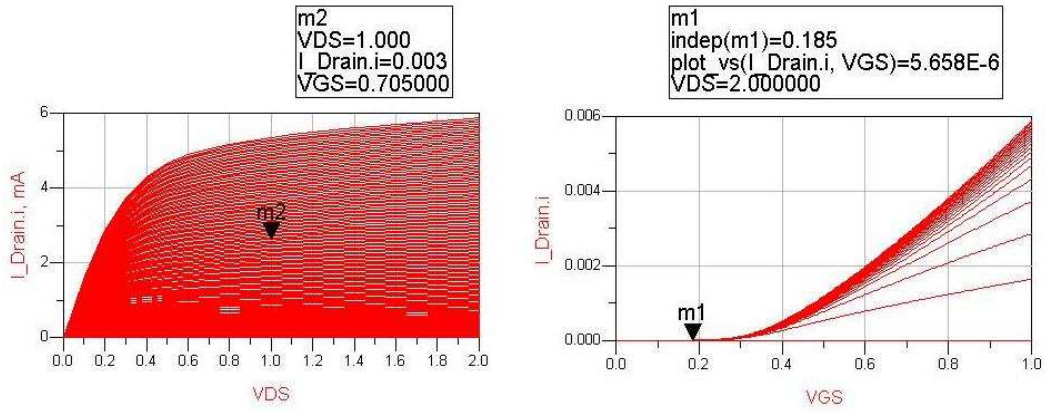

Figure 5.10: Simulated results for the I_D-V_{DS} and I_D-V_{GS} characteristics for a MOSFET UMC18 CMOS technology, with Lg = 0.35 µm and Wg = 20.0 µm.

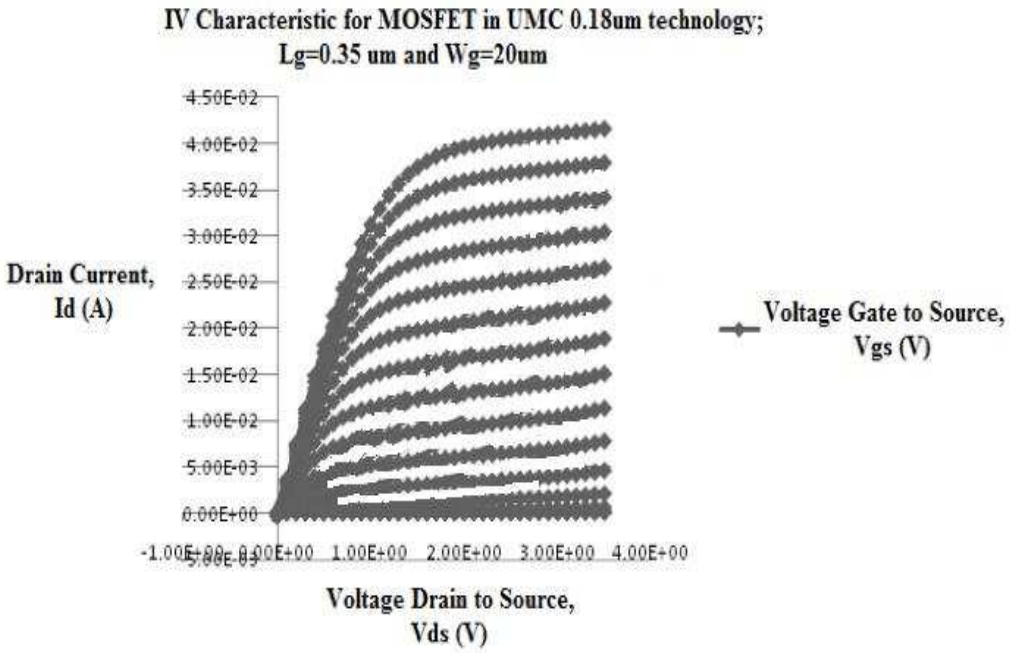

Figure 5.11: Mesured IV characteristic for MOSFET Lg= 0.35 µm and Wg= 20.0 µm.

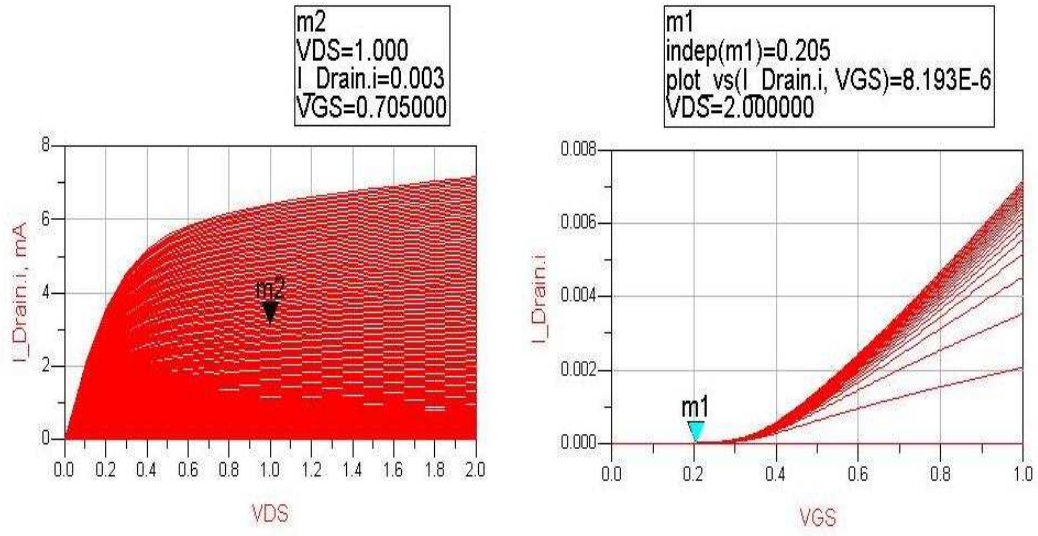

Figure 5.12: Simulated results for the I_D-V_{DS} and I_D-V_{GS} characteristics for a MOSFET UMC18 CMOS technology, with Lg = 0.25 µm and Wg = 20.0 µm.

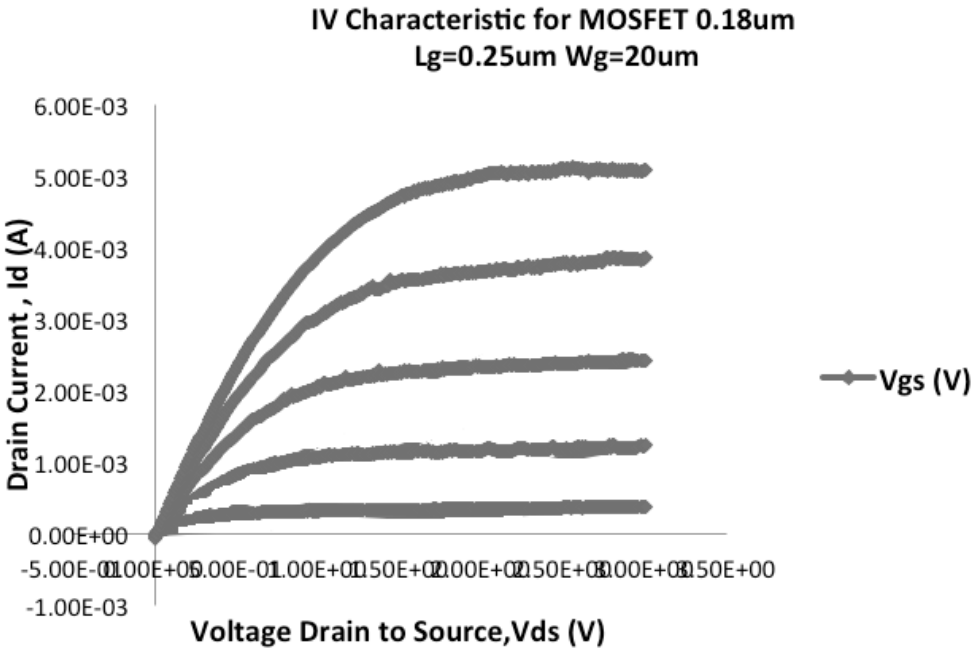

Figure 5.13: IV characteristic for MOSFET with Lg= 0.35 µm and Wg= 20.0 µm.

5.3.2 Sub-THz detection experiment

5.3.2.1 Photoresponse: varying V_{GS} and I_D

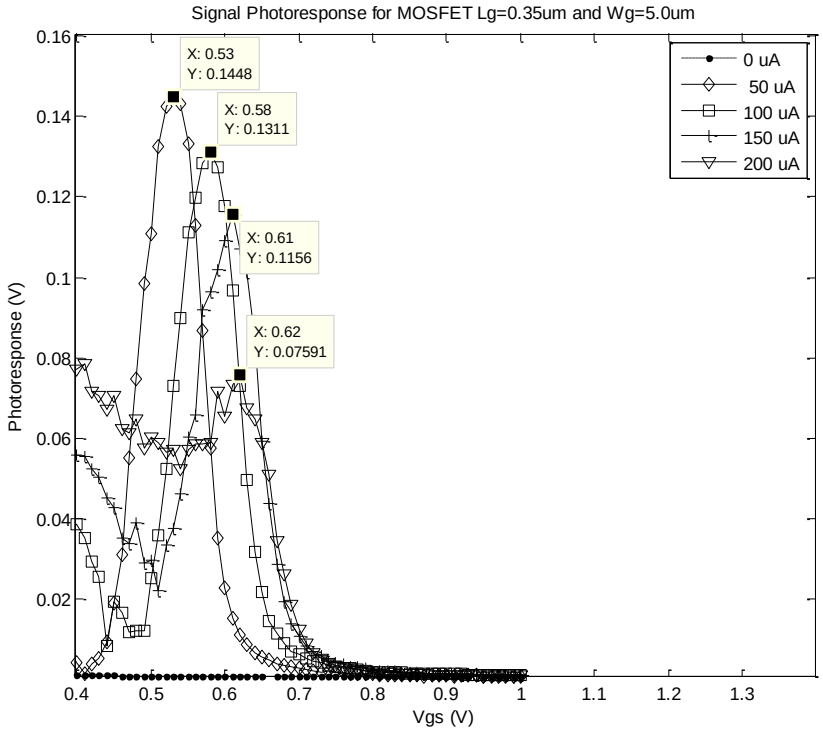

Figure 5.14: Signal photoresponse for MOSFET AMS C35 CMOS, with Lg = 0.35 μm, W= 5 μm.

Figure 5.14 shows the photoresponse of AMS C35 CMOS technology MOSFET with Lg= 0.35 μm and Wg= 5 μm. This figure shows the results of the photoresponse experiment whereby sub-THz signal was fed to the MOSFET's gate and measurement was made on V_{DS} as a function of V_{GS} for different bias currents. At this stage, the drain current was varied between 0 and 200 μA. In these measurements, the results indicate that the highest photoresponse using MOSFET technology occurred when I_D was 50 uA. In all these measurements, the frequency

was constant and set to 200 GHz with a nominal input power to the VNA extender of 13 dBm.

The method of drain current enhancement gives some information on the processes occurring plasma wave in the gate channel transistor. As the drain current increased, it will affect the plasma relaxation rate in driving two-dimensional plasma in transistor channel towards plasma wave instability [69].

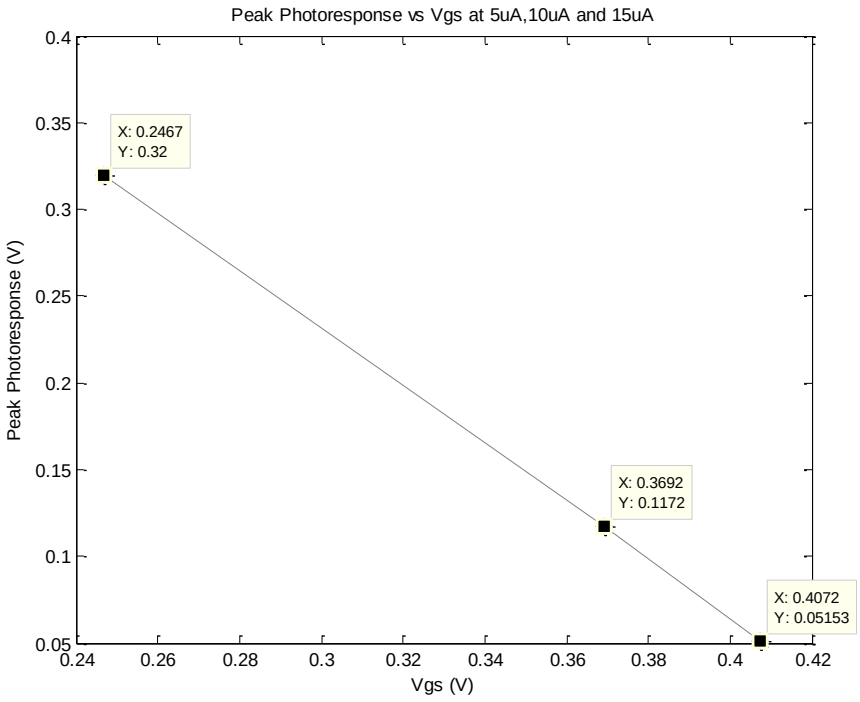

Figure 5.15: Peak photoresponse vs Vgs for MOSFET AMS C35 CMOS technology, with Lg = 0.35 μm, W=5 μm.

Since the drain current enhancement experiment looked promising at 50 μA, an experiment was performed for 5 μA, 10 μA and 15 μA and the results are shown in

Figure 5.15. From this figure, there is a clear peak of photoresponse for each drain current. The value of V_{GS} where this peak occurs decreases with I_D. In this figure, a clear "peak" at V_{GS}= 0.25 V gain for bias at 5 μA, V_{GS}= 0.37 V for bias at 10 μA and V_{GS} = 0.45 V when biasing at 15 μA. This measurement was taken using different devices but have the same size. This is because the first device used in first experiment was destroyed due to over current on the device. From the results, it is clear that the photoresponse occurs at transistors threshold voltage but depends on the drain bias current.

5.3.2.2 Photoresponse: varying V_{GS} and VNA input power.

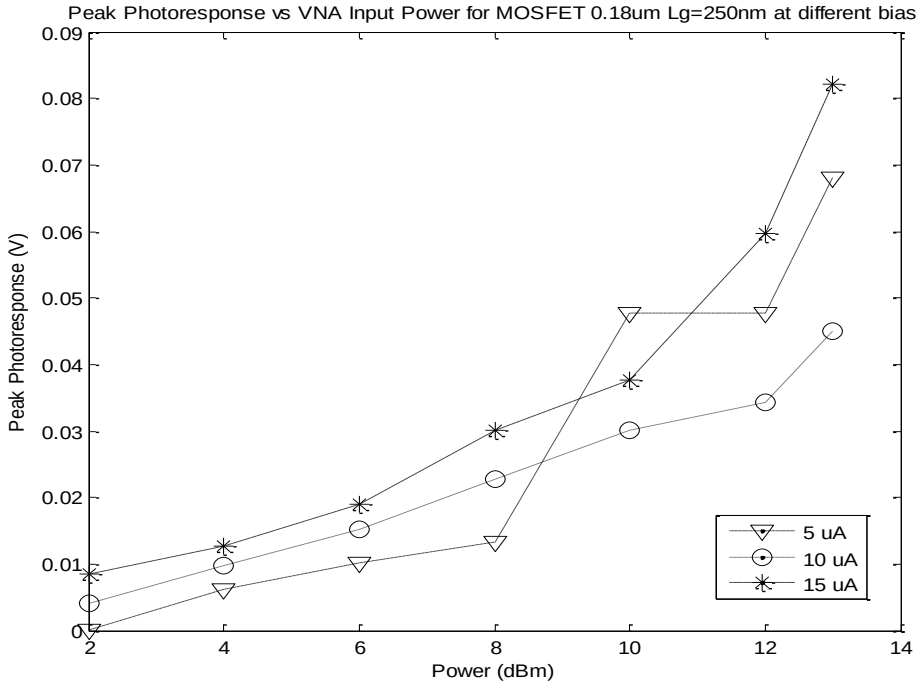

Figure 5.16: Peak photoresponse vs VNA input power for MOSFET UMC18 CMOS technology with Lg= 250 nm at different bias currents.

In this experiment the photoresponse was measured as a function of RF power input. RF input power is the input power to VNA extender. The input power was varied from 2 dBm, up to 10 dBm at 200 GHz. For the experiment using MOSFET AMS C35 CMOS devices, this was measured at one value of I_D namely 5 μA. For MOSFETs UMC18 CMOS technology devices, the photoresponse versus power was measured for different values of I_D at different input powers. Each point of diagram is the peak photoresponse versus input power that were average of 100 measurements. To obtain this measurement, V_{GS} had to be scanned so that the peak value could be found. The results are shown in Figures 5.16 and 5.17.

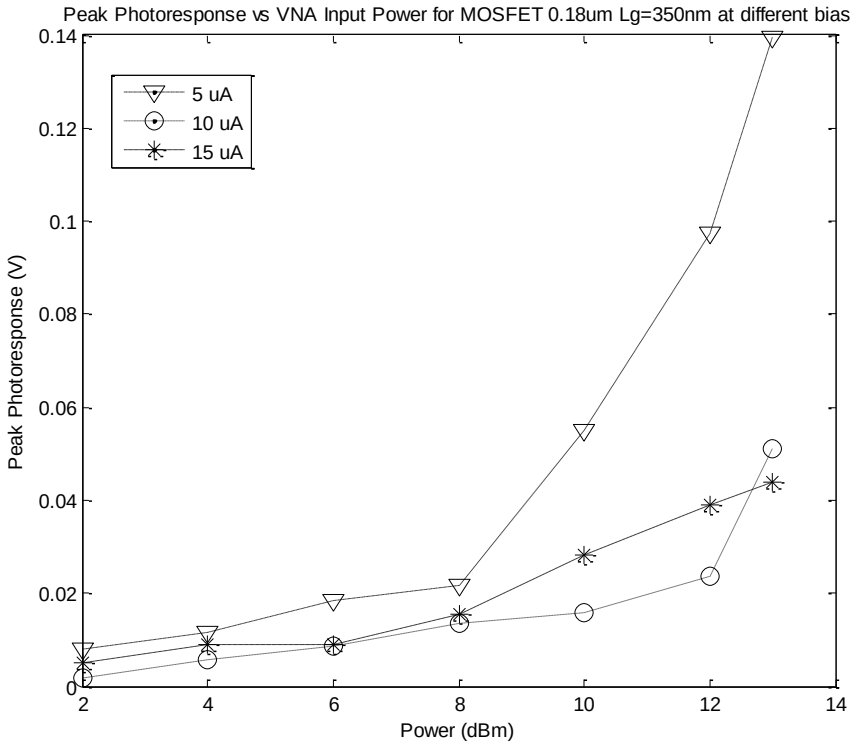

Figure 5.17: Peak photoresponse vs VNA input power for MOSFET 0.18 CMOS process, with Lg= 350 nm at different bias currents.

As shown in Figure 5.16 for Lg= 250 nm, the peak of photoresponse increases with input power to VNA extender. It is not clear what the relationship between the input and output power is. From the VNA manual, the power should be at 13 dBm, however we have no method of verifying this. In the beginning, the peak photoresponse gradually increased up to 8 dBm. The gradients of the curves for different values of I_D seem to be same. Above 8 dBm input power, the photoresponse increases rapidly. A similar result can be seen when using device with Lg= 350 nm as seen in Figure 5.17. But there are differences in the magnitude of the response and "gradient" at low power. At this stage, two conclusions can be made: first, when the current is increased, photoresponse increases and there is a shift in the peak of photoresponse. These results prove that by increasing current, the peak of the photoresponse also increases. This effect is due to increase in asymmetry of plasma waves boundary condition [87]. Secondly, when RF input power increased, the photoresponse will also increase. From the obtained results, we could see that MOSFET devices can be used as a sub-THz detector with good detection sensitivity.

5.3.2.3 Photoresponse: varying V_{GS} and frequency.

In this experiment, RF input power was set at 13dBm while I_D was fixed at 5 μA, 10 μA and 15 μA respectively. The peak of photoresponse was measured by varying V_{GS} and frequencies from 140 GHz up to 220 GHz. Again, averaging the measured signal was required. LabVieW program took 100 measurements. Internal filtering of 100 readings was also enabled within the Keithley 196 DMM. The results

of these experiments are shown in Figures 5.18 to 5.20. Note that direct comparison cannot be made because each of the measurements was made from different devices.

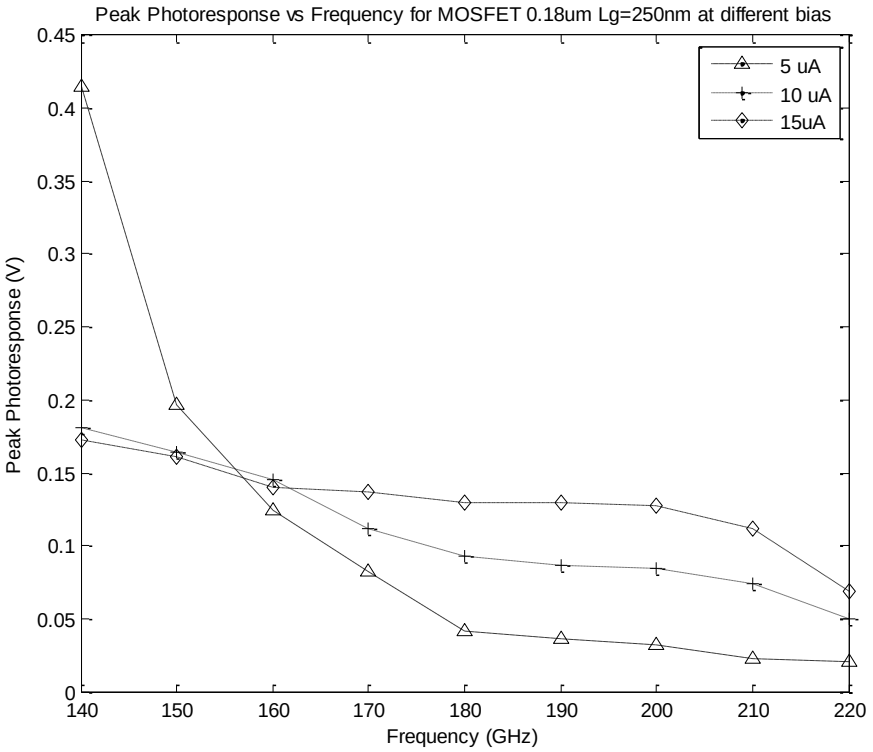

Figure 5.18: Peak photoresponse vs frequency for MOSFET UMC18 CMOS technology with Lg=250 nm at different bias currents.

From Figure 5.18, the peak of photoresponse at 140 GHz that we observed for Lg= 250 nm at I_D= 5 μm started to "resonate" from broadening photoresponse when it reaches 0.415 V. As the frequency increases, the peak of the photoresponse decreases with a gradient of -0.006 V/GHz. For a MOSFET biased I_D at 10uA, the broadening photoresponse started to decrease and the peak photoresponse was measured at 0.1808 V with decreasing gradient of -0.0025 V/GHz. After that, the bias

was increased to I_D = 15 μA, and resonant peak occurred at 0.1728 V and 140 GHz. The peak of photoresponse at this bias decreased from 140 GHz up to 220 GHz with gradient of -0.0035 V/GHz.

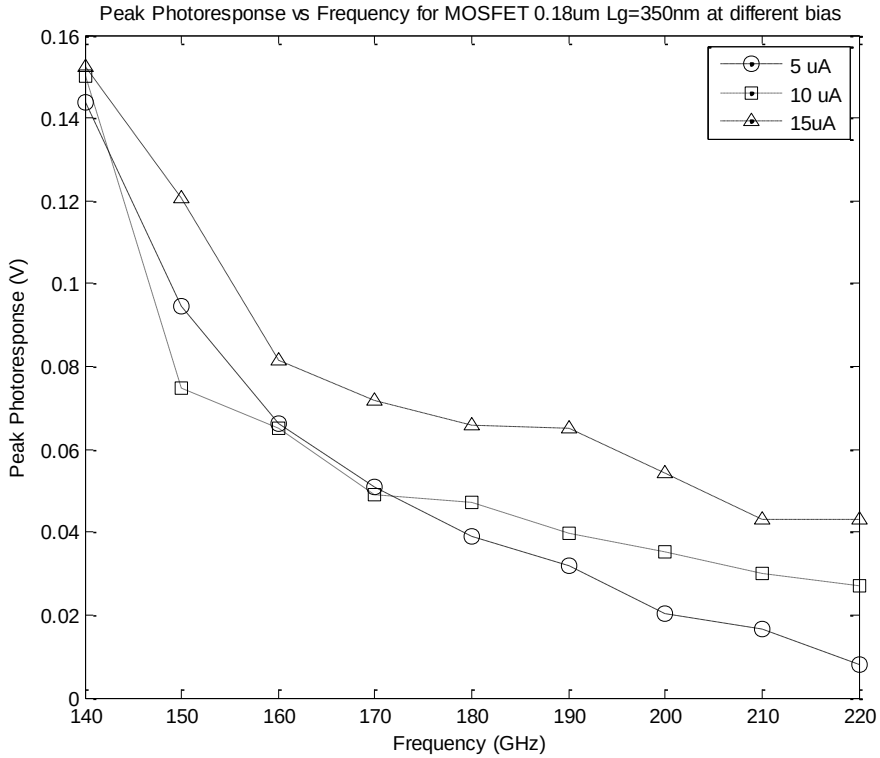

Figure 5.19: Peak photoresponse vs frequency for MOSFET UMC18 CMOS technology with Lg= 350 nm.

In Figure 5.19, with MOSFETs of Lg = 350 nm, and biased at I_D = 5 μA, the peak of photoresponse were measured at 0.1436 V at 140 GHz. The peak photoresponse was measured as a function of frequency. The results indicate that the peak of photoresponse decreases with the gradient of -0.0011 V/GHz. As the

MOSFET was biased at I_D = 10 μA, the peak of photoresponse were observed and also the peak of photoresponse starting to decrease with the gradient of -0.0008 V/GHz when sweeping the frequency from 140 GHz up to 220 GHz. Then as the MOSFET was biased at I_D = 15 μA, the peak photoresponse was measured as 0.1523 V at 140 GHz. As the frequency was swept, the results show that the peak of photoresponse was decreased with the gradient of -0.0013 V/GHz.

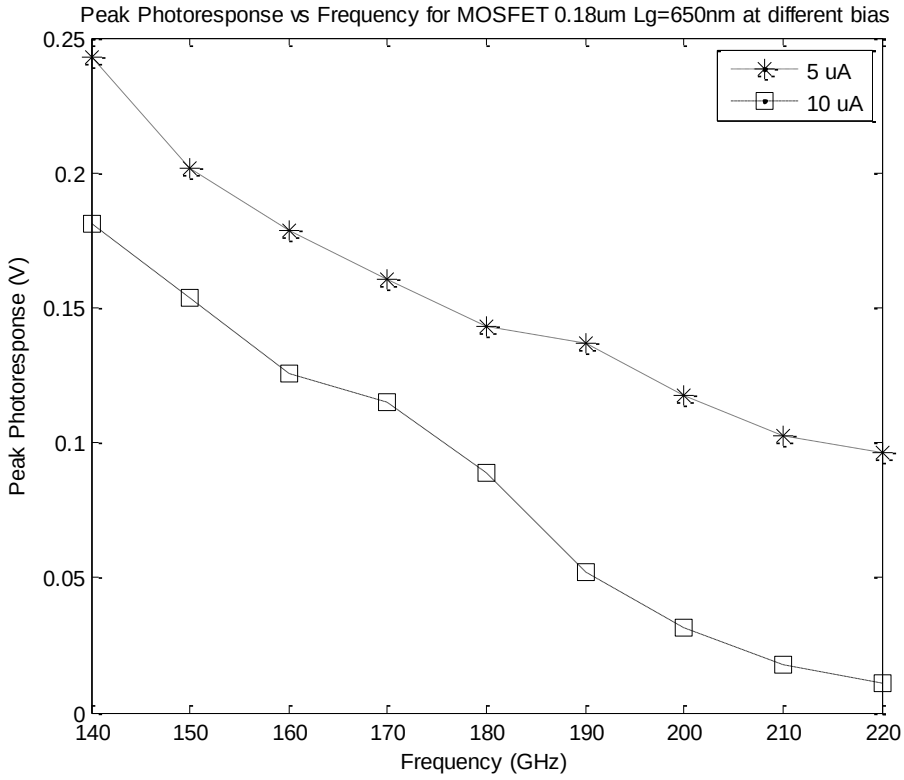

Figure 5.20: Peak photoresponse vs frequency for MOSFET UMC18 CMOS technology with Lg= 650 nm.

The peak of photoresponse of MOSFETs where Lg= 650 nm, were also observed and measured. In Figure 5.20, a biasing of I_D =5 μA, the peak of

photoresponse started to resonate at 0.2427 V at 140 GHz. Then, the peak of photoresponse decreased with frequency with a gradient of -0.00183 V/GHz. Then the MOSFET was biased at I_D = 10 μA, the peak of photoresponse were observed at 0.1813 V and the peak of photoresponse decreased with a gradient of -0.0026 V/GHz for a sweep of frequency from 140 GHz up to 220 GHz. These results prove that MOSFETs can be resonant tuneable detectors of sub-THz radiation.

Previous works on MOSFETs THz detectors show just a single broad peak in the responsivity whose maximum usually occurred at the threshold voltage of the device. In this thesis results shows that a peak in the photoresponse of the devices was observed. Several explanations are presented below to explain and support the differences.

First of all, the experiment setup in our lab is different from the methods used previously. In terms of sub-THz sources, most of previous work used a Gunn diode as the source of the sub-THz, which was chopped with a mechanical chopper. The photoresponse signal was measured using standard lock-in techniques. In our technique, the sub-THz radiation output from the Anritsu Broadband Network Analyzer ME7808B are directly coupled to the MOSFETs by using RF G-S-G Probe by Picoprobe. The detected quasi DC signal was measured using Keithley multimeter.

Secondly, the device in the experiment is from a different silicon foundry. Previous published results in MOSFETs have generally been sourced by IBM Microelectronics [96]. The IBM devices have smaller gate length, nominally 50 nm to 180 nm compared to ours. In the AMS C35 CMOS technology, the minimum gate length is 350 nm and in UMC18 CMOS technology, the minimum gate length of 250

nm, 350 nm and 650 nm were used. The RF performance would be dependent on the parasitics associated with RF pads layout and the size of the device. The properties of the 2DEG, especially the plasma waves will depend on the difference in gate length as will as the gate-source separation.

Previously, the measured photoresponse peak width was approximately 0.5 V [97]. It could be that the result presented is just one side of an unobserved peak. However, in our measurement we manage to reduce the broadening photoresponse up to the width of approximately 0.2 V. This maximum width that we achieved can't be reduced any further as the devices V_{GS} reduced below pinch off, and the resistance of the channel between the source and the drain increases rapidly.

In measuring the photoresponse at different RF input powers, the results show that by increasing the current, the photoresponse will also increase. Also as we increase the RF input power, the photoresponse also increases with a very small gradient. These results prove that responsitivity of the MOSFETs at different levels of RF input power.

In terms of the frequency dependency measurement, our experimental results are different from previously published papers [71-72]. In this thesis, the obtained results show that the MOSFETs peak photoresponse depends on varying the frequencies from 140 GHz up to 220 GHz. The results show that the peak photoresponse decreases with frequencies. In addition to these results, we managed to measure a photoresponse at 220 GHz where previous work had not been done before anywhere. To the best of the author's knowledge, this type of work has never been published before.

5.4 Conclusion

In summary, we have demonstrated the photoresponse to CW sub-THz radiation of MOSFETs from two (2) types of CMOS technology, AMS C35 UMC18 CMOS technology at different gate length caused by plasma wave detection. These results provide evidence that the photoresponse increases with the V_{GS} at different current enhancement and the RF input power, but inversely proportional to the frequencies. These experiments also provide evidence that the MOSFETs are able to work as sensitive sub-THz detectors. In general, photoresponse dependency with V_{GS} is totally different from previously reported work and several explanations have been put forward to account for these differences. As MOSFETs were proven to be a good sub-THz detector, one should look to integrate of detector with a sub-THz CMOS amplifier and this will allow the development of sub-THz front-end receiver.

Chapter 6

Conclusion and future work

6.1 Thesis conclusion

In this thesis, a review on state of the art in sub-THz generation and detection was presented, including both optical and electronic generation and detection. In chapter 3, the operation of the two terminals IMPATT diode was discussed. By employing reverse bias; avalanche multiplication process and generated holes-electron pairs will pass through the drift region. This process produces external power due to their negative resistance at microwave frequencies. Monolithic integrated IMPATT diode based on commercial AMS C35 CMOS technology was developed and tested. The diodes were simulated using ADS2006A at resonant frequencies at 30 GHz with a very large negative resistance. Based on the measurements, the avalanche frequency for IMPATT diode were observed for two different conditions; without illumination and with illumination, where without the illumination, the avalanche frequency were detected of the beginning of the frequency at 3 GHz, while by using illumination, the observation were made at 13 GHz. The objective of this research was to realise IMPATT diodes operating in the sub-THz region, but the avalanche frequency attained was at nearly 13 GHz.

Sub-THz detection by FET by plasma wave terahertz devices was investigated and the existing response models were examined. The development and the results of

photoresponse using HEMT with 0.2 μm gate length and 200 μm width caused using a sub-THz CW source from 140 GHz up to 325 GHz were presented. Experimental results showed that the photoresponse was affected by the drain current and the gate to source voltage, V_{GS}. In addition, the photoresponse also depends the changes to the frequency. Furthermore, we explored the response of the HEMT devices to varying power. Several explanations had been put forward to explain why the results are different from the previous work.

Chapter 5 presented results of using silicon MOSFET n-channel as sub-THz detectors. In this chapter the photoresponse to CW sub-THz radiation of MOSFETs for two (2) types of CMOS technology, AMS C35 and UMC18 CMOS technology with varying at different gate length was measured. Again, the method was different from previous work. In the experiment, detection reported in this thesis used RF-probing to couple the radiation into the device. Experimental results showed that the photoresponse depends on the gate-to-source voltage, drain current, frequency, and RF power. Also, by increasing the frequency, a decreasing of the maximum photoresponse was observed. Consequently, new low cost sub-THz detectors could be made of these MOSFETs by integrating them with appropriate CMOS low frequency amplifiers.

6.2 Future work

Several suggestions on the future work for sub-THz sources and detectors using semiconductor devices are presented here. For IMPATT diode, a proper design with larger active area while reducing the diode capacitance, to allow an increase of

the negative resistance and resonant frequency. In addition, the IMPATT diode also can be produced in other CMOS process such as in XFAB 0.25 μm CMOS technology, UMC 0.18 μm CMOS technology, etc. Using a proper on-wafer probe station can also increase the efficiency in the experimental assessment of the IMPATT diode.

On the experimental setup, with the availability of the Thor Labs motorized stage, an accurate THz beam placement and focus is more easily achieved. Therefore, it is possible to obtain peak photoresponse measurements at higher frequency. Additionally, response maps at these frequencies would provide insight into coupling at these frequencies, and enable the design of appropriate structures to more efficiently couple the incident radiation to the plasma wave devices.

Another suggestion is to design a Focal Plane Array (FPA) based on patch antennas integrated with MOSFETs to couple the sub-THz radiation where the feed of patch antennas are connected to the gate of MOSFETs. The on-chip antennas can mitigate substrate coupling and will increase the response. With these FPAs, a room temperature of sub-THz multiplexing imaging in CMOS can be realized.

Finally, given the impressively high speed performance of silicon-germanium devices and the ease of their integration with common silicon CMOS processing, investigation of plasma wave operation in these devices gives a great promise in terahertz multiplexing imaging.

References

[1] M. J. Fitch, R. Osiander, "Terahertz Waves for Communications and Sensing," John Hopkins APL Technical Digest, vol. 25, no. 4, pp. 348-355, 2004.

[2] N. Anscombe, "No place to hide," IEEE Review, vol. 51, no. 12, pp. 26-30, December 2005.

[3] S. Paine, R. Blundell, D. C. Papa, J. W. Barrett, S. J. E. Radford, "A Fourier Transform Spectrometer for Measurement of Atmospheric Transmission at Submillimeter Wavelengths," The Publications of the Astronomical Society of the Pacific, vol. 112, no. 767, pp. 108-118, January 2000.

[4] J. F. Federici, B. Schulkin, F. Huang, D. Gary, R. Barat, F. Oliveira, D. Zimdars, "THz Imaging and Sensing for Security Applications Explosives, weapons and drugs," Journal on Semiconductor Science and Technology, vol. 20, no. 7, pp. 266-280, 2005.

[5] V. P. Wallace, B. C. Cole, R. M. Woodward, R. J. Pye, D. A. Arnone, "Biomedical applications of terahertz technology," 15th Annual Meeting of the IEEE Lasers and Electro-Optics Society, vol. 1, pp. 308-309, 2002.

[6] M. C. Kemp, "Millimetre Wave and Terahertz Technology For The Detection of Concealed Threats -A Review," 15th IEEE International Conference on Terahertz Electronics, pp. 647-648, 2007.

[7] N. Zinov'ev, A. F. Fitzgerald, S. M. Strafford, D. J. Wood, F. A. Carmichael, R. E. Miles, M. A. Smith, J. M. Chamberlain, "Identification of Tooth Decay

using Terahertz Imaging and Spectroscopy," 27th International Conference on Infrared and Millimeter Waves, pp. 13-14, 2002.

[8] D. M. Mittleman, J. Cunningham, M. C. Nuss, M. Geva, "Noncontact semiconductor wafer characterization with the terahertz Hall effect," Applied Physics Letters, vol. 71, no. 1, pp. 16-18, 1997.

[9] M. Yamashita, T. Kiwa, M. Tonouchi, K. Nikawa, C. Otani, K. Kawase, "Laser terahertz emission microscope for inspecting electrical failures in integrated circuits," International Meeting for Future of Electron Devices, pp. 29-30, July 2004.

[10] D. H. Auston, P. R. Smith, "Generation and detection of millimeter waves by picosecond photoconductivity," Applied Physics Letters, vol. 43, no. 7, pp. 631-633, October 1983.

[11] X. C. Zhang, Y. Jin, T. D. Hewitt, X. F. Ma L.E. Kingsley, M. Weiner, "THz Beam Emission by Carrier Transport or Optical Rectification?" OSA Proceeding on Ultrafast Electronics and Optoelectronics, vol. 14, pp. 99-101, 1993.

[12] G. L. Carr, M. C. Martin, W. R. McKinney, K. Jordan, G. R. Neil, G. P. Williams, "High-power terahertz radiation from relativistic electrons," Nature, vol. 420, no. 6912, pp. 153-156, November 2002.

[13] L. F. L. Costa, J. C. S. Moraes, F. C. Cruz, R. C. Viscovini, D. Pereira, "Infrared and far-infrared spectroscopy of $^{13}CH_3OH$: Terahertz laser lines and assignments," Journal of Molecular Spectroscopy, vol. 241, no. 2, pp. 151-154, 2007.

[14] B. S. Williams, Q. Qin, S. Kumar, Q. Hu, J. L. Reno, "High-temperature and high-power terahertz quantum cascade lasers," 19th Annual Meeting of IEEE Lasers and Electro-Optics Society, pp. 128-129, October 2006.

[15] J. A. Dayton, V. O. Heinen, N. Stankiewicz, T. M. Wallett, "Submillimeter backward wave oscillators," International Journal of Infrared and Millimeter Waves, vol. 8, no. 10, pp. 1257-1268, October 1987.

[16] J. Bruston, E. Schlecht, A. Maestrini, F. Maiwald, S. C. Martin, R. P. Smith, I. Mehdi, P. Siegel, J. Pearson, "Development of 200 GHz to 2.7 THz Multiplier Chains for Submillimeter-wave Heterodyne Receivers," SPIE-International Symposium on Astronomical Telescopes and Instrumentation, 27-31 March 2000.

[17] A. Satou, V. Vyurkov, I. Khmyrova, "Plasma Oscillations in Terahertz Photomixing High-Electron-Mobility Transistor Structure on p+ -Substrate," Japanese Journal of Applied Physics, vol. 43, no. 4, pp. 566– 568, 2004.

[18] G. I. Haddad, J. R. East, H. Eisele, "Two-terminal active devices for terahertz sources," International Journal of High Speed Electronics and Systems, vol. 13, no. 2, pp. 395-427, 2003.

[19] W. Knap, J. Lusakowski, T. Parenty, S. Bollaert, A. Cappy, V. V. Popov, M. S. Shur, "Terahertz emission by plasma waves in 60 nm gate high electron mobility transistors," Applied Physics Letters, vol. 84, no. 13, pp. 2331-2333, 2004.

[20] C. M. Armstrong, "The Truth About Terahertz," IEEE Spectrum, vol. 49, no. 9, pp. 36-41, September 2012.

[21] M. Tani, M. Herrmann, K. Sakai, "Generation and detection of terahertz pulsed radiation with photoconductive antennas and application to imaging," Journal of Measurement Science and Technology, vol. 13, no. 11, pp. 1739–1745, 2002.

[22] D. Dragoman, M. Dragoman, "Terahertz fields and applications," Progress in Quantum Electronics, vol. 28, no. 1, pp. 1-66, 2004.

[23] H. F. Dylla, S. T. Corneliussen, "Free Electron Lasers Come of Age," Photonic Spectra, vol. 39, no. 8, pp. 62-68, August 2005.

[24] H. Shi, L. Jin, Y. Lu, X. Gong, Y. Zhang, H. Cui, "Optically Pumped Terahertz Laser Based on Three-Level Transition in D20," 2010 Symposium on Photonics and Optoelectronic, pp. 1-3, 2010.

[25] E. R. Brown, "THz Generation by Photomixing in Ultrafast photoconductors," International Journal of High Speed Electronic and Systems, vol.13, no. 2, pp. 497-545, 2003.

[26] B. S. Williams, S. Kumar, Q. Hu, J. L. Reno, "High-power terahertz Quantum-cascade lasers," Electronics Letters, vol. 42, no. 2, pp. 1-2, 2006.

[27] F. Hegeler, E. Schamiloglu, S. D. Korovin, V. V. Rostov, "Recent advances in the study of a long pulse relativistic backward wave oscillator," 12th IEEE International Conference on Pulsed Power, vol. 2, pp. 825-828, Jun 1999.

[28] T. Suemitsu, Y. M. Meziani, Y. Hosono, M. Hanabe, T. Otsuji, E. Sano, "Novel Plasmon-Resonant Terahertz-Wave Emitter Using a Double-Decked HEMT Structure," 65th IEEE Annual Device Research Conference, pp. 157-158, 2007.

[29] A. Reklaitis, L. Reggiani, "Monte Carlo Study of Hot-Carrier Transport in Bulk Gan and Modelling of a Near Terahertz Impact Avalanche Transit Time Diode," Journal of Applied Physics, vol. 95, no. 12, pp. 7925-7935, 2004.

[30] T. Al-Attar, T. H. Lee, "Monolithic Integrated Millimeter-Wave IMPATT Transmitter in Standard CMOS Technology," IEEE Transactions On Microwave Theory And Techniques, vol. 53, no. 11, pp. 3557-3561, November 2005.

[31] S. G. Park, M. R. Melloch, A. M. Weiner, "Analysis of Terahertz Waveforms Measured by Photoconductive and Electro Optic Sampling," IEEE Journal Of Quantum Electronics, vol. 35, no. 5, pp. 810-815, May 1999.

[32] J. R. Gao, M. Hajenius, Z. Q. Yang, J. J. A. Baselmans, P. Khosropanah, R. Barends, T. M. Klapwijk, "Terahertz Superconducting Hot Electron Bolometer Heterodyne Receivers," IEEE Transactions On Applied Superconductivity, vol. 17, no. 2, pp. 252-258, June 2007.

[33] S. Sankaran, K. O. Kenneth, "Schottky Barrier Diodes for Millimeter Wave Detection in a Foundry CMOS Process," IEEE Electron Device Letters, vol. 26, no. 7, pp. 492-494, 2005.

[34] T. Otsuji, M. Hanabe, O. Ogawara, "Terahertz Plasma Wave Resonance of Two-Dimensional Electrons in InGaP/InGaAs/GaAs High Electron Mobility Transistors," Applied Physics Letters, vol. 85, no. 11, pp. 2119-2121, 2004.

[35] W. Knap, F. Teppe, Y. Meziani, N. Dyakonova, J. Lusakowski, F. Bouef, T. Skotnicki, D. Maude, S. Rumyantsev and M. S. Shur, "Plasma Wave

Detection of Sub-Terahertz and Terahertz Radiation by Silicon Field Effect Transistors," Applied Physics Letters, vol. 85, no 4, pp. 675-677, 2004.

[36] P. L. Richards, "Bolometers for Infrared And Millimeter Waves," Journal of Applied Physics, vol. 76, no. 1, pp. 1-24, 1994.

[37] S. Ariyoshi, C. Otani, A. Dobroiu, H. Sato, K. Kawase, H. M. Shimizu, T. Taino, H. Matsuo, "Terahertz Imaging with a Direct Detector based on Superconducting Tunnel Junctions," Applied Physics Letters, vol. 88, no. 20, pp. 203503-203506, 2006.

[38] D. Dooley, "Measuring THz Radiation…choose a Pyroelectric Detector or Golay Cell?" Spectrum Detector Incoporated, Application Note 1011, Rev. A, pp.1-5, 2009.

[39] Y. Jang, Y. Kim, D. Seo, D. Yee, "Terahertz Frequency and Power Measurement Based on Terahertz Frequency Comb and a Bolometer," 34th International Conference on Infrared, Millimeter and Terahertz Waves, pp. 1-2, 2009.

[40] C. Otani, K. Hoshino, T. Taino, H. Myoren, R. Nakano, S. Ariyoshi, H. Sato, H. M. Shimizu, S. Takada, K. Kawase, "Terahertz Detector using a Nb-Based Superconducting Tunnel Junction," 12th International Conference on Terahertz Electronics, pp. 243-244, 2004.

[41] G. Gerlach, D. Shvedov, V. Norkus, "Packaging Influence on Acceleration Sensitivity of Pyroelectric Infrared Detectors," 6th IEEE CPMT Conference on High Density Microsystem Design and Packaging and Component Failure Analysis, pp. 297 - 302, 2004.

[42] R. Han, Y. Zhang, D. Coquillat, H. Videlier, W. Knap, E. Brown, K. O. Kenneth, "A 280-GHz Schottky Diode Detector in 130-nm Digital CMOS," IEEE Journal Of Solid-State Circuits, vol. 46, no. 11, pp. 2602-2612, November 2011.

[43] J. Q. Lu, M. S. Shur, "Terahertz Detection by High Electron Mobility Transistor: Effect of Drain Current," 12th International Symposium on Space Terahertz Technology, pp. 103-111, 2001.

[44] R. L. Jonston, B. C. DeLoach, B. G. Cohen, "A Silicon Diode Oscillator," Bell Systems Technical Journal, vol. 44, pp. 369-374, 1965.

[45] W. T. Read, "A Proposed High-Frequency, Negative-Resistance Diode," Bell Systems Technical Journal, vol. 37, pp. 401-446, 1958.

[46] M. Gilden, M. E. Hines, "Electronic Tuning Effects in the Read Microwave Avalanche Diode," IEEE Transactions on Electron Devices, vol. 13, no. 1, pp 169-175, 1966.

[47] P. J. Stabile, B. Lalevic, "Lateral IMPATT diodes," IEEE Electron Device Letters, vol. 10, no. 6, pp. 249-251, 1989.

[48] C. Dalle, P. A. Rolland, G. Lleti, "Flat Doping Profile Double-Drift Silicon IMPATT for Reliable CW High-Power High-Efficiency Generation in the 94-GHz Window," IEEE Transactions on Electron Devices, vol. 37, no. 1, pp. 227-236, 1990.

[49] A. Steller, E. M. Biebl, J. F. Luy, K. M. Strohm, J. Buechler, "A Monolithic Integrated Millimeter Wave Transmitter for Automotive Applications," IEEE

Transactions on Microwave Theory and Technology, vol. 43, no. 7, pp. 1654-1658, 1995.

[50] C. J. Schoellhorn, M. Morschbach, H. Xu, W. Zhao, E. Kasper, "S-Parameter Measurements of the Impedance of mm-Wave IMPATT Diodes in dependency on the Current Density," Journal of Microwaves and Optoelectronics, vol. 3, no. 5, pp. 81-96, July 2004.

[51] T. Al-Attar, M. D. Mulligan, T.H. Lee, "Lateral IMPATT Diodes in Standard CMOS Technology," IEEE International Electron Devices Meeting, pp. 459-462, 2004.

[52] C. J. Schoellhorn, M. Morschbach, M. Oehme, J. Hasch, H. Irion, E. Kasper, "Monolithically Integrated Silicon-IMPATT Oscillator at 93 GHz," 33rd European Microwave Conference, pp. 1291-1294, 2003.

[53] F. Träger, "Springer Handbook of Lasers and Optics", 2nd Edition, Springer, pp. 574-578, 2012.

[54] G. P. Srivastava, V. L. Gupta, "Microwave Devices and Circuit Design", PHI Learning Private Limited, pp. 294-302, 2006.

[55] E. M. Conwell, "High Field Transport in Semiconductor," Solid State Physics, Academic Press New York, vol. G, October 1967.

[56] M. C. A. M. Koolen, J. A. M. Geelen, M. P. J. G. Versleijen, "An Improved De- Embedding Technique for On-wafer High-frequency Characterization," IEEE Bipolar Circuits and Technology Meeting, vol. 1, pp. 188-191, 1991.

[57] G. W. Johnson, R. Jennings, "LabVIEW Graphical Programming 4th edition," The Mc Graw-Hill Companies, 2006.

[58] C. P. Wen, "Coplanar Waveguide: A Surface Strip Transmission Line suitable for Nonreciprocal Gyromagnetic Device Applications", IEEE Transactions on Microwave Theory and Techniques, vol. 17, no. 12, pp.1087- 1090, December 1969.

[59] R. S. Singh, P. Tewari, J. L. Bourges, J. P. Hubschman, D. B. Bennett, Z. D. Taylor, H. Lee, E. R. Brown, W. S. Grundfest, M. O. Culjat, "Terahertz sensing of corneal hydration," IEEE International Conference on Engineering in Medicine and Biology Society, pp. 3021-3024, 2010.

[60] H. Quast, T. Loffler, "Towards real-time active THz range imaging for security applications," International Conference on Electromagnetics in Advanced Applications, pp. 501- 504, 2009.

[61] C. Kulesa, "Terahertz Spectroscopy for Astronomy: From Cosmets to Cosmology," IEEE Transactions on Terahertz Science and Technology, vol. 1, no. 1, pp. 232-240, 2011.

[62] K. Ajito, Y. Ueno, "THz Chemical Imaging for Biological Applications," IEEE Transactions on Terahertz Science and Technology, vol. 1, no. 1, pp. 293-300, 2011.

[63] F. Yan, "Application on non-destructive inspection of Terahertz wave," 10th World Congress on Intelligent Control and Automation, pp. 1570-1573, 2012.

[64] A. Rogalski, F. Sizov, "Terahertz detectors and focal plane arrays," Opto-Electronics Review, vol. 19, no. 3, pp. 346-404, 2011.

[65] S. Cherednichenko, A. Hammar, S. Bevilacqua, V. Drakinskiy, J. Stake, A. Kalabukhov, "A Room Temperature Bolometer for Terahertz Coherent and Incoherent detection," IEEE Transactions on Terahertz Science and Technology, vol. 1, no. 2, pp. 395-402, 2011.

[66] R. Yao, S. H. Ding, Q. Li, Q. Wang, "Real-time THz reflection imaging using a pyroelectric array camera," 10th Russian-Chinese Symposium on Laser Physics and Laser Technologies and 2010 Academic Symposium on Optoelectronics Technology, pp. 125-127, 2010.

[67] J. L. Hesler, T. W. Crow, "NEP and responsivity of THz zero-bias Schottky diode detectors," Joint 32nd International Conference on Infrared and Millimeter Waves and 15th International Conference on Terahertz Electronics, pp. 844-845, 2007.

[68] H. Yi, N. Khiabani, S. Yaochun, L. Di, "Terahertz photoconductive antenna efficiency," International Workshop on Antenna Technology, pp. 152-156, 2011.

[69] M. S. Shur, J. Q. Lu, M. I. Dyakonov, "Plasma wave electronics: terahertz sources and detectors using two-dimensional electronic fluid in high electron mobility transistors," 6th IEEE International Conference on Terahertz Electronics, pp. 127-130, 1998.

[70] Y. Kawano, K. Ishibashi, "A wide-band wavelength-tunable terahertz detector using a graphene transistor," 35th International Conference on Infrared Millimeter and Terahertz Waves, pp. 1-4, 2010.

[71] W. Knap, V. Kachorovskii, Y. Deng, S. Rumyantsev, J. Q. Lu, R. Gaska, M. S. Shur, G. Simin, X. Hu, M. Asif Khan, C. A. Saylor, L.C. Brunel, "Nonresonant detection of terahertz radiation in field effect transistors," Journal of Applied Physics, vol. 91, no. 11, pp. 9346-9353, 2002.

[72] F. Teppe, D. Veksler, V. Yu. Kachorovski, A.P. Dmitriev, X. Xie, X.C.Chang, S. Rumyantsev, W. Knap, M. Shur, "Plasma Wave Resonant Detection of Femtosecond Pulsed Terahertz Radiation by Nanometer Field Effect Transistor," Applied Physics Letters, vol. 87, no. 2, pp. 022102 - 022105, 2005.

[73] X. G. Peralta, S. J. Allen, M. C. Wanke, N. E. Harff, J. A. Simmons, M. P. Lilly, J. L. Reno, P. J. Burke and J. P. Eisenstein, "Terahertz Photoconductivity and Plasmon modes in Double-Quantum-Well Field Effect Transistors," Applied Physics Letters, vol. 81, no.9, pp. 1627-1629, 2002.

[74] W. Stillman, F. Guarin, V. Yu. Kachorovskii, N. Pala, S. Rumyantsev, M. S. Shur and D. Veksler, "Nanometer Scale Complementary Silicon MOSFETs as Detectors of Terahertz and Sub-Terahertz Radiation," IEEE Sensors, pp. 934-936, 2007.

[75] M. Dyakonov and M. S. Shur, "Shallow Water Analogy for a Ballistic Field Effect Transistor: New Mechanism of Plasma Wave Generation by DC Current," Physics Review Letters, vol. 71, no. 15, pp. 2465-2468, 1993.

[76] F. Teppe, A. El Fatimy, S. Boubanga, D. Seliuta, G. Valusis, B. Chenaud and W. Knap, "Terahertz Resonant Detection by Plasma Waves in Nanometric Transistors," Acta Physica Polonica A, vol. 113, no. 3, pp. 815-820, 2007.

[77] V. Ryzhii and M. S. Shur, "Plasma wave electronics devices,"2003 International Semiconductor Device Research Symposium, pp.200-201, 2003.

[78] M. S. Shur and V. Ryzhii, "New Concepts for Submillimeter-Wave Detection and Generation," 11th GAAS Symposium, pp. 301-304, 2003.

[79] P.J. Burke, I.B. Spielman, J.P. Eisenstein, L. N. Pfeiffer, and K. W. West "High frequency conductivity of the high-mobility two-dimensional electron gas," Applied Physics Letters, vol. no. 6, pp. 745-747, 2000.

[80] W. Knap, W. Deng, Y. Rumyantsev, S. Lu, J.-Q. Shur, M. S. Saylor, C. A. Brunel, L. C., "Resonant Detection of Subterahertz Radiation by Plasma Waves in a Submicron Field Effect Transistor," Applied Physics Letters, vol. 80, no. 18, pp. 3433-3435, 2002.

[81] ATF-36163 1.5–18 GHz Surface Mount Pseudomorphic HEMT, Data Sheet, pp. 1-10, Avago Technologies, 2008.

[82] R. J. Gilmore, M. B. Steer, "Nonlinear circuit analysis using the method of harmonic balance—A review of the art. Part I. Introductory concepts," International Journal of Microwave and Milliter Wave Cmputer –Aided Engineering, vol. 1, no. 1, pp. 22-37, 1991.

[83] M. H. Olsen, "PCB design tutorial with Eagle," Orsted-DTU, Automation, Technical University of Denmark, pp. 1-15, March 2004.

[84] Bonnie C. Baker, "Circuit Layout Techniques And Tips," Microchip Technology Incorporated, Application Notes I-IV, pp. 1-43, 2004.

[85] B. Kennedy, M. Cantrell, "EMI Reduction and PCB Layout Techniques," TLSI Incorporated, Application Notes, AN-101, pp. 1-3, November 2003.

[86] PCB Train; http://www.pcbtrain.co.uk/

[87] S. B. Tombet, F. Teppe, D. Coquillat, S. Nadar, N. Dyakonova, H. Videlier, W. Knap, A. Shchepetov, C. Gardès, Y. Roelens, S. Bollaert, D. Seliuta, R.Vadoklis, G. Valušis, "Current Driven Resonant Plasma Wave Detection of Terahertz Radiation: Toward the Dyakonov–Shur Instability," Applied Physics Letters, vol. 92, no. 21, pp. 212101-212104, 2008.

[88] M. A. Othman, I. Harrison, "Continuous Wave (CW) sub- Terahertz (sub-THz) detection by Plasma Wave in High Electron Mobility Transistor (HEMT)," IEEE Asia Pacific Conference on Circuits and Systems, pp. 987-990, 2010.

[89] M. Sakowicz, J. Lusakowski, K. Karpierz, M.Grynberg, W. Knap, W.Gwarek, "Polarisation Sensitive Detection of 100 GHz Radiation by High Mobility Field Effect Transistors," Journal of Applied Physics, vol. 104, no. 2, pp. 024519 - 024524, 2008.

[90] D. Veksler, F. Teppe, A. P. Dmitriev, V. Yu. Kachorovskii, W. Knap, M. S. Shur, "Detection of Terahertz radiation in Gated Two-Dimensional Structures governed by DC Current," Physical Review B, vol. 73, no. 12, pp. 125328-125338, 2006.

[91] N. Pala, F. Teppe, D. Veksler, Y. Deng, M. S. Shur, R. Gaska, "Nonresonant Detection of Terahertz radiation by Silicon-On-Insulator MOSFETs," IET Electronics Letters, vol. 41, no. 7, pp. 447 - 449, 2005.

[92] A. J. Martin, “Tutorial: Cadence Design Environment”, Klipsch School of Electrical and Computer Engineering, New Mexico State University, pp. 1-51, October 2002.

[93] High Performance Microwave Probes Model 220 http://www.ggb.com/220.html

[94] AMS 0.35 µm CMOS process technology http://www.austriamicrosystems.com/

[95] UMC 0.18 µm process technology http://www.umc.com/english/process/d.asp

[96] W. Stillman, D. Veksler, T. A. Elkhatib, K. Salama, F. Guarin, M. S. Shur, “Sub-terahertz testing of silicon MOSFET,” Electronics Letters, vol. 44, no. 22, pp. 1325-1327, 2008.

[97] Y. M. Meziani, J. Lusakowski, N. Dyakonova, W. Knap, D. Seliuta, E. Sirmulis, J. Devenson, G. Valusis, F. Boeuf, T. Skotnicki, “Non Resonant Response to Terahertz Radiation by Submicron CMOS Transistors”, IEICE Transactions on Electronics, vol. E89-C, no. 7, pp. 993-998, 2006.

Appendix

Chapter 3:

De-embedding procedure.

De-embedding technique need to be done since the inner diode cannot be measured directly. The open and short structures are designed and the gap between metal in the open structure is the same dimension of the IMPATT diode. Figure below shows the short , open, and load elements used for de-embedding IMPATT diode:-

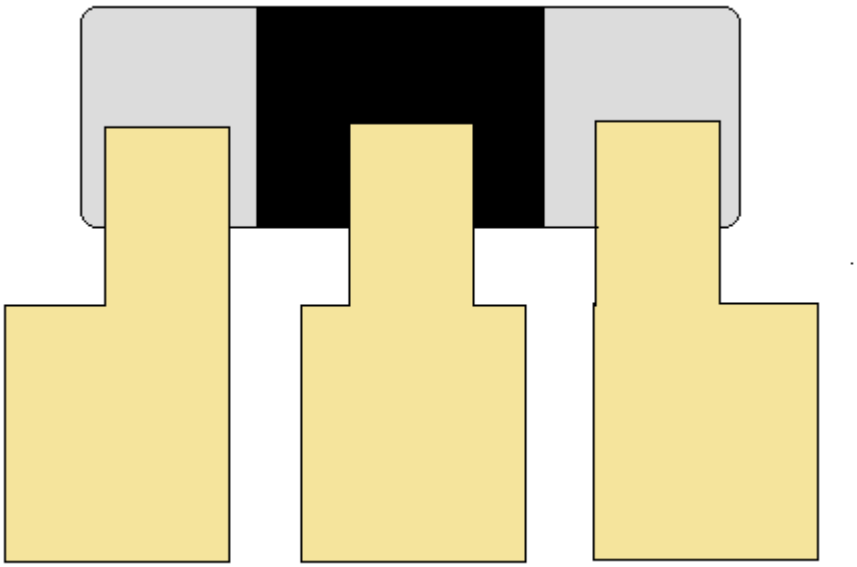

Figure A3.1: Load

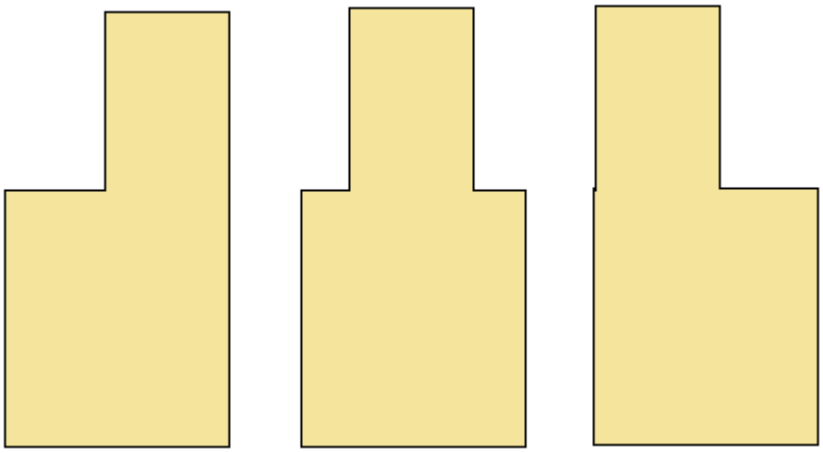

Figure A3.2: Open

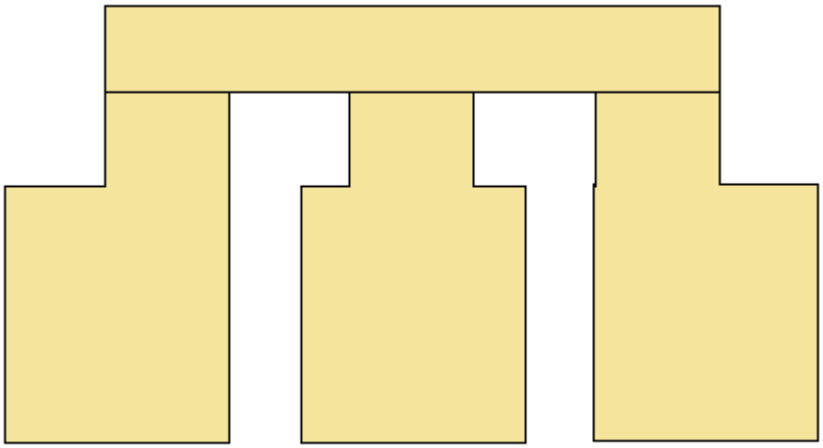

Figure A3.3: Short

With these structures the impedance of the parallel and the parasitic caused by RF pad and the metal between RF pad and the diode can be estimated and subtracted from the quantified impedance of the diode. The impedance of measured diode with metal and RF pads is called Z_{DUT} (DUT is device under test) where the inner diode we

called it Z_{DIODE}. The equivalent circuit IMPATT diode with de-embedding technique is shown in figure below:-

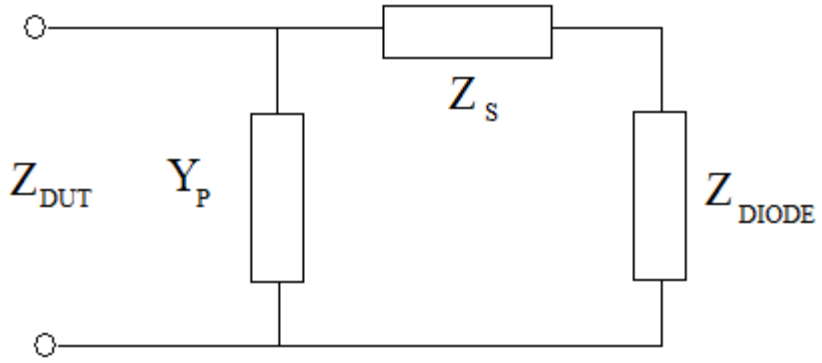

Figure A3.4: Equivalent circuit of the IMPATT diode embedded for S-Parameter

At first stage, the reflection coefficient of the Z_{DUT} is measured. Then the reflection coefficient transformed to impedance by using formula below with characteristic impedance $Z_O = 50\ \Omega$,

$$Z = \frac{1+\Gamma}{1-\Gamma}.\mathrm{Zo} \qquad (3.13)$$

The open structure, is firstly used to determine the parallel admittance Y_P of the contact structure:

$Y_{OPEN} = Y_P$. Then the admittance of short circuit Y_{SHORT} is measured where $Y_{SHORT} = 1/Z_S$. With all the impedance can be known, the inner diode impedance can be calculated by following equation :-

$$Z_{DIODE}=(Y_{DUT}-Y_{OPEN})^{-1} - (Y_{SHORT}-Y_{OPEN})^{-1} \qquad (3.14)$$

Y_{DUT} is measured of Y-Parameter device including all the structure, and Y_{SHORT} and Y_{OPEN} is the Y parameter for open and short. The procedure of deembedded technique had been published by Koolen et al. in 1990 [3.10]. Figure 3.17 below shows measured S11 for short and open deembed.

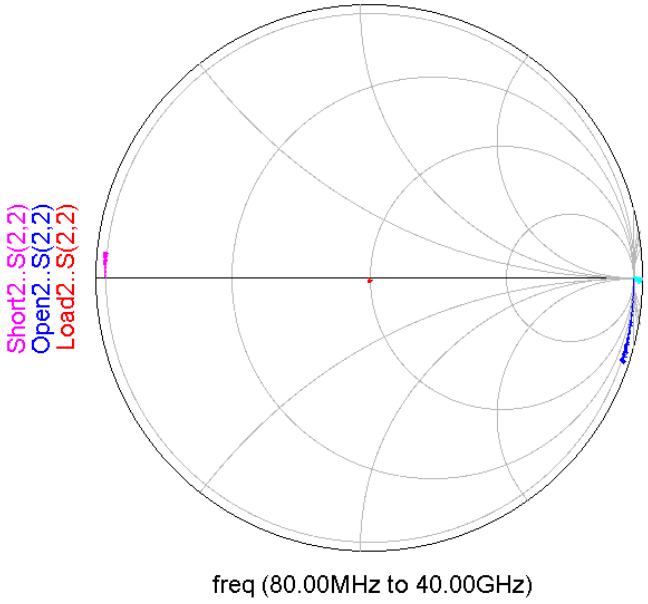

Figure A3.5: Calibration results on the Smith Chart

Chapter 4

FET IV Characteristic and THz Detector using NI Labview 8.5

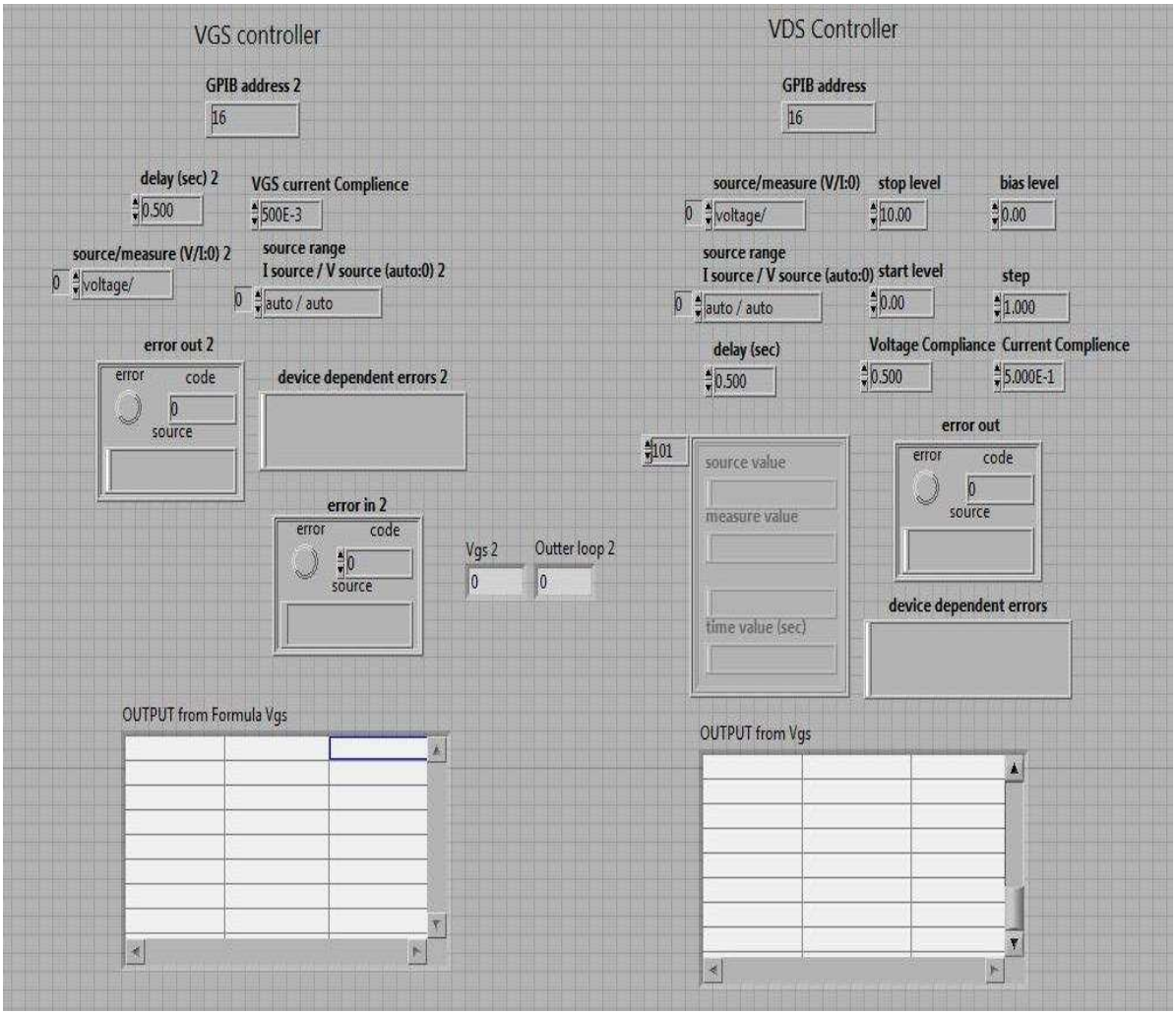

Figure A4.1: IV Characteristic ATF36163.vi Front panel

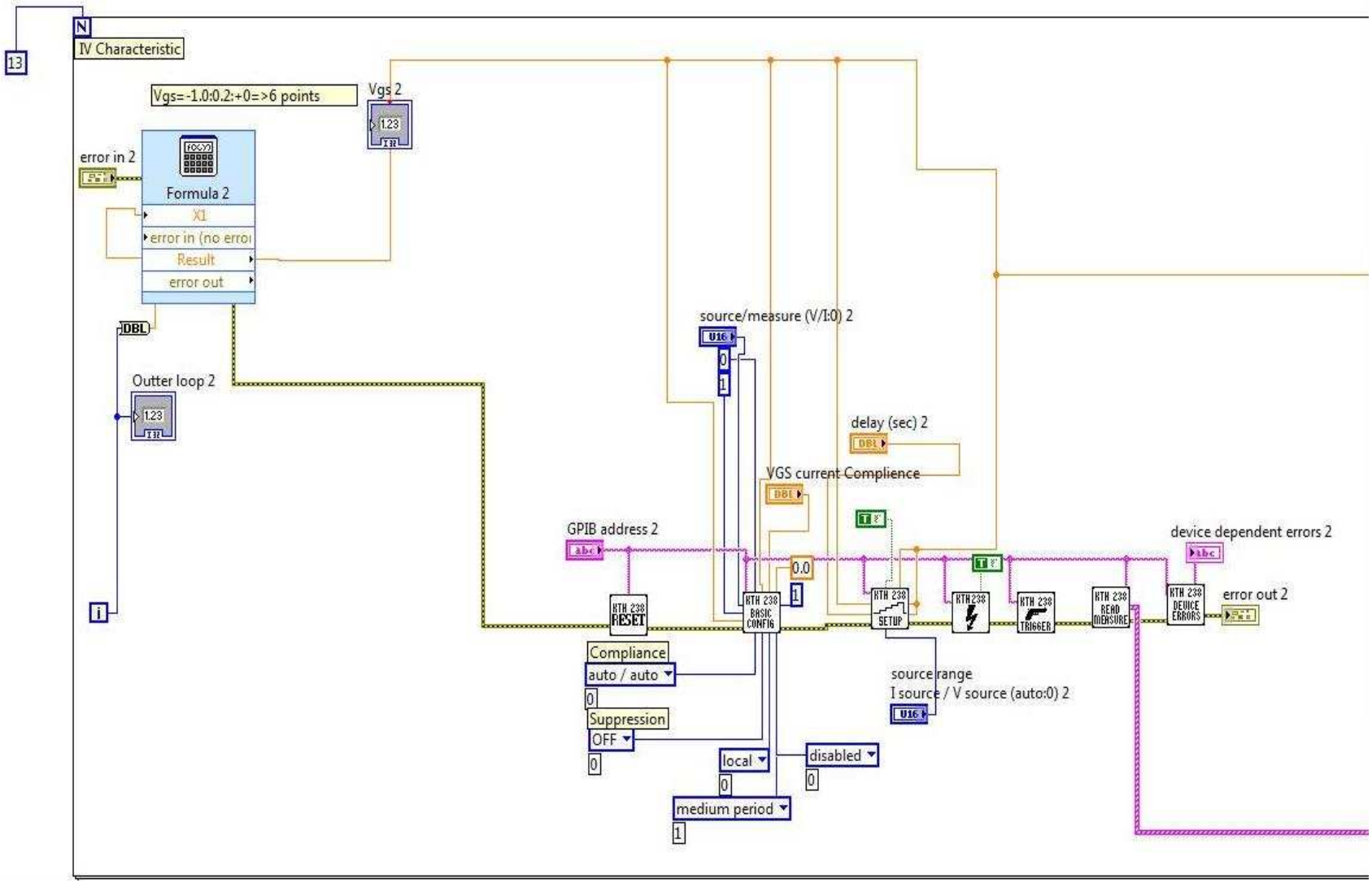

Figure A4.2: IV Characteristic ATF36163.vi block diagram 1

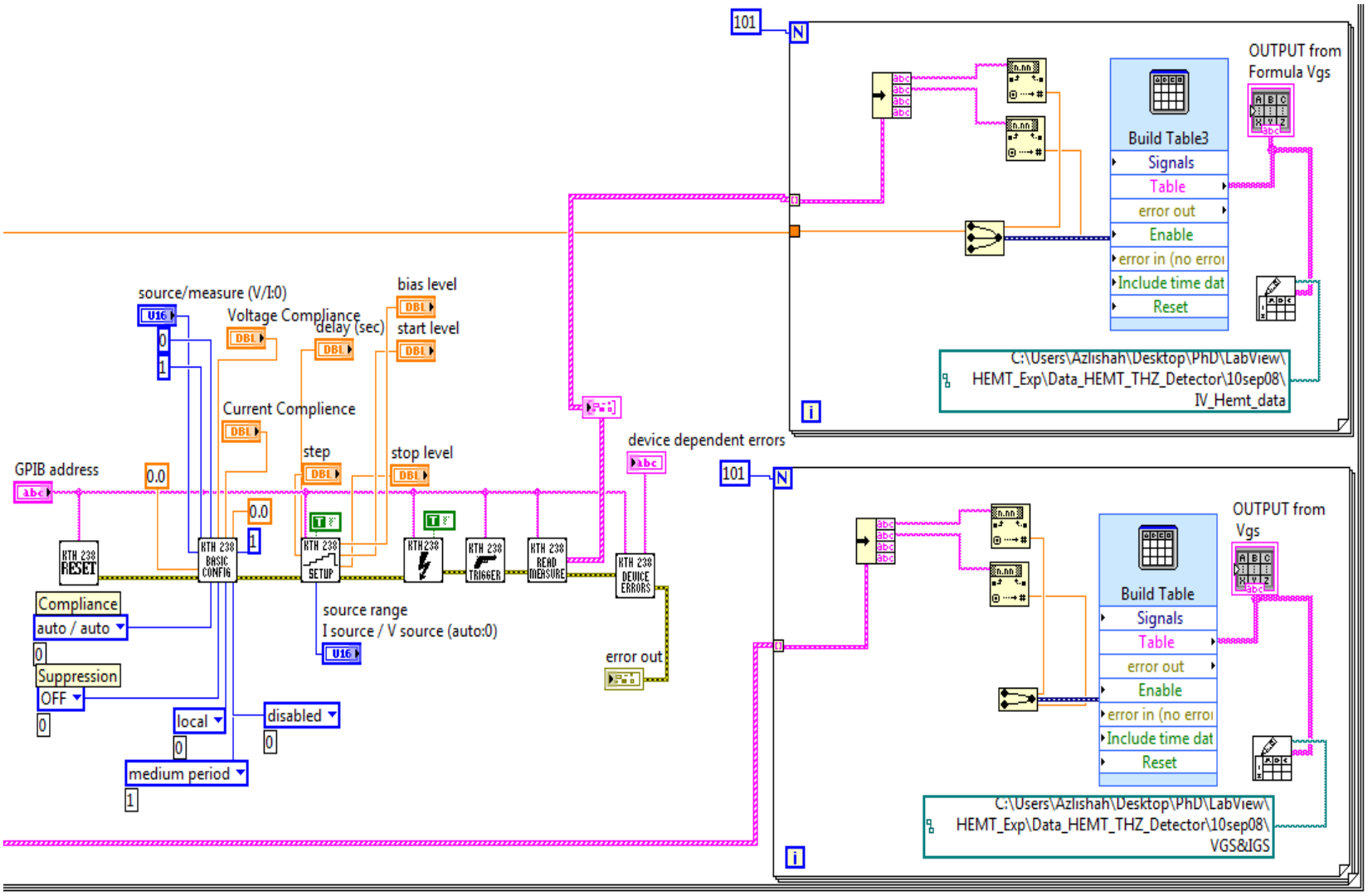

Figure A4.3: IV Characteristic ATF36163.vi block diagram 2

Photoresponse Experiment using NI Labview 8.5

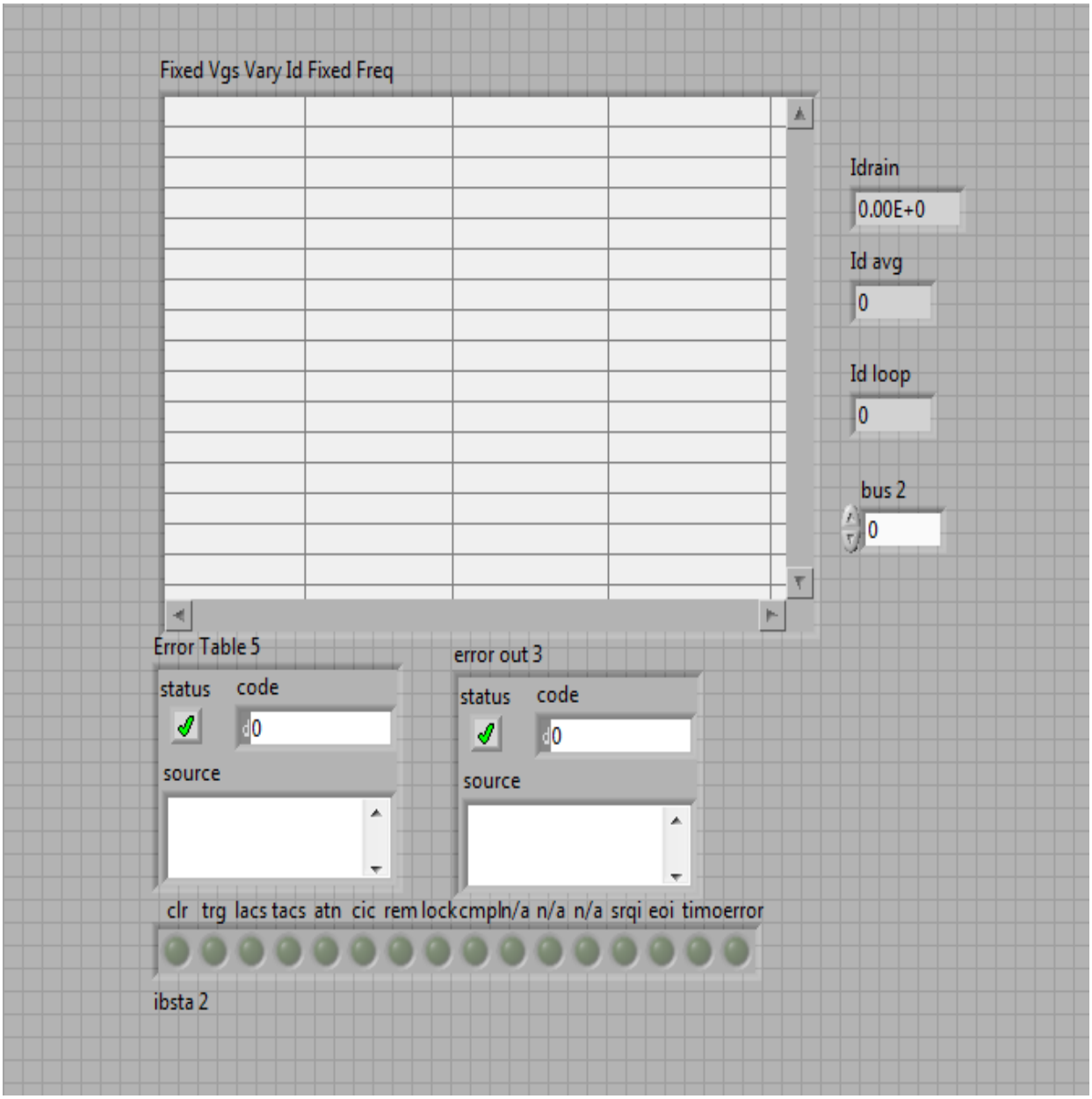

Figure A4.4: Photoresponse front panel using ATF36163.vi

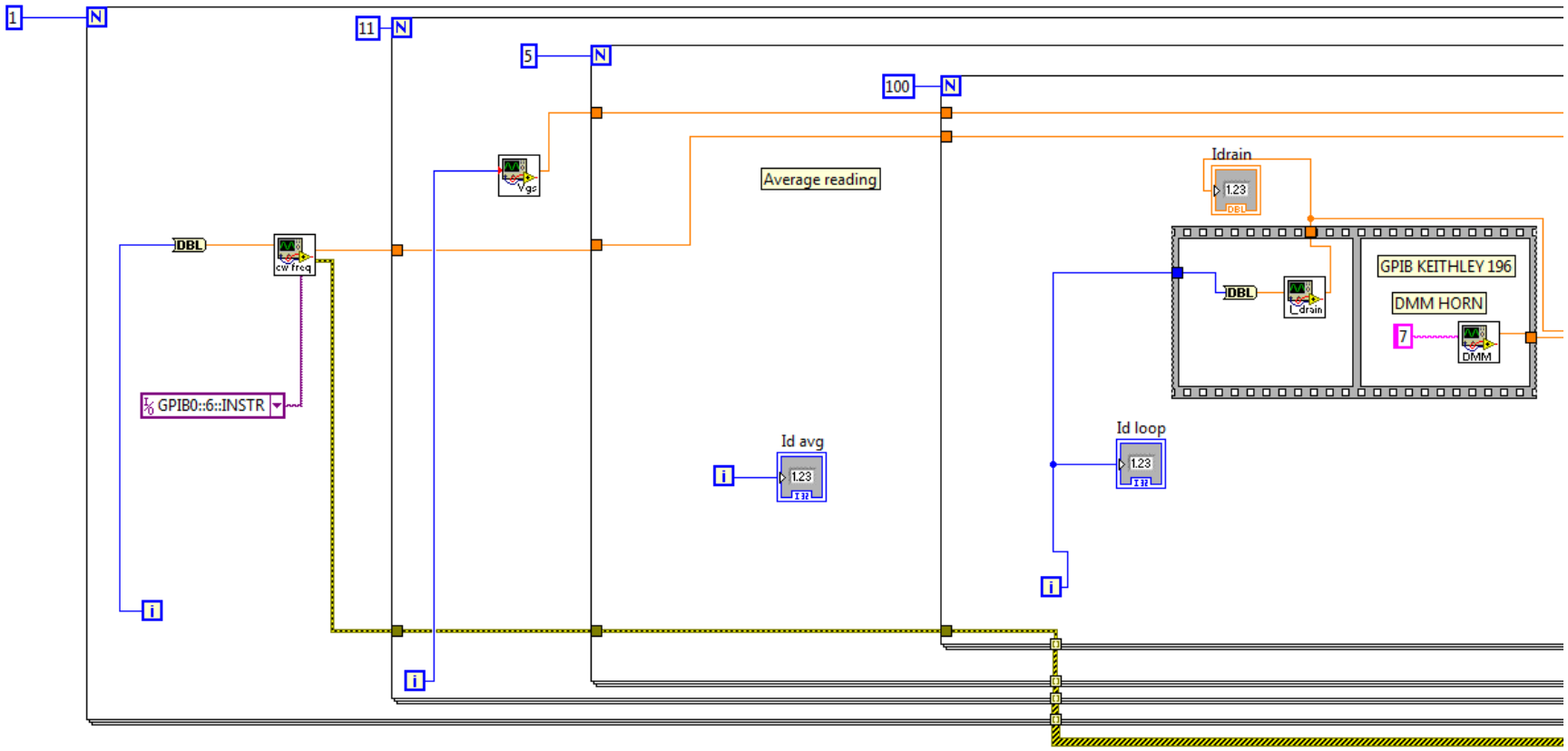

Figure A4.5: Photoresponse block diagram 1.vi

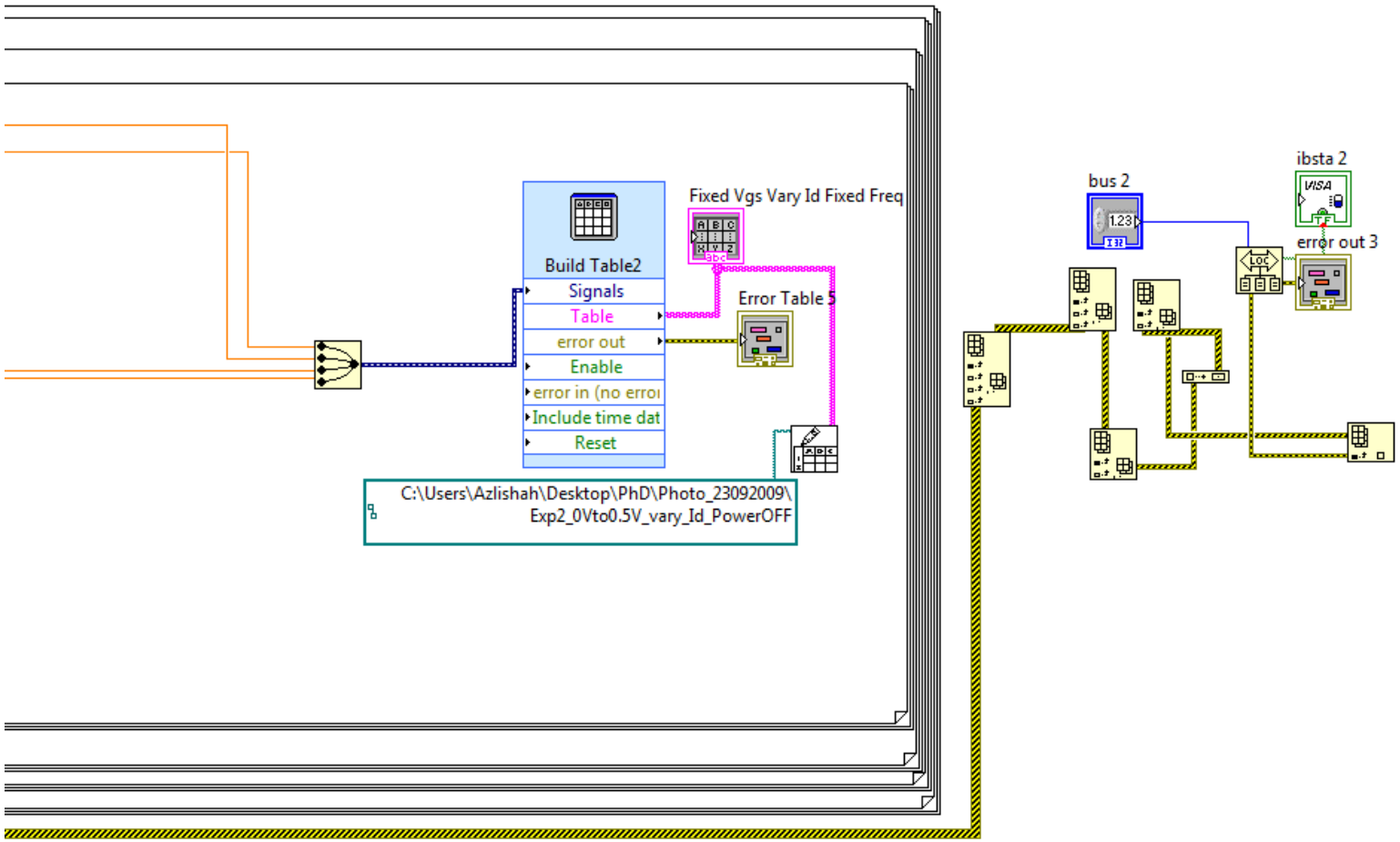

Figure A4.6: Photoresponse block diagram 2 .vi

Chapter 5

FET IV Characteristic and THz Detector using NI Labview 8.5

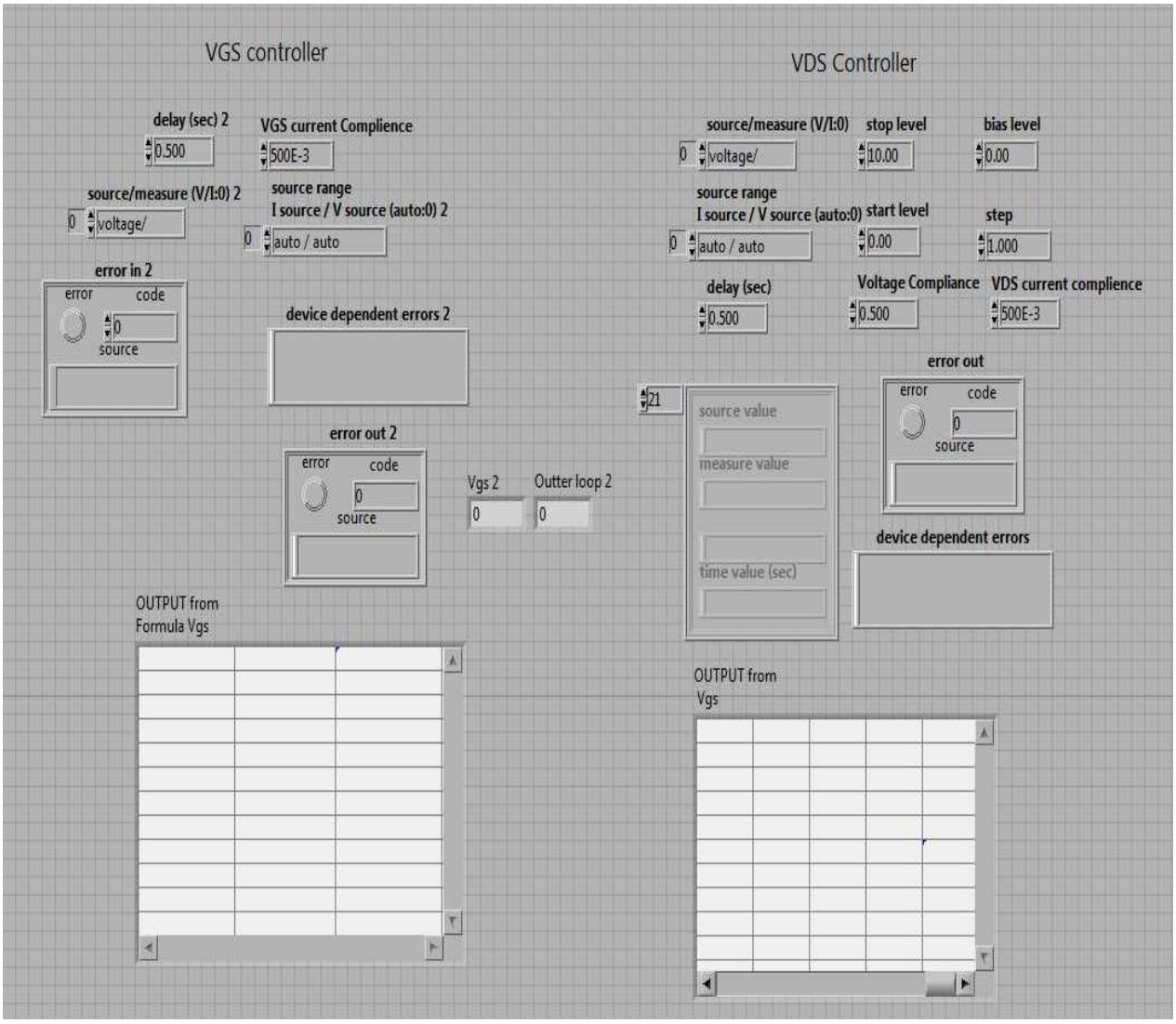

Figure A5.1: IV Characteristic MOSFET.vi Front panel

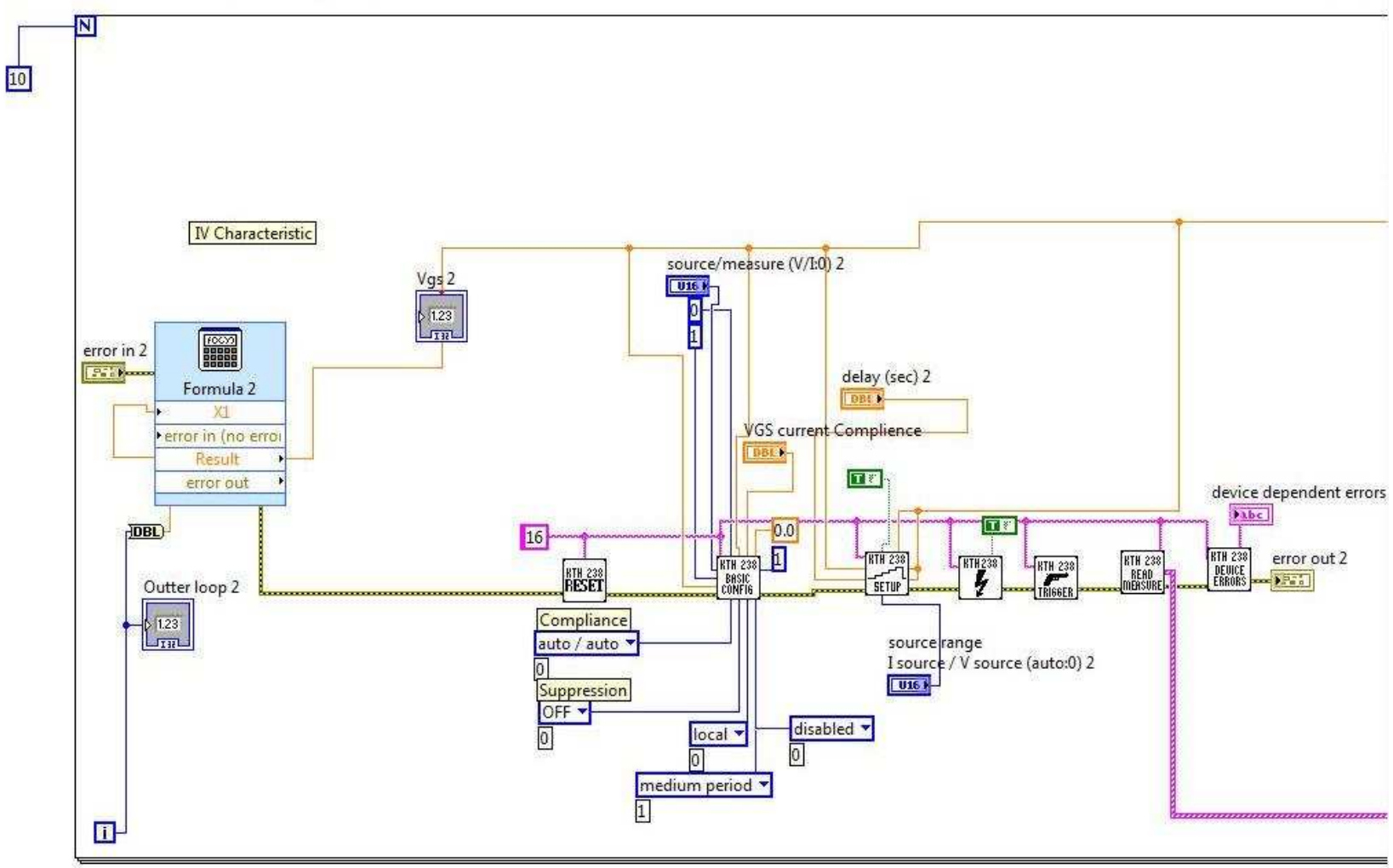

Figure A5.2: IV Characteristic MOSFET.vi block diagram 1

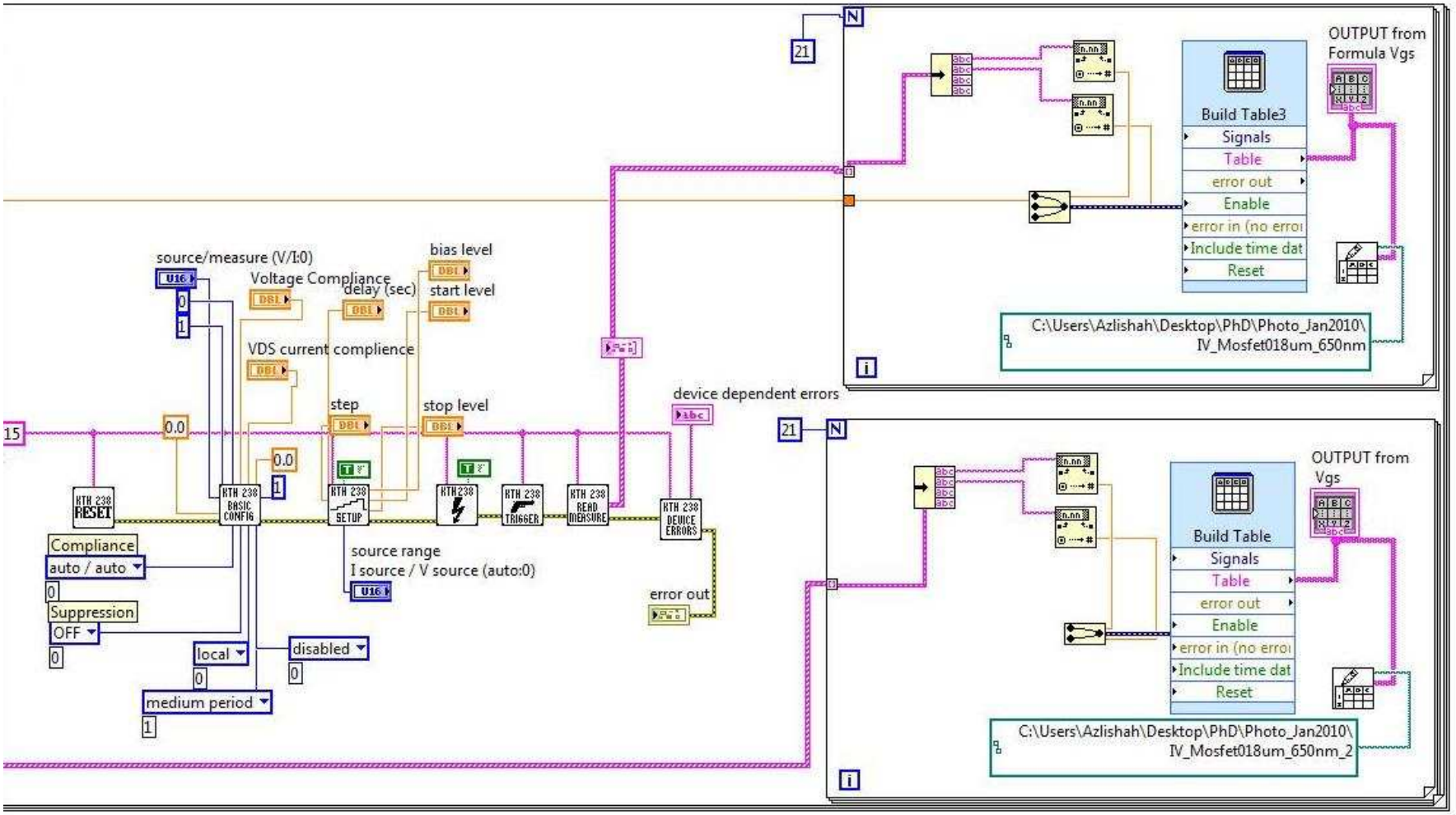

Figure A5.3: IV Characteristic ATF36163.vi block diagram 2

Photoresponse Experiment using NI Labview 8.5

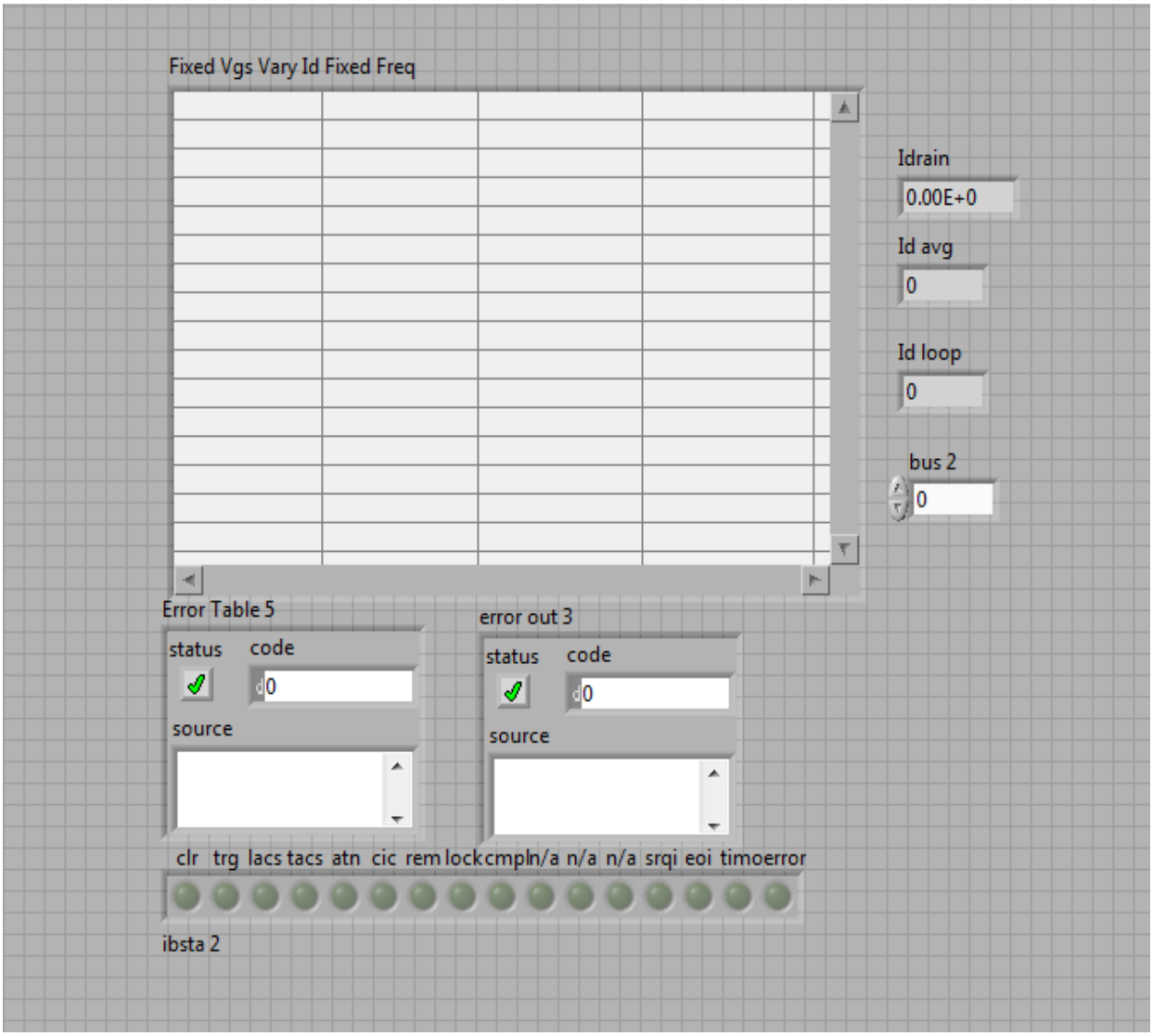

Figure A5.4: Photoresponse front panel using MOSFET.vi

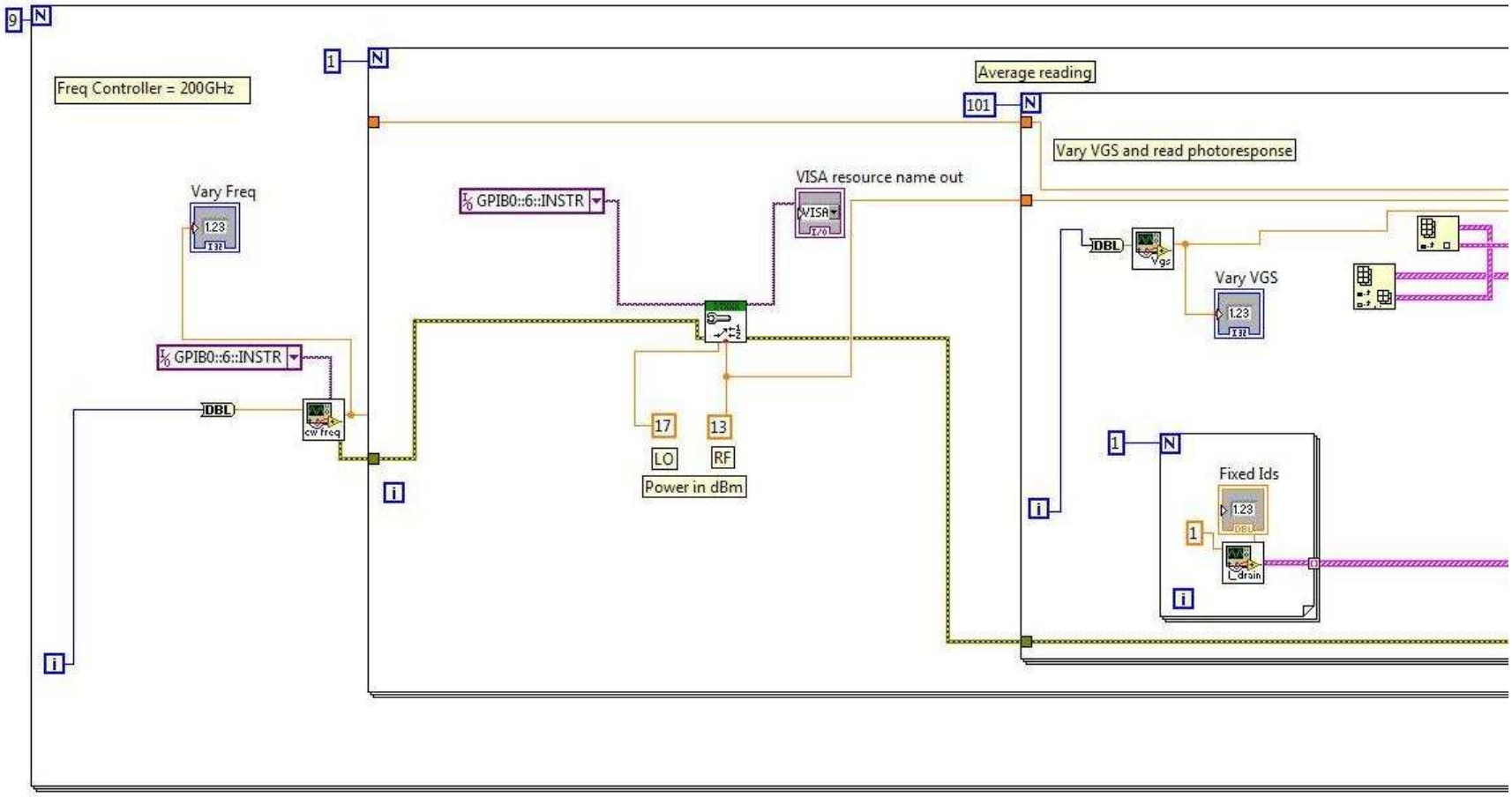

Figure A5.5: Photoresponse MOSFET.vi block diagram 1.vi

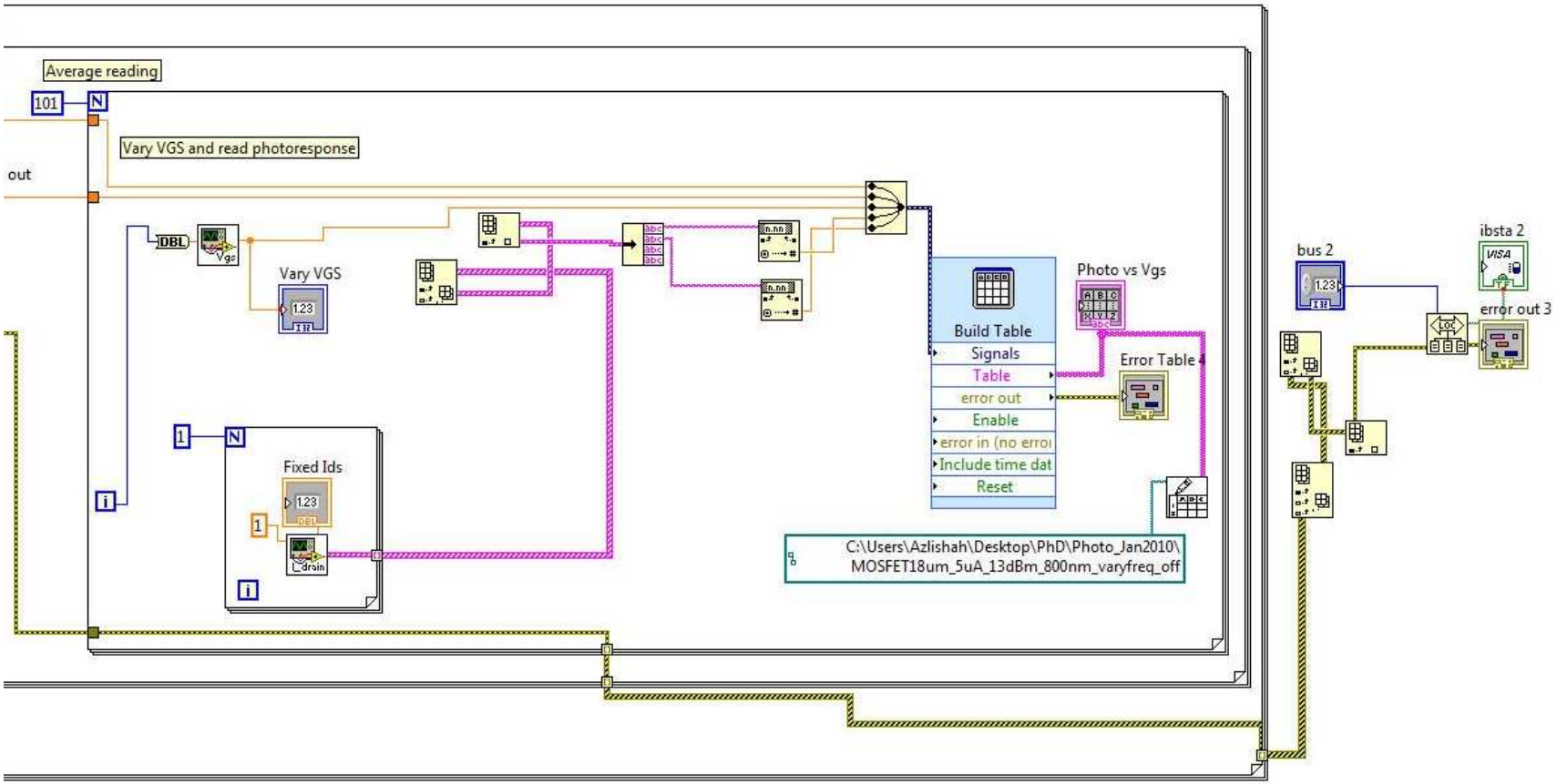

Figure A5.6: Photoresponse MOSFET.vi block diagram 2 .vi